A Raman spectral characterization of thin-film carbon: the impact of source wavelength variation

by

Md. Ashraf Ul Ahsan

B.Sc. in Electrical and Electronic Engineering, American International University-Bangladesh, 2015

A THESIS SUBMITTED IN PARTIAL FULFILLMENT OF
THE REQUIREMENTS FOR THE DEGREE OF

MASTER OF APPLIED SCIENCE

in

The College of Graduate Studies

(Electrical Engineering)

THE UNIVERSITY OF BRITISH COLUMBIA

(Okanagan)

May 2019

The following individuals certify that they have read, and recommend to the College of Graduate Studies for acceptance, a thesis/dissertation entitled:

A Raman spectral characterization of thin-film carbon: the impact of source wavelength variation

submitted by Md. Ashraf Ul Ahsan in partial fulfilment of the requirements of the degree of Master of Applied Science

Dr. Stephen K. O'Leary, School of Engineering
Supervisor

Dr. Jian Liu, School of Engineering
Supervisory Committee Member

Dr. Jahangir Hossain, School of Engineering
Supervisory Committee Member

Dr. Nicolás Peleato, School of Engineering
University Examiner

Abstract

Raman spectroscopy is ubiquitous in the study of thin-film carbon. Often, the Raman spectrum of a thin-film carbon is characterized in terms of the location of two distinct peaks, a D-peak located around 1360 cm^{-1} and a G-peak located about 1580 cm^{-1}. Many of the material properties of thin-film carbon have been related either to the ratio of the D-peak and G-peak amplitudes or to the ratio of the D-peak and G-peak integrated intensities. In this analysis, I aim to assess whether or not a relationship exists between these two distinct ratios. Through an examination of the Raman spectra associated with a number of representative carbon thin-films, it has been established that the amplitude ratio is indeed related to the corresponding integrated intensity ratio. The samples of thin-film carbon that are probed using Raman spectroscopy have been prepared through the use of plasma-enhanced chemical vapor deposition and rf and dc magnetron sputtering. The slope of this relationship is shown to be related to the source wavelength, larger source wavelengths corresponding to a smaller slope. The scatter about the resultant linear fit is also found to increase as the source wavelength is increased. Recommendation for further study are offered.

Lay Summary

The vibrational character of thin-film carbon is interrogated through the use of Raman spectroscopy. In this approach, a laser source beam interacts with the molecular vibrations that are present within the material, such interactions leading to changes in the wavelength of the light that is re-emitted from this material. It is these changes in wavelengths that are detected in Raman spectroscopy. In this analysis, we relate the form of the Raman spectrum to its material properties. The implications of these results are then explored.

Preface

This thesis is based on the research work conducted in the School of Engineering at The University of British Columbia's Okanagan campus under the supervision of Dr. Stephen K. O'Leary. This thesis is an original and unpublished work by the author, Md. Ashraf Ul Ahsan.

The author has performed the Raman experiments on the samples prepared by Mr. Jonathan Laumer during his postgraduate academic studies. The Raman spectra for this particular analysis have been acquired as per his guidance.

Table of Contents

List of Tables

List of Figures

List of Acronyms

I_D	Integrated intensity of D-peak
I_G	Integrated intensity of G-peak
A_D	Amplitude of D-peak
A_G	Amplitude of G-peak
DLC	Diamond-like carbon
CVD	Chemical vapor deposition
PECVD	Plasma-enhanced chemical vapor deposition
PVD	Physical vapor deposition
UV	Ultra-violet
IR	Infra-red
dc	Direct current
rf	Radio-frequency
Ar	Argon
CCD	Charge-coupled device
ta-C:H:N	Hydrogenated tetrahedral amorphous carbon nitride
EELS	Electron energy loss spectroscopy
°C	Celsius
Si	Silicon
nc-Si:H	Hydrogenated nanocrystalline silicon
sccm	Standard cubic centimeter per minute
TMS	Tetramethylsilane
HeCd	Helium cadmium
HeNe	Helium neon
OD	Optical density
eV	Electronvolt
R-squared	Coefficient of correlation-squared
A.U.	Arbitrary unit
NMR	Nuclear magnetic resonance

Acknowledgements

Firstly, I would like to express my gratitude to my supervisor, Dr. Stephen K. O'Leary, for selecting me as his graduate student, for guiding me through my research work and for his constructive feedback throughout the thesis writing process.

Sharing of information is critical to scientific progress and for this reason I am indebted to Mr. Jonathan Laumer in Dr. Stephen K. O'Leary's research group for the innumerable conversations and sharing of ideas related to this research while also working on his own doctoral studies.

I am grateful to Dr. Guangrui Xia for giving me access to Horiba Raman machine and for connecting me with Mr. Yunlong Zhao from her research group who has helped me acquire the Raman measurements. Ms. Yujie Yin (Grace) and Mr. Tao Fang from Dr. Guangrui Xia's research group have also invested their valuable time during my visit to their lab in the Vancouver campus of the University of British Columbia, in order to conduct my research. I am thankful to Dr. Andrew Jirasek for creating an opportunity for me to get trained by his graduate student, Mr. Ramie Ali Adeeb, on how to operate the Renishaw Raman machine in order to understand the spectral information better. I would also like to acknowledge the Graduate Studies Administration Assistant, Ms. Shannon Hohl, of the School of Engineering at the University of British Columbia-Okanagan for always being there to

help graduate students during difficult times by effectively communicating and showing great sense of urgency.

In conclusion, I must express my very profound gratitude to my parents, Baba and Ammu, to my siblings, Rupkatha and Aurittro, and to my fiancé, Jenny, for providing me with unfailing support and continuous encouragement throughout my years of study and through the process of researching and writing this thesis. I would like to touch upon the fact that this has been a great graduate experience with so much to be grateful for and so many friends to thank for it. This accomplishment would not have been possible without my friends who are basically family at this point - Ben, Remy, Uche, Nibirh, Connor, Yushan, Niloy, Tanjid, Zarah, Samee, Shaylah, Priyo, Roy, Haroon, Sanchari, Yana and Tahmid.

Dedication

To Ammu and Jenny for your love, advice, patience, and your faith.

Thank you for always inspiring me.

Chapter 1

Introduction

Over the past few decades, thin-films have been used for decorative purposes, instrumentation coatings, and electronic devices [1–4]. Thin-films are low-dimensional materials that are less than a few microns in thickness and are created by individually condensing molecular species onto an underlying substrate [5]. Basically, thin-films are fabricated by depositing individual atoms onto substrates. This contrasts with the case of thick films, which are generally created by assembling large clusters of molecular species onto a surface [6]. Thin-film technology is continually advancing and is directly tied with new advances in materials science, such as the development of man-made super-lattices and nanoscale materials [7]. It is a key material technology for the future due to its environmentally benign character and energy efficient material conserving processing nature [8].

Thin-films can be deposited onto substrates through a variety of different methods. Typically, the growth of a thin-film starts with a nucleation process followed by a number of growth stages [9]. These stages are critically dependent on the substrate chemistry, the growth rate, and the substrate temperature [10]. Deposition conditions, such as the gases present within the deposition chamber, the length of the deposition process, the pressure within the chamber during the deposition itself, and a myriad of other factors, have been shown to determine many of the resultant thin-film properties, such as

its composition, thickness, crystal phase, and orientation [11].

In the preparation of thin-films, sputtering and chemical vapor deposition are the two primary means through which thin-films may be fabricated. Sputtering occurs through the irradiation of a substrate with energetic species [12]. In contrast, chemical vapor deposition involves the decomposition of source materials and deposition under thermodynamic equilibrium conditions [13]. Alternate deposition approaches may be employed for the preparation of more exotic types of thin-films. Atomic growth processes, for example, wherein thin-films can be prepared at the atomic level, i.e., one layer of atoms on top of another layer of atoms, can provide for very unusual thin-film properties that do not occur for the case of bulk materials, such as quantum confinement effects [14].

Carbon may be prepared in a variety of different forms. The diversity in the physical properties of these various forms of carbon stems, in large measure, from the fact that carbon atoms can bond in a number of different ways [15]. At one extreme, if the atoms are bonded in a purely tetrahedral manner within a crystalline lattice, one obtains diamond, known for its exceptional clarity and hardness [16]. At the other extreme is graphite, known for its trigonal planar type of bonding [16]. Representative bonding structures, corresponding to the cases of diamond and graphite, are depicted in Figures 1.1 and 1.2, respectively.

In addition to diamond and graphite, carbon atoms can bond in a variety of different forms. This is because carbon atoms can hybridize in the sp^1, sp^2, and sp^3 bonding configurations [16]. A variety of more recently developed forms of carbon, offering considerable opportunities for device applications, have now become available. These forms of carbon include carbon in thin-film form, C_{60} form, carbon nanotubes, graphene, and other more recently

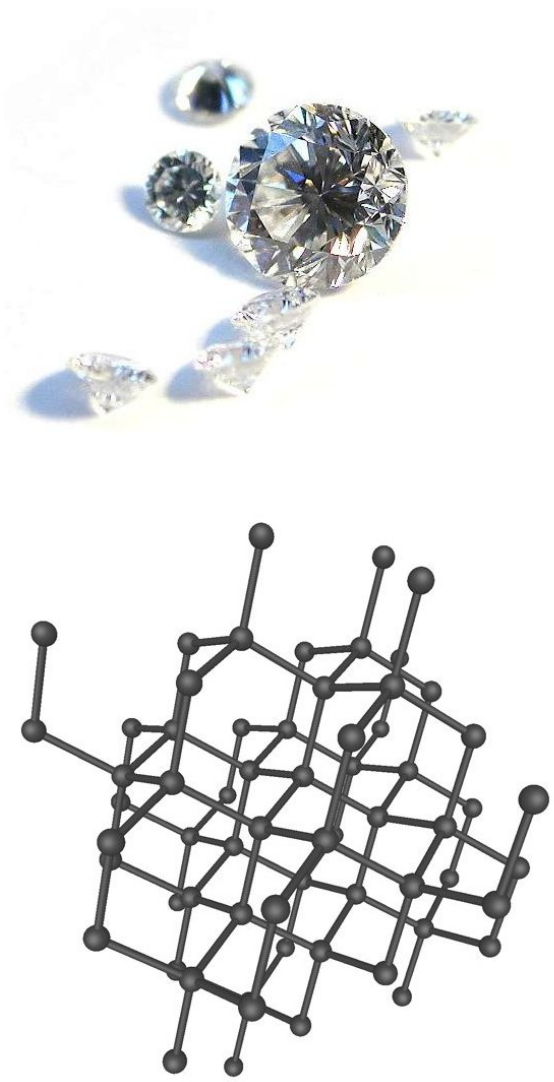

Figure 1.1: The distribution of carbon atoms within diamond. The carbon atoms are represented with the spheres while the bonds are depicted with the spokes. A picture of a representative sample of diamond is also depicted. This image is by Itub, distributed under a CC BY-SA 3.0 license. The online version of this figure is depicted in color.

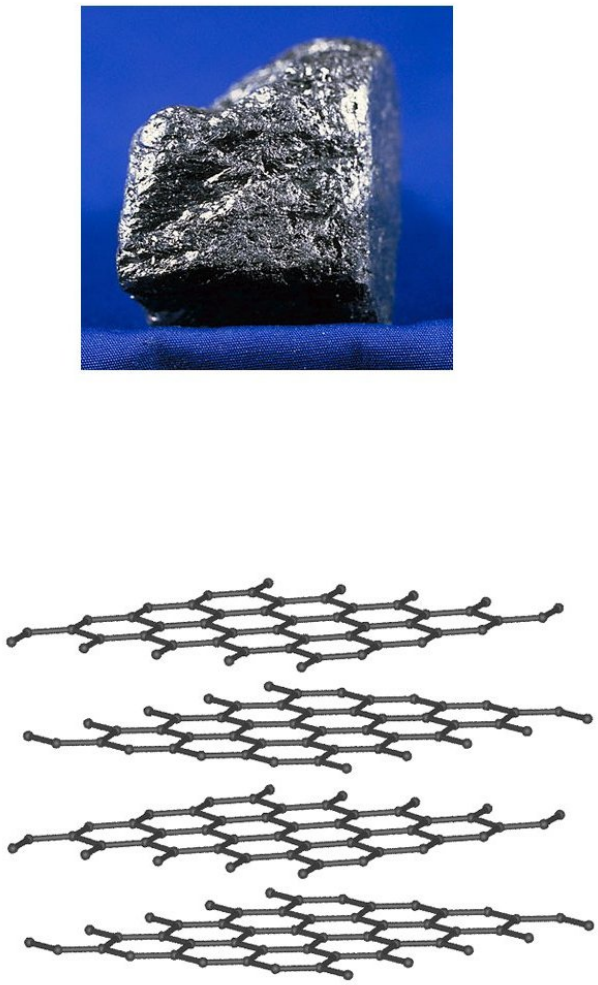

Figure 1.2: The distribution of carbon atoms within graphite. The carbon atoms are represented with the spheres while the bonds are depicted with the spokes. A picture of a representative sample of graphite is also depicted. This image is by Itub, distributed under a CC BY-SA 3.0 license. The online version of this figure is depicted in color.

discovered forms of carbon [17]. For the purposes of this particular analysis, thin-film carbon will be the focus of investigation.

Thin-film carbon may be prepared in amorphous and poly-crystalline forms [18]. Fundamental to this form of carbon is the lack of long-range order in the distribution of atoms [19]. This, of course, has profound implications in the terms of its material properties. While in an amorphous form of thin-film carbon the atoms are distributed in such a manner that the bonding lengths and bonding angles exhibit variations from atom-to-atom, in the poly-crystalline form of thin-film carbon, randomly distributed crystallites are adjacent to one another, the orientation of any particular crystallite being randomly distributed with respect to its neighbouring crystallites [20].

Thin-film carbon has found applications in a variety of industrial settings. The applications of thin-film carbon run the gamut from coating tools to a variety of machine parts [21]. In addition to their mechanical advantages, the shiny black coating of thin-film carbon coatings make them appealing for other types of applications. The automotive industry today, for example, relies on high performance piston pins, and these components are unimaginable without the use of thin-film carbon coatings [22]. Carbon is also compatible with active tissues within the human body, and this property has allowed for the use of carbon thin-films for implants for bone replacement, owing to its bio-compatibility [23]. There has also been an increase in the use of carbon thin-films in the next generation of infra-red and visible imaging systems, as can be seen in Figure 1.3. Thin-films of carbon hold the key to improved performance in a number of products. However, the achievement of these improvements relies on the selection of the best deposition process and appropriate corresponding deposition parameters [24].

The physical properties of thin-films of carbon deposited onto an under-

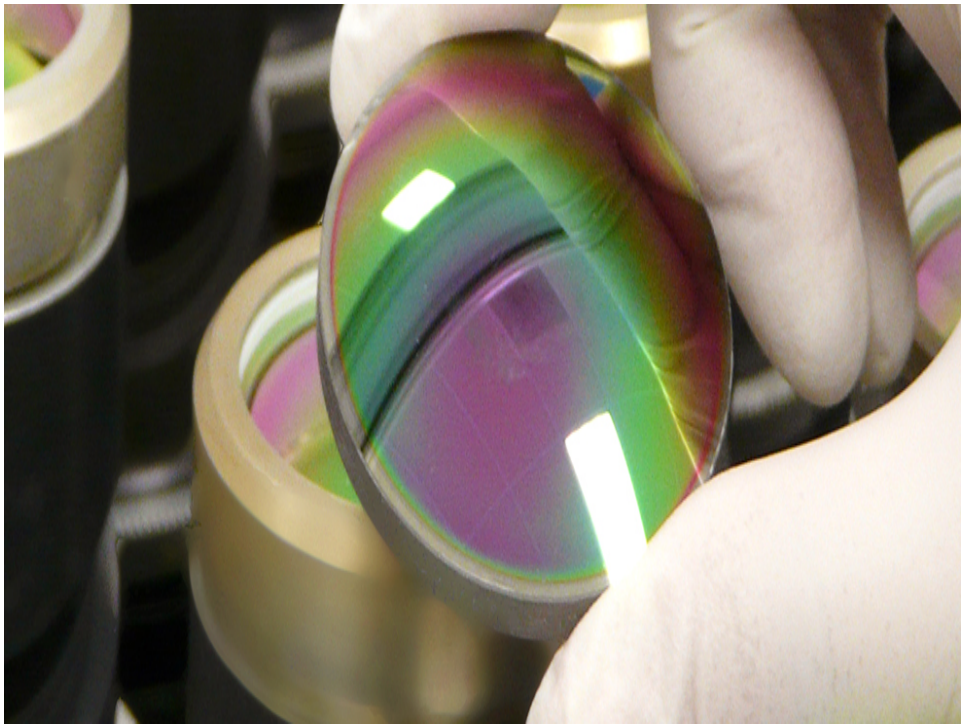

Figure 1.3: Representative image of an application of a thin-film carbon coating for an imaging purpose. This image is used with permission from II-VI Optical Systems. The online version of this figure is depicted in color.

lying substrate may be evaluated using techniques such as the scratch or indentation tests, which involve the application of an external stress to the surface of thin-film of carbon until the carbon thin-film delaminates. The stress on carbon thin-films can also be easily measured through an evaluation of the corresponding spectroscopic shift, which is in turn proportional to the amount stress [25, 26]. Spectroscopic techniques, such as Raman spectroscopy, provide information on how the carbon atoms are bonded to other atoms within the material, and have often been used for determining the sp^2 and sp^3 bonding ratios [27].

In the study of thin-film carbon, Raman spectroscopy is ubiquitous. Raman spectroscopy involves subjecting the sample under investigation to an incident beam from a laser source. The light from such a source will then interact with some of the vibrating molecules, and some of these interactions will lead to either an increase or a decrease in the energy of the corresponding photons. It is this shift in the wavelengths that is determined in the acquisition of a Raman spectrum [28]. Raman spectroscopy offers a non-destructive probe of the material in question, and it can be used to identify the type and nature of the chemical bonds that are present as well as the micro-structure of the underlying thin carbon films. The favorable economics and widespread availability of the equipment associated with Raman spectroscopy also accounts for its popularity amongst the thin-film carbon community [29].

A representative Raman spectrum, associated with a representative thin-film of carbon, is depicted in Figure 1.4. As is typically the case in analyzes of thin-film carbon, two distinct peaks are observed in the Raman spectrum associated with thin-film carbon. These peaks, denoted the D- and G-peaks, are located around 1390 and 1580 cm^{-1}, respectively, as is seen in Figure 1.4.

In thin-film carbon analyzes, one typically fits a two-peak function to such a Raman spectrum [30], a representative two-peak fit being depicted in Figure 1.5, the experimental data set employed in Figure 1.5 being the same as that depicted in Figure 1.4. Many of the properties of thin-film carbon have been correlated with the amplitude ratio [1] or the integrated intensity ratio [2] between the two peaks, i.e., A_D/A_G or I_D/I_G, respectively, where A_D and A_G represent the amplitudes found from the peak fits while I_D and I_G correspond to the integrated intensities, i.e., integrations over the peaks that are found from the fits.

Ferrari *et al.* suggests that the sp^2 cluster sizes and their distribution can be identified through the measurement of Raman peak amplitude ratios and their widths in diamond-like carbon (DLC) [25]. Historically, several authors have considered the peak amplitude ratio instead of the integrated intensity ratio, and vice versa [30–34]. This raises an important question: is the amplitude ratio, A_D/A_G, related to the integrated intensity ratio, I_D/I_G, for the case of thin-film carbon [31]. These ratios are considered important as they serve as an indicator of the quality of the corresponding DLC material [35].

In this thesis, thin-films of carbon, deposited using the plasma enhanced chemical vapor deposition (PECVD) and magnetron sputtering techniques, will be characterized through the use of Raman spectroscopy. Peak decomposition will be performed for all of the acquired Raman spectra. Thin-films of carbon, prepared using a variety of different deposition conditions, will be considered. Raman source wavelengths, of 325, 442, and 633 nm, will be employed in order to acquire the Raman spectra corresponding to these samples of thin-film carbon. The aim of this analysis is to ascertain as to whether or not the peak amplitude ratio, A_D/A_G, is related to the cor-

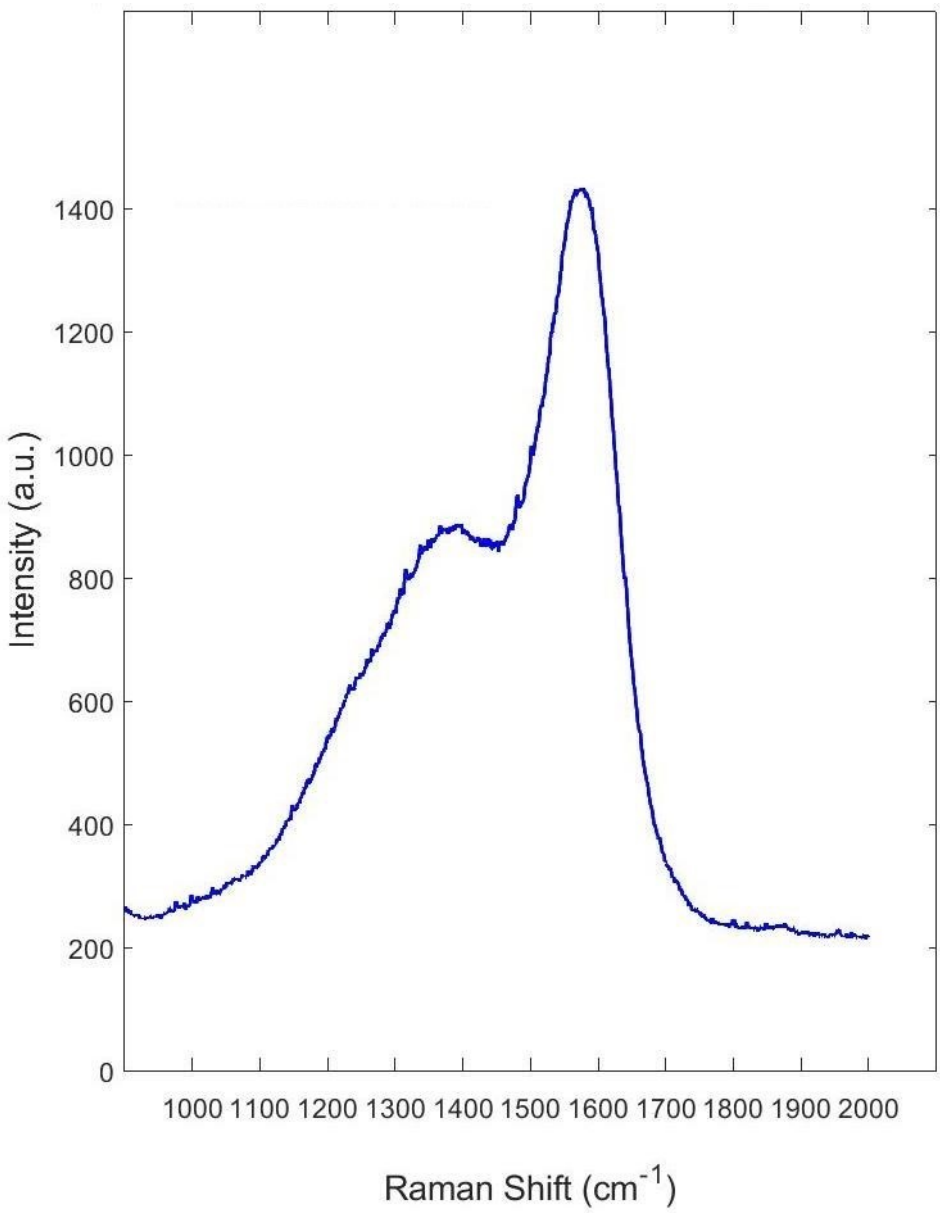

Figure 1.4: A representative Raman spectrum corresponding to thin-film carbon. Created by Ashraf Ahsan, used by permission. The online version of this figure is depicted in color.

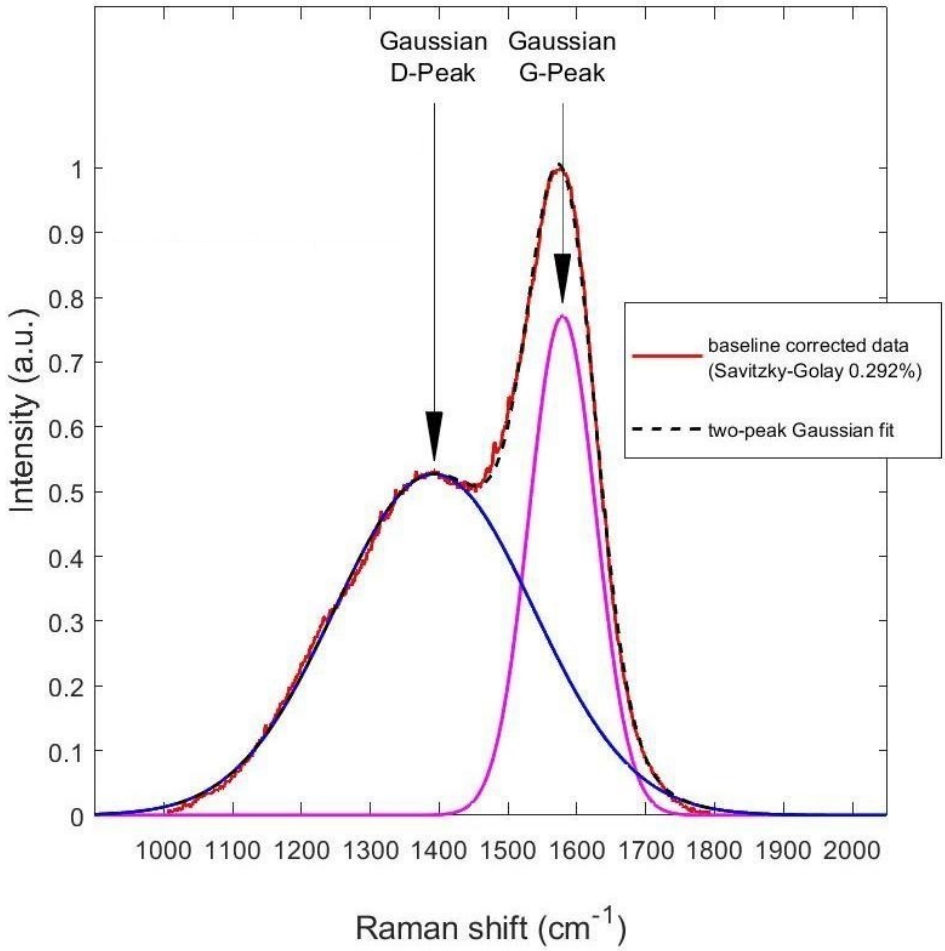

Figure 1.5: A representative Raman spectrum. A peak decomposition of this spectrum, into D- and G-peaks, is depicted. The experimental data depicted in this figure is the same as that shown in Figure 1.4. Created by Ashraf Ahsan, used by permission. The online version of this figure is depicted in color.

responding peak intensity ratio, I_D/I_G. This analysis is performed over a relatively broad swath of thin-film carbon genome. The dependence of this relationship on the source wavelength will be probed.

This thesis is organized in the following manner. In Chapter 2, the background for this research is provided. Then, in Chapter 3, the experimental methodologies, employed for the purposes of this analysis, are described. The results obtained from the experiments that are performed are then analyzed in Chapter 4. Finally, conclusions are drawn and some suggestions for future investigation are provided in Chapter 5.

Chapter 2

Background

2.1 Overview

Thin-films of carbon have attracted the attention of researchers since the 1970s [36]. At present, they are being used for a number of important industrial applications. Since these thin-films of carbon fulfill various important industrial functions, such as providing a barrier against corrosion and providing protection against contamination [37], there is an interest in identifying how the properties of a carbon thin-film may be optimized for the particular application in question. Clearly, this will require further scientific analyzes on the properties of thin-film carbon. This thesis aims to contribute towards the realization of this goal.

In this chapter, the background for this work is provided. First, the different forms of carbon are discussed. Then, a variety of approaches to the preparation of diamond-like thin-film carbon are presented. Means of reducing the presence of contamination are then presented. The electromagnetic spectrum is then described. A variety of spectroscopic approaches, that may be employed in the study of thin-film carbon, are then presented. Finally, the key elements of Raman spectroscopy are introduced.

This chapter is organized in the following manner. In Section 2.2, the different forms of carbon are discussed. Then, DLC thin-film deposition tech-

niques are introduced in Section 2.3. The challenges that are encountered owing to the presence of contamination are then discussed in Section 2.4. Later on, the electromagnetic spectrum is presented in Section 2.5. This is followed by a brief discussion on the various spectroscopic techniques that may be used in the study of thin-film carbon in Section 2.6. Finally, Raman spectroscopy is discussed in Section 2.7.

2.2 Carbon allotropes

Since the 17th Century, diamond has been the subject of numerous scientific investigations [38]. In addition to being clear and sparkling in appearance, diamond is also amongst the hardest substances on this planet [39]. For these reasons, diamond has naturally attracted a considerable amount of attention. Through an examination of the properties associated with diamond, it has been established that it represents a pristine form of carbon arranged in a tetrahedral crystal structure [40]. As was mentioned in the introduction, it has been observed that carbon atoms can also crystallize in a trigonal form, known as graphite, as seen in Figure 1.2, which has a crystalline structure that is distinct from that of diamond [40]. Diamond has strong tetrahedral sp^3 bonds for all axes, whereas graphite has strong sp^2 bonds along only two axes but weak bonds on the third axis. This difference accounts for the differences in the physical properties of diamond and graphite [41], these being tabularly presented in Table 2.1.

The hardness of diamond has naturally attracted a considerable amount of interest in the possible uses of diamond for industrial applications. Clearly, for milling and drilling applications, diamond offers a considerable advantage [42]. Unfortunately, naturally occurring diamond, while exhibiting this

Table 2.1: The properties of diamond and graphite [38].

Property	**Diamond**	**Graphite**
Appearance	Transparent	Black, shiny
Hardness	Very hard	Soft and slippery to touch
Thermal conductivity ($W\ m^{-1}\ K^{-1}$)	Very poor $\sim$ 2200	Moderate $\sim$ 150
Electrical conductivity	Poor	Good conductor
Density (g/cm^{-3})	3.515	2.267
Uses	Jewellery and drilling	Dry cell and lubricant
Crystal structure	Rigid, tetrahedral structure with strong covalent bonds	Layers can slide, strong hexagonal layer structure with weak Van der Waals forces between layers
Bonding	Each carbon atom is covalently bonded to 4 others	Each carbon atom is covalently bonded to 3 others
Electron configuration	No delocalized electrons	Delocalized electrons
Orbital hybridization	sp^3	sp^2
Heat capacity ($J\ mol^{-1}\ K^{-1}$)	6.155	8.517

extreme hardness, is very rare and expensive to purchase. Accordingly, the use of natural diamond for such applications has only occurred for the very highest-end applications. Clearly, in order for diamond to be used over a broader base of applications, synthetic forms of diamond must be fabricated.

Research aimed at producing synthetic forms of diamonds began in earnest in the late 1800s [38], when hard crystals of carbon were being formed by heating charcoals in a furnace [43, 44]. While these initial efforts failed to synthesize actual diamond, with the advent of modern high-pressure and high-temperature deposition equipment, the manufacturing of synthetic forms of diamond became a reality by the middle of the 20th Century. Today, synthetic diamonds can be fabricated through the use of high-temperatures and high-pressures. Though synthetic diamonds are expensive to fabricate,

this expenditure is much less than the purchase of their naturally occurring counterparts [44].

In addition to these two crystal forms of carbon, there are a variety of non-crystalline forms of carbon. Since carbon atoms can bond in a variety of different forms, it is referred to as being an allotropic material [15]. Carbon atoms can be arranged in both amorphous and poly-crystalline forms. Since the 1970s, thin-film forms of carbon have been identified as being members of the carbon genome, and are currently primarily being used as a coating for a variety of different substrates [43]. Its ability to coat onto an underlying substrate of seemingly arbitrary geometry, thereby enhancing its resistance to wear, has obviously enhanced its appeal for military and industrial applications.

Thin-films of carbon can be deposited cheaply and uniformly onto a variety of underlying substrate types. Indeed, it was economic factors that prompted the preparation of thin-film carbon from the vapor phase in the first place, the 1971 deposition of thin-film carbon by Chabot and Aisenberg, of the Space Science Division of the Whittaker Corporation from Waltham, Massachusetts [45], being one of the first reported depositions of thin-film carbon. Various methods for thin-film carbon deposition have since emerged, such as sputtering and more sophisticated processes, such as PECVD [46]. Depending on the application at hand, the right deposition method must be carefully selected.

Thin-films of carbon that are deposited from the vapor phase are always deposited onto an underlying substrate. The selection of the substrate is often determined by the application at hand. For the depositions employed for the purposes of this analysis, thin-films of carbon were deposited onto a titanium alloy through the use of PECVD or magnetron sputtering. The

titanium substrates used for this case is Ti6Al4V, which is a commonly found titanium alloy with 6% aluminum, 4% vanadium, 0.25% (utmost) iron, 0.2% (utmost) oxygen, and almost 90% titanium, by weight [47]. This alloy is commonly employed in a wide variety of industrial applications.

Thus far, a number of deposition processes have been studied in detail. While there is research on the effect of the substrate on the thin-film carbon properties, what remains unknown is how the shape and the type of the substrate influences the properties of the resultant thin-films of carbon; the only analysis that could be found on the influence that substrate geometry plays in shaping the thin-film carbon properties was that reported by Bobzin *et al.* [48]. While a lot of work has been performed on the thin-film carbon properties that arise from depositions onto planar glass or crystalline silicon substrate [48–50], there is a considerable scope available to investigate the properties of thin-films of carbon deposited on Ti6Al4V substrates. This can be done using the two most popular deposition techniques, namely PECVD and magnetron sputtering. In this thesis, Raman spectroscopy, performed for three different source wavelengths, will be employed for the purposes of such an analysis, samples of thin-film carbon, prepared through PECVD and magnetron sputtering, being considered.

Unprocessed titanium is typically coated with a native oxide layer, which makes adhesion a challenge, requiring the use of interlayers, i.e., a layer of material acting as an interface between the underlying substrate and the thin-film of carbon [51]. While this work focuses on the relationship between the A_D/A_G and I_D/I_G ratios, a variety of deposition parameters and sp^2 to sp^3 bonding ratios, will be considered in this analysis. The dependence of the results on the source wavelength will be a key focus of this inquiry, three different Raman sources being considered for each thin-film of carbon that

is considered. While beyond the scope of this analysis, understanding the influence of the deposition parameters on the resultant thin-film of carbon will allow for the selection of "optimal" deposition parameters.

As has been mentioned before, carbon's wide range of physical properties arises because of the diverse range of bonding that can occur within it. Carbon atoms can partake in sp^1, sp^2, and sp^3 bonding [52]. sp^1 bonding is comparatively less common compared with sp^2 bonds for the trigonal crystalline structure, leading to a black and soft form of carbon, i.e., graphite, and sp^3 bonds for the tetrahedral structure, leading to a transparent and hard form of carbon, i.e., diamond. Forms of carbon with both sp^2 and sp^3 bonds are also available, with properties that lie between these two extremes [53]. Overall, thin-films of carbon have both sp^2 and sp^3 bonds and the quality of a thin-film of carbon may be determined through the ratio of the sp^2 to the sp^3 bonding fraction. If the sp^3 bonds are more numerous, then the coatings exhibit diamond-like properties. If the sp^2 bonds are more numerous, then graphite-like characteristics are exhibited. Thin-films of carbon, with plenty of sp^3 content, are now being employed over a wide range of applications in the automotive, milling, drilling, industrial, and military sectors, as was discussed by Gilo *et al.* [54–56].

Carbon based atomic orbitals can form new hybridized orbitals, resulting in completely different types of chemical bonding and properties, as is seen in Figure 2.1. Carbon has four valence electrons with sp^3 bonds for pristine diamond, each of them being allocated to an sp^3 orbital with σ bonds, resulting in diamond's hardness [56]. When the carbon atoms bond in sp^2 form, such as in graphite, three out of the four valence electrons form σ bonds. The outermost valence electron forms a π orbital with π bonds in normal orientation with the other σ bonds. These π bonds are weaker than

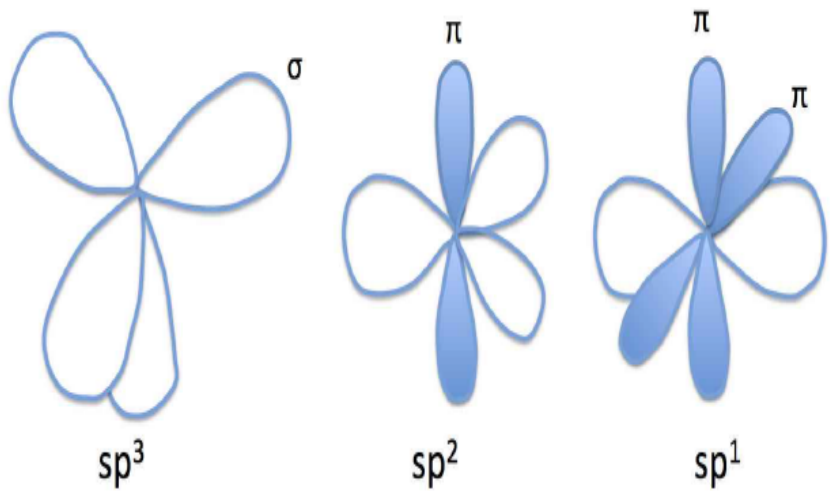

Figure 2.1: The hybridizations available to carbon atoms within thin-film carbon. This figure is after Robertson *et al.* [57]. Created by Jonathan Laumer, used by permission. The online version of this figure is depicted in color.

the σ bonds, which is why the bonding is weaker on the axes that include π orbitals. In the case of the sp^1 bonding configuration, carbon atoms form two π bonds in x and z axes, but two σ bonds are formed with the two valence electrons along the x axis.

2.3 DLC thin-film deposition and application

Chemical vapor deposition (CVD) and physical vapor deposition (PVD) are two widely used techniques that have been employed to deposit thin-films of carbon [58]. CVD is commonly employed using the plasma enhanced version of this deposition process, known as PECVD. A plasma is created by applying a voltage across an inert gas, thereby enabling thin-film deposition. This process enables the cracking of molecules within the plasma, the species associated with these cracked molecules then being deposited onto the heated substrate, thus permitting the fabrication of a thin-film of carbon [45]. The resultant thin-film carbon coating is found to be relatively uniform in thickness. In a PVD technique, however, such as sputtering, an inert gas is ionized in order to create the plasma. The carbon source material is then bombarded using the ions, which blasts carbon atoms from the source into the vacuum. The carbon atoms then get deposited onto a substrate that is in the line-of-sight of this beam of carbon atoms [58].

A fair amount of hydrogen is incorporated into thin-films of carbon fabricated using PECVD, as many of the source gases used for these depositions are based on hydro-carbons. The PVD process leads to a shadowing effect, unlike the case of CVD. In PECVD, the gaseous basis material comes from all directions, whereas in sputtering, it is only from a single direction. Other methods are also available for the deposition of thin-films of carbon, such as

ion beam, pulsed laser deposition, cathode arc, and a variety of other techniques [45]. It is possible to characterize the various forms of DLC using a ternary phase diagram. In such a phase diagram, a given thin-film of carbon is specified with respect to its sp^2, sp^3, and hydrogen contents. Materials, such as glassy soot and evaporated forms of thin-film carbon with a higher sp^2 content, are in the left corner. Other forms of thin-film carbon, with finite hydrogen content, can also be produced, some being found in the lower right corner of the ternary phase diagram. In the upper corner, materials with a higher sp^3 content are found [57]. As the sp^3 bonding content increases, the thin-film carbon starts to exhibit a greater DLC character, such as increased hardness and density and decreased electrical conductivity [59].

As has been mentioned earlier, thin-films of carbon with higher sp^3 bonding content exhibit great hardness, durability, and biocompatibility [57]. As the smooth coatings that arise from such a deposition have a very low coefficient of friction, they can be used to coat machine parts and tools in order to increase their life-time [57]. Apart from their mechanical benefits, thin-films of carbon can also be used for ornamental purposes. The glossy black coating of such a thin-film feels good and looks beautiful, making them highly desirable for cosmetic jewellery applications. For the purposes of such an application, it is crucial to be consistent and to achieve a similar quality on all types of surfaces [52].

The automotive industry has improved vehicle performance using thin-films of carbon. Stronger cars can be built with more durable parts, such as pistons that can withstand greater pressures, using such coatings. An example of the application of DLC coatings is the Dodge Challenger, where gains in performance have been achieved through the use of thin-film carbon compared with previous models [55]. In a similar way, the drilling and milling

industries have benefited considerably from the hardness and durability of thin-film carbon coated tools [52]. A noteworthy increase in the durability of cutting apparatuses, along with a corresponding decrease in the surface roughness of cut materials, have been amongst the benefits of coatings using thin-films of carbon.

Carbon exists abundantly in nature and can readily bond with hydrogen, oxygen, and nitrogen atoms to form intricate molecules. Carbon is also compatible with active tissues. Therefore, thin-films of carbon can be utilized for implants, such as in hip replacements, owing to its biocompatibility [60]. Rotating parts need to have almost frictionless surfaces in order to avoid metallic wear. Investigations on the biocompatibility of thin-films of carbon coated parts have been carried out by Allen *et al.* [56], with a demonstration that it is harmless in nature. Thus, carbon coatings offer virtually unlimited potential in the biomedical arena.

There also seems to be a benefit to using thin-films of carbon in optical applications due to its enhanced resistance to mechanical impact and corrosion. In the case of forward looking infra-red cameras, used for military applications, it has been observed that coating the lens with a thin-film of carbon can reduce the reflection of the indicator onto itself from the front lens [55].

2.4 Challenges due to the presence of contamination

Even if a thin-film of carbon has a high sp^3 bonding content, there is no assurance that it will stick to the underlying substrate. This is a serious problem if the layer of thin-film carbon is to be effective [51]. To achieve

proper adhesion, the substrate must be free of dirt prior to deposition. The surface must be cleaned using soapy water and acetone to free it from organic contamination and metal oxidation, i.e., rust. Oxygen can reduce the inter-atomic bonding strength and can frustrate the adhesion of the thin-film of carbon onto the underlying substrate. Thus, the substrate needs to undergo cleaning using the plasma in the vacuum chamber in order to reduce the oxygen layer while employing any of the commonly used widely available deposition techniques [25].

2.5 The electromagnetic spectrum

As the name suggests, electromagnetic radiation possesses both magnetic and electrical components. Electromagnetic radiation includes what we normally refer to as light, as well as other forms of radiation with shorter or longer wavelengths. All forms of electromagnetic radiation travel at the speed of light in vacuum, and can be characterized in terms of their wavelength, both in vacuum or air, and by wave-numbers or frequencies in vacuum. The electromagnetic spectrum, shown in its totality in Figure 2.2, is divided into a number of bands, from low-energy radio-waves to high-energy gamma-rays. The laser sources employed for Raman spectroscopy typically are in the visible range to the ultra-violet range of the electromagnetic spectrum.

2.6 Spectroscopic techniques

Spectroscopy plays an important role in allowing for a probe of the chemical content of materials. It relates to the absorption, scattering, and

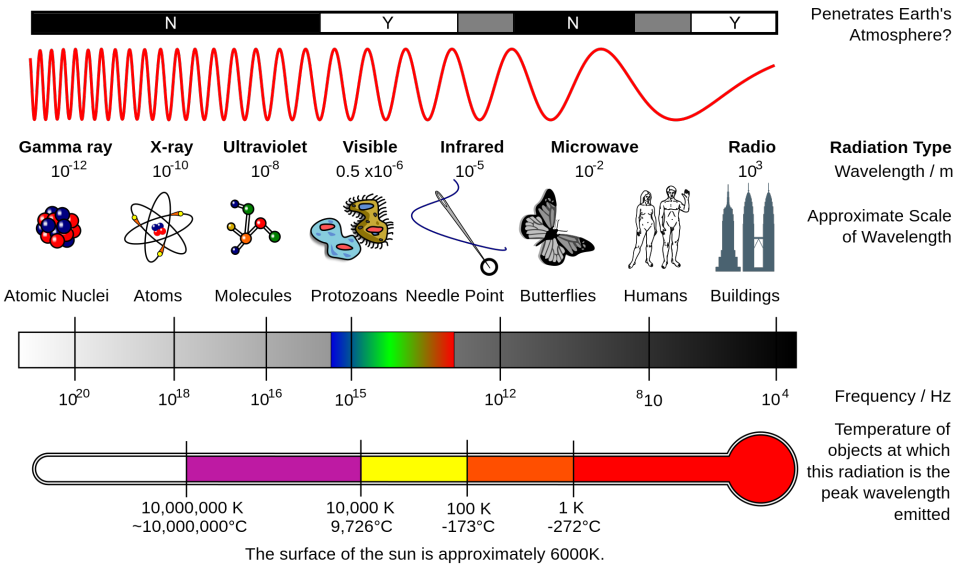

Figure 2.2: A representation of the electromagnetic spectrum. This image is by Inductiveload, distributed under a CC BY-SA 3.0 license. The online version of this figure is depicted in color.

emission of electromagnetic radiation by atoms and molecules. Quantum mechanics may be used for the interpretation of results acquired through spectroscopy [61].

In the middle of the 16th Century, experimental methods of spectroscopy were becoming more common, at least for the visible region of the electromagnetic spectrum. Newton had also started to perform his famous experiments on the dispersion of white light using triangular prisms [62]. By the 1860s, Bunsen and Kirchhoff began integrating prism spectroscopy into analytical instruments. This marked the origin of the flame tests on elements and also the Sun, as these new instruments were being used to observe the emission of spectra of samples in flames [63].

The fitting of spectral lines in a visible spectrum of atomic hydrogen to a mathematical formula by Balmer shed light on the close relation between experiment and theory in spectroscopy [64]. The theoretical part, based on Newtonian mechanics, kept running into difficulty until the development of quantum mechanics by Erwin Schrödinger in 1926 [65]. The interpretation of spectroscopic data proved challenging, and approximations invariably had to be made to make the analysis manageable, except for the case of the simplest atoms. The situation began to change due to the advent of fast computers, thereby requiring fewer approximations, bearing in mind that predictions are still not uncommon for fairly small molecules.

A measurement of thin-film properties, such as the chemical composition, the crystalline structure, the mechanical, and electrical aspects, is required in order to study thin-film materials and devices. There has been rapid progress in the evaluation of surface and thin-film of semiconductor materials, causing an increase in the number of largely available methods. The choice of spectroscopic technique relies on its reproducibility, the number

of detectable elements, the area, the depth, and the sensitivity of both the source and the sample. There exists a correlation between growth conditions and the properties of a deposited thin-film [6]. Table 2.2 provides a list of common spectroscopic techniques currently being used in the field.

In 1928, Raman and Krishnan discovered Raman scattering [66]. Since then, numerous research papers have been published on this subject. In Raman spectroscopy, the scattered light is usually observed in the direction perpendicular to the monochromatic light incident upon the material. A decrease or increase in the wavelength of the emitted photons is caused by the vibrational frequencies, resulting in Stokes and anti-Stokes lines [28], respectively, as is seen in Figure 2.3. Basically, the molecular vibrations disturb electron clouds around the molecules and it is possible for the vibrational and optical excitations to interact, causing Raman scattering [28].

2.7 Raman analysis of carbon thin-films

Chandrasekhara Venkata Raman (1888-1970), born in the southern part of India, discovered what is now referred to as the Raman effect [66]. On his way to India from England, he demonstrated that the blue shade of the ocean is not due to the blue sky's reflection. Instead, Raman showed, using a diffraction grating, that the maximum spectral density for the sky and the ocean occur at different wavelengths. He thus concluded that there must be another explanation for the blue color of sea [67]. Later, it was observed by him that the scattered light within water experiences a frequency shift and that this change in the frequency is the reason for the blue color of the sea, i.e., owing to the inelastic scattering of light by water molecules [66]. In contrast, the shade of the sky is due to elastic scattering, known as Rayleigh

Table 2.2: Examples of spectroscopic techniques involving an exchange of energy between a stream of photons and the sample.

Region of electro-magnetic spectrum	**Spectroscopic technique**
γ-ray	Mössbauer spectroscopy
X-ray	X-ray absorption spectroscopy
	X-ray fluorescence
UV/Vis	UV/Vis spectroscopy
	Chemiluminescence spectroscopy
	Fluorescence spectroscopy
	Atomic emission spectroscopy
	Phosphorescence spectroscopy
	Atomic fluorescence spectroscopy
	Atomic absorption spectroscopy
IR	Infra-red spectroscopy
	Raman spectroscopy
Microwave	Microwave spectroscopy
Radio-wave	Electron spin resonance spectroscopy
	NMR spectroscopy

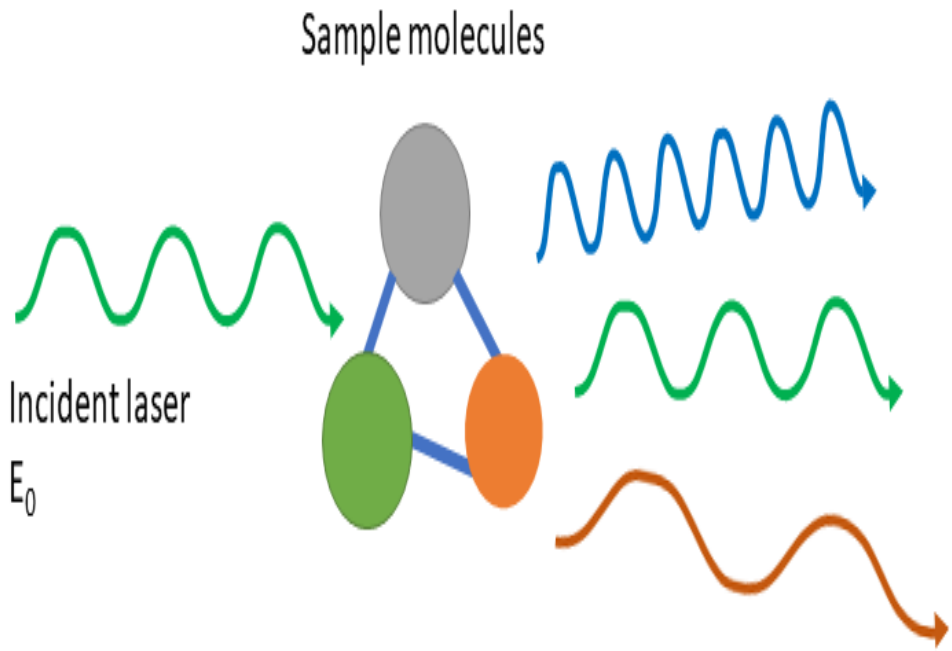

Figure 2.3: A representation of Raman scattering contrasted to Rayleigh scattering [3]. Created by Ashraf Ahsan, used by permission. The online version of this figure is depicted in color.

scattering [60].

2.7.1 Raman setup

The basic components of a Raman spectroscopic experimental set-up are as depicted in Figure 2.4. The major components include: (1) an incident source laser beam for excitation, (2) an optical element in order to focus the beam and filters in order to achieve the desired intensity on the sample, and (3) a detector or spectrograph and a camera so as to capture the scattered light.

A band-pass filter, known as the dichroic beam splitter, is used to separate the Rayleigh scattered light from the Raman scattered light by confining the range within the Raman spectrum [60]. Each hybridization state experiences different scattering, and the change in wavelength/frequency is known as the Raman shift. It is the difference between the reciprocals of the excitation and scattered wavelengths [68], i.e., the Raman shift, that is measured in a Raman spectrometer.

The emission or absorption of energy causes a change in the frequency of the light. In the case of a down-shift by a phonon emission, a Stokes shift is observed, whereas in the case of phonon absorption, an up-shift in the frequency, i.e., an anti-Stokes shift, takes place [28]. The Stokes shift is the focus of my analysis here, as the intensity of the scattering is much more significant for the Stokes shift than for the anti-Stokes shift. This is due to the lower population of excited states because of the Boltzmann distribution for molecules in the higher energy states [68]. The biggest advantage of Raman spectroscopy is its non-destructive nature and the widespread availability and favourable economics associated with the use of the required

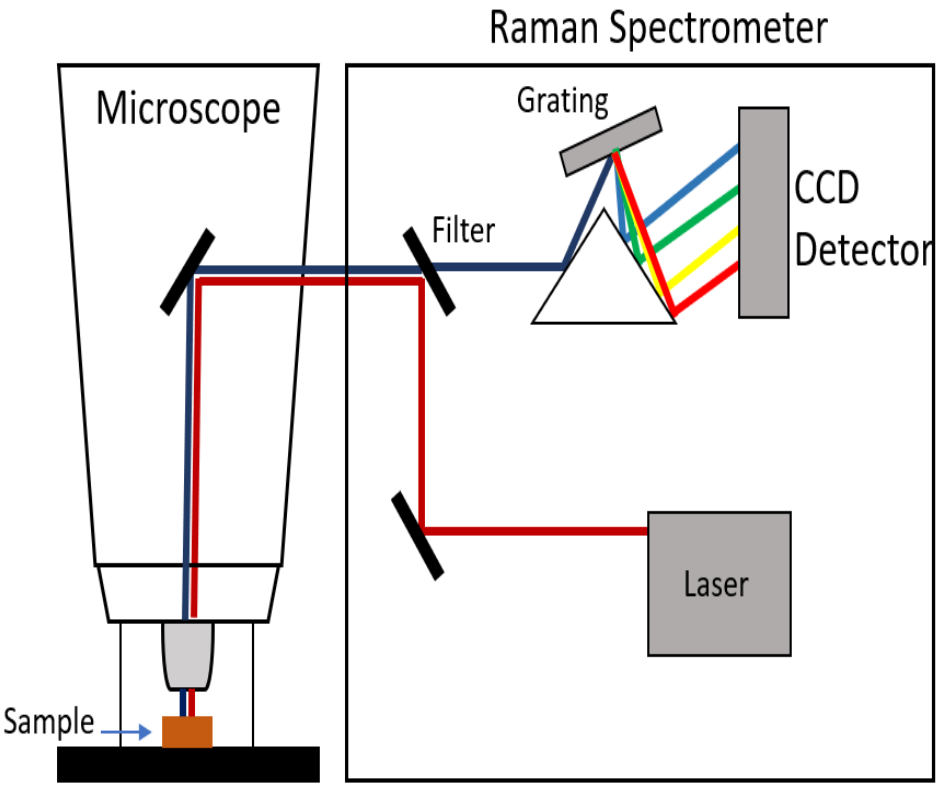

Figure 2.4: A representation of the basic components of a Raman spectrometer. Created by Ashraf Ahsan, used by permission. The online version of this figure is depicted in color.

equipment.

Laura *et al.* have investigated the optimal choice of laser source wavelength and substrate needed in order to collect the Raman signals, which can get overpowered by background noise [69]. It should be noted that the intensity of the Raman scattering is proportional to the fourth power of the incident light source frequency. Researchers are often under a dilemma on the kind of source excitation wavelength for the laser source to use. The choice of wavelength and substrate entirely depends on the quality of the sample material [70]. Evaluations have previously been performed by breaking down the work into studying the importance of standardization of the parameters associated with Raman spectroscopy.

Previously, Ferrari has presented the effects of multi-wave Raman for the excitation to observe the peak dispersion of ta-C:H:N samples composed of 29% N and 26% H atomic weight [71]. There exists an evident potential to explore the outcome of using multiple source wavelengths to conduct Raman analysis on materials, such as thin-films of carbon with titanium substrates [44]. It has been demonstrated, by Neuville and Matthews [25], that there is no basic difference between the deposition physics of diamond and DLC, but it is only a question of the variations between the deposition parameters and the growth conditions which allow for more crystalline structures and dense materials.

2.7.2 The D- and G-peaks

In most studies of thin-film carbon involving the use of Raman spectroscopy, two distinct peaks are observed, one between 1350 and 1365 cm^{-1} another being between 1580 and 1620 cm^{-1}, these peaks being commonly

referred to as the D- and G-peaks, respectively [30]. Originally standing for diamond and graphite, the former band is generally known as the D-peak and the latter as the G-peak. As the diamond band is always observed to be at around 1332 cm^{-1}, the letter D had to be redefined. It has been argued, by some authors, that the D-band represents a disorderly network of sp^2 coordinated clusters [27]. When using the intensity ratio, I_D/I_G, for quality control of thin-films of carbon being used in the computer industry, the users are likely to face trouble if the excitation wavelength transitions to lower wavelengths as the intensity of D-peak tends to drop to zero in the ultra-violet range [70]. Pócsik *et al.* observed that the D-peak's frequency increases with excitation energy, while the intensity decreases [72]. On the other hand, the intensity and frequency of the G-peak only changes a little. From the study of the Raman specta associated with microcrystalline graphite, the D-peak arises from the phonons near the Brillouin zone's edge, which are preferentially excited by low energy photons due to small optical transitions near the edges [3]. In contrast, the zone centre is where the high energy photons produce optical transitions by exciting the zone centre phonons, i.e., the G-peak [3].

As shown by Muller *et al.*, the oxygen/carbon ratio in DLC films results in a proportional increase in the measured G-peak position. It has also been shown that films containing a constant amount of hydrogen or nitrogen exhibit a linear increase in the G-peak position with the deposition temperature. This correlates with the electron energy loss spectroscopy (EELS) results indicating that thin-films of carbon deposited at higher temperatures possess a higher sp^2 bonding content and a lower sp^3 bonding content [73]. In fact, as the G-peak moves towards lower frequencies, its wear resistance increases. It is argued that a wear resistant carbon coating

will have higher sp^3 bonding and that the G-peak position will shift towards lower frequencies. The G-peak position is used to monitor the DLC film quality industrially and this peak shift is enough to give an insight into deposition quality variations [3].

2.7.3 The I_D/I_G and A_D/A_G ratios

The analysis of Raman intensity provides a very powerful tool for understanding and characterizing the modifications in the crystalline/amorphous structure due to changes in the symmetry, long-range order, and nanostructure. The intensities allow us to obtain information, as seen in Figures 2.5 [74, 75] and 2.6 [76], about the composition, the chemical environment, and the different phases that are present within the material [77]. Table 2.3 provides insight on the relationship of the peak positions and peak amplitude ratios based on the Raman spectra acquired using a He-Ne laser of 633 nm by Dillon *et al.* on thin carbon films deposited using the LASER-ARC technique [1].

Table 2.3: Peak fit parameter for a variety of different Raman spectra. This data is from Dillon *et al.* [1].

Sample	D-peak position (cm^{-1})	G-peak position (cm^{-1})	A_D/A_G
30 °C	1355	1530	0.9
500 °C	1367	1581	6.4
Particle graphitic cluster	1320	1586	0.8
Covering film	1335	1511	0.6
Target	1333	1580	0.5

The parameters for the two-peaks, such as their positions, widths, and their integrated intensity ratios, can be used to characterize the thin-films of carbon. Similarly, Table 2.4 shows the Raman spectra for DLC coatings with

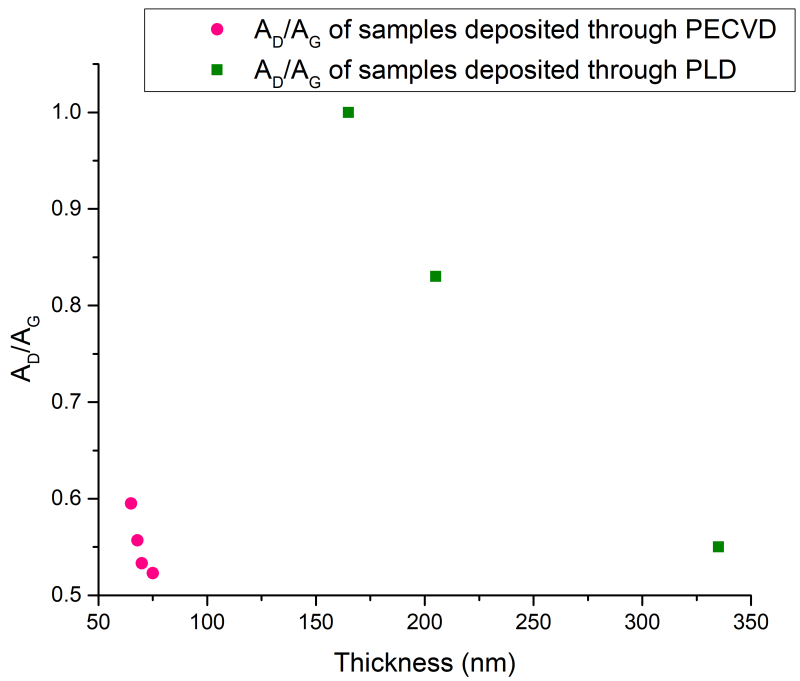

Figure 2.5: The role that film thickness plays in determining the A_D/A_G ratio. The experimental data is from Modabber *et al.* [74] and Paul *et al.* [75], for thin-film carbon. Digitized by Ashraf Ahsan, used by permission. The online version of this figure is depicted in color.

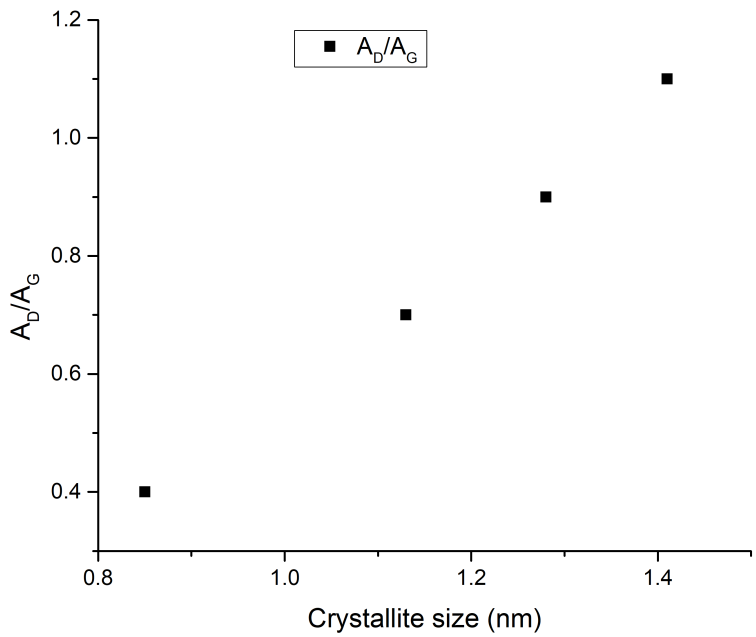

Figure 2.6: The role that crystallite size plays in determining A_D/A_G for thin-film carbon. The experimental data is from Madhusmita *et al.* [76]. Digitized by Ashraf Ahsan, used by permission. The online version of this figure is depicted in color.

different deposition temperatures and source excitation wavelengths. Here,

Table 2.4: Peak decomposed Raman spectral data corresponding to DLC coatings deposited with different temperatures and source excitation wavelengths. This data is from Varade *et al.* [2].

Sample	D-peak position (cm^{-1})	G-peak position (cm^{-1})	I_D/I_G
Si RT (514 nm)	1345.3	1545	0.53
Si 300 (514 nm)	1370.2	1551.8	0.83
Si RT (785 nm)	1221.6	1455	0.15
Si 300 (785 nm)	1252.6	1477.4	0.25

the peak intensity area is found to proportionally increase with respect to the deposition temperature [2]. As can be seen, a baseline corrected and fitted spectrum, showing the areas under the peaks and eventually calculating their ratios, may also be sufficient for sample identification [78].

Marchon *et al.* [79] and Yoshikawa [80] are among some of the groups who have studied the behavior of Raman spectral intensities as a function of the carbon thin-film structure and/or deposition conditions. The I_D/I_G ratio has been found to correlate with the observed properties of the DLC films and abrasive wear rates are observed to be inversely proportional to the I_D/I_G ratio. It is also believed that the increase in the D-peak intensity is due to increases in the size or the number of graphitic crystallites and that this also results in a decrease in the corresponding optical bandgap. It should be noted that below a certain critical size, estimated to be 2 nm, these crystallites do not contribute to the Raman spectra and its D-peak. So it is advisable to use the I_D/I_G ratio to monitor the thin-film quality on or after the crystallites reach a critical size. If no structural changes are made, then the increase in the I_D/I_G ratio is accompanied by a decrease in the

background slope of the Raman spectrum, for both the D- and G-peaks [3].

Finally, it is not always clear if the ratio of peak amplitudes or peak areas should be used. Researchers employing two-Lorentzian-peak fits report peak amplitude ratios, while others, employing the two-Gaussian-peak fits, report the peak integrated area ratios. The difference is not so important for disordered graphite, as the peak widths are similar, but this is not the case for other types of thin-film carbon. In the case of the latter, the broadening of the D-peak is correlated with the distribution of clusters, of varying order and dimensions. Thus, information about the less distorted aromatic rings is found in the peak amplitude and not the width [30].

2.7.4 UV-Raman spectroscopy

Recent developments in ultra-violet (UV) laser technology have allowed for the development of Raman spectroscopy in this range of the electromagnetic spectrum, making it possible to use this technique in a research capacity for industry. The intensity of a Raman signal is dependent on the wavelength, i.e., fourth power dependent on the excitation frequency, this can be expressed as

$$I_R \propto I_0(v_0 \pm v_i)^4 N, \tag{2.1}$$

where I_R denotes the Raman signal intensity, I_0 refers to the intensity of the excitation source, v_0 is the intensity of the excitation source, v_i is the frequency of the Raman scattered particle, and N is the density of molecules. This shows how excitation though the use of a UV source, which has a shorter wavelength or a higher frequency, that high Raman scattering efficiency can be attained. The advantage of using UV excitation is to probe sp^3 bonding, unlike visible excitation, which is implied to look at the sp^2 bonding.

Despite the improvements, it is challenging to make this technique widely available, as the cost of such a laser is very high (greater than $10K) [81] and there is a need for additional utilities, such as water, water drainage, and three phase electricity. Also, UV excitation may completely ablate sp^2 bonded carbon, making the interpretation of the results a challenge. Nevertheless, the systematic use of this technique will reveal new information on the growth mechanisms and their effect on the obtained DLC thin-films [3].

Chapter 3

Experimental procedures and results

3.1 Overview of experiment

When Raman and Krishnan first published their manuscript in 1928, Raman scattering was introduced as a new type of secondary radiation. During the period of World War II, i.e., 1939-1945, an infra-red spectrometer, allowing for the acquisition of a Raman spectrum, was developed. Since then, the field of Raman spectroscopy has dramatically evolved. Initially, Raman spectroscopy existed as a poor man's alternative to infra-red spectroscopy. This remained to be the case until two notable developments occurred.

The first one came with the advent of the double monochromator, the laser, and electronic means of signal detection; these technologies were intially developed in the 1960s. The second one began more than three decades later with the developments of laser-line blocking filters and scientific grade charge coupled device arrays [3]. It should be mentioned here that the Raman cross-section is directly proportional to the fourth power of the excitation frequency. Hence, the sensitivity of a Raman measurement monotonically increases in response to increases in the excitation frequency. Considering these aspects, along with recent developments in instrumenta-

tion, Raman spectroscopy has become one of the most important vibrational spectroscopic tools. Raman spectrometers can now be used to non-invasively study the relationship between thin-film growth and the underlying material properties, allowing one to gain insight into the wear characteristics of thin-films. The results presented in this thesis are primarily acquired through the use of Raman spectroscopy.

DLC is a term commonly employed to describe hard forms of carbon containing hydrogen, nitrogen, or other elements, in varying proportions. Even though DLC is now widely used, its structure, and the roles that these proportions play in determining its material properties, remain the subject of considerable conjecture [3]. Raman spectroscopy may be used to non-invasively probe the material properties of samples of thin-film carbon, providing insight and clarity into these underlying properties without requiring the expenditure of excessive cost or excessive effort. Raman spectroscopy will be used here in order to probe the properties of thin-films of carbon.

In this chapter, the experimental methodology, employed for the purposes of this analysis, is presented. I first start by describing the manner in which the thin-films of carbon have been prepared; while I only perform measurements on the thin-films of carbon that have been prepared for the purposes of this analysis, it should be noted that both PECVD prepared and magnetron sputtering prepared thin-films of carbon are employed for the purposes of this analysis. Then, the Raman experimental set-up, employed for the purposes of this analysis, is described. Finally, the Raman spectral processing, used for the purposes of this analysis, is detailed.

This chapter is organized in the following manner. In Section 3.2, I describe the process whereby some of the thin-films of carbon, examined

within the scope of this thesis, are prepared using the PECVD deposition approach. Then, in Section 3.3, I describe the process whereby some of the thin-films of carbon, examined within the scope of this thesis, are prepared using the magnetron sputtering approach. In Section 3.4, I then introduce the Raman spectrometer used and identify the settings employed for the purposes of conducting Raman spectroscopy. This is followed, in Section 3.5, with a discussion about the data processing techniques used to process the acquired Raman spectra that are to be used for the purposes of this study.

3.2 PECVD preparation of thin-film carbon

Some of the thin-films of carbon that are considered in this analysis have been prepared using a PECVD approach. The details, concerning the preparation of these PECVD deposited thin-films of carbon, are provided below.

3.2.1 The PECVD deposition system

The FLARION Series Model FLR300C-TT, pictorially represented in Figure 3.1, is a table-top plasma reactor with multi-gas flow control that allows one to deposit thin-films of carbon onto an underlying substrate. This machine was developed by Plasmionique Inc. A picture of the actual set-up is shown in Figure 3.2.

Features of the system include:

i) Chamber: It consists of two vertically connected stainless steel cylinders with overall dimensions of 8 inches in diameter and 20 inches in length. The inner-wall liner on each cylinder protects the chamber from unwanted depositions. There is a view-port of 4 inches in diameter on the top flange

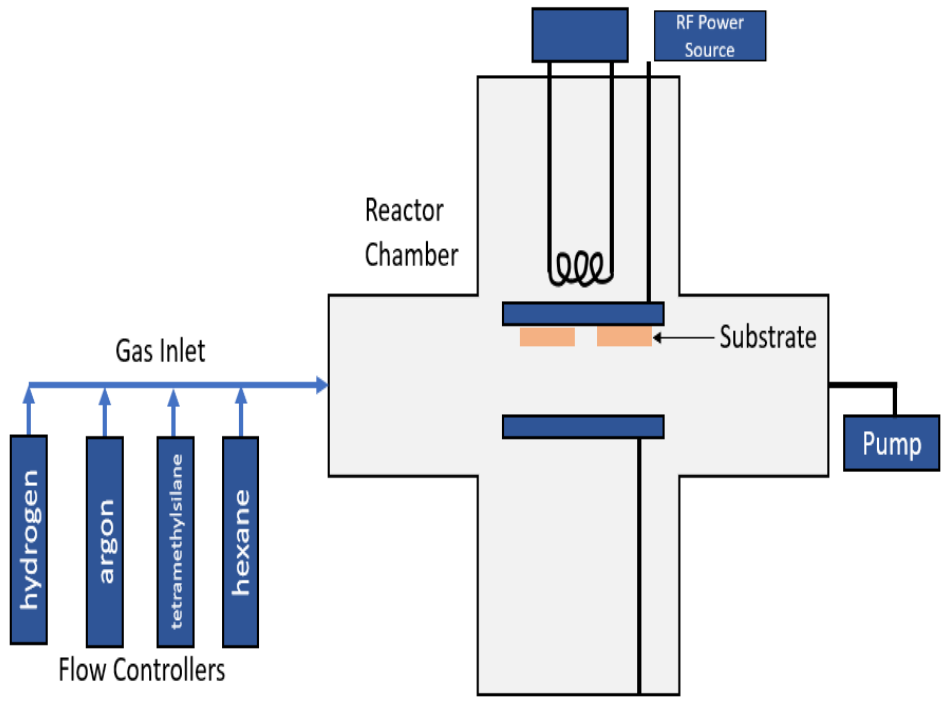

Figure 3.1: A pictorial representation of the components of a PECVD deposition system. Created by Ashraf Ahsan, used by permission. The online version of this figure is depicted in color.

Figure 3.2: The front-view of the PECVD system, developed by Plasmionique Inc., used for the purposes of preparing some of the thin-film carbon samples considered in this analysis. Created by Plasmionique Inc., used by permission. The online version of this figure is depicted in color.

and the structure is connected to the pumping manifold, a feed-through acting as the substrate holder (gas inlet). When no gas flows into the chamber for more than 10 seconds, the rf output gets disabled. A vent gas, such as dry nitrogen or argon, may be fed using this gas inlet in order to bring the chamber up to atmospheric pressure. When power is applied to the reactant gases, the cloud turns purple, indicating the presence of plasma within the chamber.

ii) Vacuum system: It is connected to the chamber and the control system. The vacuum system consists of a convection enhanced Pirani gauge that monitors the vacuum pressure, a mechanical pump with a perfluoropolyether lubricant, and a temperature compensated capacitance pressure guage that measures the process pressure. There is also a fore-line angle valve system that helps with the pumping-out from the chamber.

iii) Substrate mount: It is a platform which enables the creation of a capacitively coupled plasma with fixing points, allowing for the attachment of a structure for hanging substrates; this allows for one to hang the rinsed substrates. It also allows for the uniform flow of gas, from top-to-bottom. It has a water-cooled base without any temperature measurement or control, and allows for the rf biasing of the substrate.

iv) Plasma system: It is connected to the control system and the substrate mount in the chamber overall forming the substrate bias control. The system consists of an rf generator of 300 W at 13.56 MHz, with an automatic impedance matching circuit and an integrated controller. This creates a capacitively coupled plasma on an isolated sample stage by biasing the substrate with rf power.

v) Gas management: The gas distribution system is connected to the control system, chamber, and exhaust in order to avoid over-pressure. This

system is separated from the table-top enclosure in order to provide for expansion and in order to isolate toxic gases. It consists of four-mass flow controllers, for argon, hydrogen, hexane and tetramethylsilane (TMS), respectively, with appropriate correction factors. Each gas line is equipped with a software controlled valve.

vi) Control system: It consists of the input power or power distribution system, mechanical pump, and emergency stop mechanism, with hardware and software safety interlocks. It also includes a control box with programmable logic control for general system control and another programmable logic controller for process gas control. The PLASMICON control software, which comes with this system, is based on Windows along with LABView 2012, thereby providing a graphical user interface for real-time plotting, data logging, and process recipe and parameter display.

3.2.2 PECVD operation and parameters

Now that the overall system has been described, it is possible to move onto the deposition process itself, and sample loading is where it all begins. When moving objects in and out of the chambers, it is advisable to wear the proper gloves. The inner wall liners were checked for material peels and in order to clean the chamber. Samples were loaded either by opening the top flange or the entire chamber section. The mechanical pump was started for 15 minutes prior to deposition and then the fore-line angle valve in the vacuum system was opened slowly. In preparation for any given deposition run, the table-top was turned on with a recommended delay of 10 minutes so as to allow for the mass flow controllers and the Baratron gauge to reach a stable temperature of operation. It was important to make sure that the

rf generator was turned on, appropriate gas bottles being opened in order to allow for the compressed air to reach the system, and so as to ensure that the water cooling was on. The mass-flow controller settings were edited for appropriate gases, and the valves were opened briefly to remove any of the previously accumulated gas before starting a given deposition, this being done in order to avoid abrupt changes. The valves were opened for the gases that were initially used to start the discharge.

For the depositions that were performed for the preparation of the thin-films of carbon used for the purposes of this particular study, the process started with argon followed by other active gases, which is advisable when working at low pressures. The desired flow rate set-points were entered so as to initiate the flow of gases. By applying rf power, the substrate biasing process was initiated. It was noted that a very low DC bias voltage resulted in a soft coating and that a very high value sputtered the material instead of coating it onto the underlying substrate.

Biasing acted as a substrate cleaning process, initially when done in argon. The reflected power was kept close to zero and attention was paid to the plasma discharge process. The rf power was disabled and, at the end of the process, the automatic pressure control mode was stopped before opening the fore-line angle valves. The samples were given some time to cool down before retrieving, while allowing for small amounts of argon to flow into the chamber. The mechanical pump was stopped and the vent valve was opened briefly in order to bring the chamber up to atmospheric pressure.

During the deposition itself, the steps performed were: (1) creating a gas flow, (2) hydrogen cleaning, (3) argon cleaning, (4) TMS layer deposition, (5) DLC layer deposition, and (6) shutting everything off. The Pirani gauge

was used in order to measure the vacuum pressure (in Torr) throughout the deposition process. The Baratron gauge was used in order to examine the overall pressure (in Torr), the argon flow (in sccm), the hydrogen flow (in sccm), the hexane flow (in sccm), and the TMS flow (in sccm). Some of the thin-film carbon samples, used for the purposes of this analysis, were prepared using this approach. The deposition parameters, used for these sample preparations, are tabulated in Tables 3.1, 3.2, and 3.3.

3.3 Sputtering preparation of thin-film carbon

Thin-film carbon samples used for the purposes of this analysis were also prepared through the use of magnetron sputtering. Figure 3.3 provides a pictorial representation of the key components inside such a deposition system. The machine used for the preparation of these thin-films is an rf and dc magnetron sputtering machine, manufactured by Anatech Ltd. more than a decade ago, namely, the Hummer XII. This system can be controlled manually, with analog knobs adjusting the parameters for the deposition of the thin-films. Human interaction, or visual inspection, is required, as the machine will not automatically regulate the process variables to a set-point. It should be noted that the lack of a closed-loop system also introduces inaccuracies while regulating the analog knobs. The top lid of the chamber needs to be opened each time for sample insertion, as a load-lock, or an auxiliary chamber, does not exist. This also causes exposure to oxygen and other contaminants during each run. It can be challenging to maintain all of the process parameters exactly the same during each run.

Generally, the sputtering process can be divided into four stages, which are: (1) the start-up phase, (2) the rf argon plasma cleaning process, (3) the

Table 3.1: Deposition parameters for the PECVD prepared samples, AW128, AW129, and AW130.

Sample	**Step name**	**Duration (min)**	**Power (W)**	**Argon flow (sccm)**	**Hydrogen flow (sccm)**	**Hexane flow (sccm)**	**TMS flow (sccm)**
AW128	Create gas flow	15	0	5	8	0	0
	Hydrogen cleaning	600	250	4	4	0	0
	Argon cleaning	600	250	4	0	0	0
	TMS layer	600	120	8	0	0	5
	DLC layer	1800	200	2	0	4	0
	Shut off everything	17	0	0	0	0	0
AW129	Create gas flow	15	0	5	8	0	0
	Hydrogen cleaning	600	250	4	4	0	0
	Argon cleaning	600	250	4	0	0	0
	TMS layer	600	120	18	0	0	18
	DLC layer	1800	200	18	0	17.9	0
	Shut off everything	17	0	0	0	0	0
AW130	Create gas flow	15	0	5	8	0	0
	Hydrogen cleaning	600	250	4	4	0	0
	Argon cleaning	600	250	4	0	0	0
	TMS layer	600	120	18	0	0	18
	DLC layer	1800	200	18	0	17.9	0
	Shut off everything	17	0	0	0	0	0

Table 3.2: Deposition parameters for the PECVD prepared samples, AW133, AW135, and AW143.

Sample	**Step name**	**Duration (min)**	**Power (W)**	**Argon flow (sccm)**	**Hydrogen flow (sccm)**	**Hexane flow (sccm)**	**TMS flow (sccm)**
AW133	Create gas flow	15	0	5	8	0	0
	Hydrogen cleaning	600	250	4	4	0	0
	Argon cleaning	600	250	4	0	0	0
	TMS layer	600	120	18	0	0	18
	DLC layer	1800	200	18	0	17.9	0
	Shut off everything	17	0	0	0	0	0
AW135	Create gas flow	15	0	5	8	0	0
	Hydrogen cleaning	600	250	4	4	0	0
	Argon cleaning	600	250	4	0	0	0
	TMS layer	600	120	9	0	0	9
	DLC layer	1800	200	9	0	9	0
	Shut off everything	17	0	0	0	0	0
AW143	Create gas flow	15	0	5	8	0	0
	Hydrogen cleaning	600	250	4	4	0	0
	Argon cleaning	600	250	4	0	0	0
	TMS layer	600	100	12	0	0	12
	DLC layer	1800	100	12	0	12	0
	Shut off everything	17	0	0	0	0	0

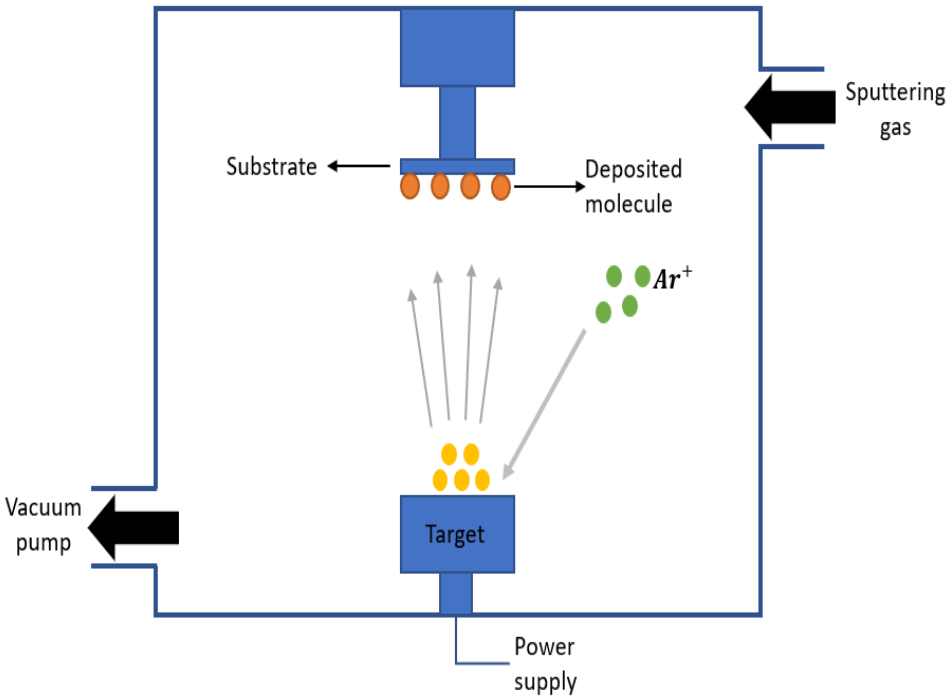

Figure 3.3: A pictorial representation of the components of a sputtering deposition system. Created by Ashraf Ahsan, used by permission. The online version of this figure is depicted in color.

Table 3.3: Deposition parameters for the PECVD prepared sample, AW145.

Sample	**Step name**	**Duration (min)**	**Power (W)**	**Argon flow (sccm)**	**Hydrogen flow (sccm)**	**Hexane flow (sccm)**	**TMS flow (sccm)**
AW145	Create gas flow	15	0	5	8	0	0
	Hydrogen cleaning	600	250	4	4	0	0
	Argon cleaning	600	250	4	0	0	0
	TMS layer	600	120	18	0	0	18
	DLC layer	1800	150	18	0	17.9	0
	Shut off everything	17	0	0	0	0	0

sputtering stage, and (4) the shut-down sequence. The samples in use had to be mechanically polished with a bung machine initially. This is done so as to ensure a shiny and smooth surface, which directly relates to the glossiness of the resultant carbon thin-films. Two types of ultrasonic baths came into action here, where the first mixture is hot water with all purpose cleaner for about 20 minutes so as to get rid of the dirt accumulated while polishing. The latter contains pure acetone so as to remove residual organic components, if any. In order to allow the substrates to dry in a streak-free way, the samples are then swung on a cord. Overall, these steps ensure that the samples are not touched by human hands during and following the cleaning process.

As depicted in Figure 3.4, the vacuum chamber consists of an rf plate, which can be covered with a shutter, a target with a shutter in front, a rotational ring holder, a temperature gauge, and a heater. The substrates are then kept in this vacuum chamber by applying a vacuum pressure of 1.3×10^{-4} Torr so as to reduce the amount of oxygen. It is not possible

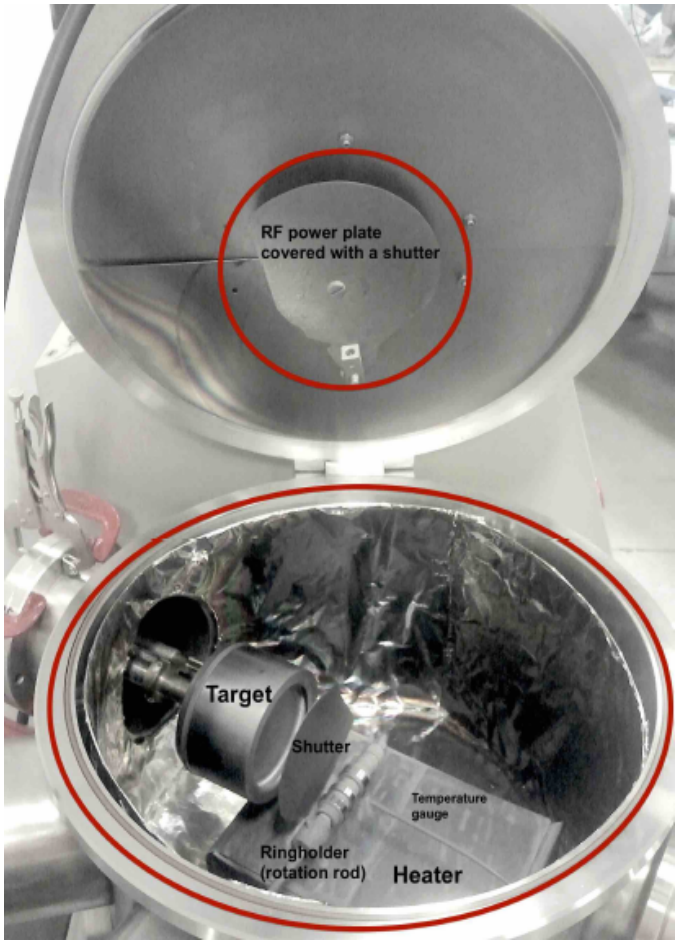

Figure 3.4: The basic components inside of the sputtering apparatus. This image is from Laumer [44], used by permission. The online version of this figure is depicted in color.

to entirely remove contamination, hence, an argon based plasma cleaning process is carried out in order to clean the substrate of oxygen on a molecular level. The chamber is then filled with an argon gas flow of around 75 sccm, which is ionized with an rf power of 200 W at 13.56 MHz. Argon ions bombard the surface to remove foreign molecules without any chemical reaction. The surface becomes rough after this bombardment, and this improves the adhesion. After this rf cleaning process for about 85 minutes, a water drop can slide perfectly down the surface without sticking, unlike the uncleaned surfaces. The process begins with the polishing and the cleaning of the substrates followed by ultrasonic cleaning.

After pumping down the chamber, an rf cleaning process is carried out. The rf cleaning is suspended to start pre-sputtering in the system. The gun shutter is opened when the pre-sputtering ends. It is then time to stop the sputtering and switch-off the turbo pump followed by the cool-down process. All switches are turned-off before opening the chamber. As described in this section, the samples were placed inside the chamber after cleaning the substrate. The power and gas supplies were then turned-on, followed by the pumping down to a vacuum level of about 1.3×10^{-4} Torr. The rf argon plasma process was then started and when the surface has been cleaned, the samples were then allowed to cool down. The sputtering process was then initiated by allowing an argon gas flow of 12.5 sccm with a deposition pressure of 1 mTorr. Eventually, a proper shut-down sequence was carried out followed by the venting of the chamber in order to complete the coating process. During this whole process, the parameters that can be manually controlled are the choice of using a dc power excitation at 200 W or an rf power excitation at 200 W, the gas flow rates, the deposition times, the temperature of the substrate, and the distance between the sputtering gun to

the substrate. Each sample is labeled according to the experimental number for the deposition run used for the preparation of the carbon thin-films. The samples that were prepared for the purposes of this study, using the above mentioned method, and their corresponding deposition parameters, are provided in Table 3.4.

3.4 Raman spectroscopy

3.4.1 Machine and parameters

The Raman spectra reported in this thesis have all been acquired using the LabRAM HR Raman Confocal Microscope, this apparatus being shown in Figures 3.5 and 3.6, which has both helium-cadmium and helium-neon lasers, both manufactured by Horiba Scientific. This machine supports excitation using source wavelengths which are set to 325.000 (HeCd laser with power output of 2 - 50 mW), 441.557 (HeCd laser with power output of 14 - 180 mW), and 632.817 nm (He-Ne laser with power output of 17 mW). Two calibrations are needed for the purposes of these measurements. The first one involves a calibration of the spectral axis and the second one requires the user to run a standard crystalline silicon sample to make sure that the peak is located exactly at 520.7 cm^{-1}, as shown in Figures 3.7 and 3.8.

To acquire a given Raman spectrum, it is necessary to check the switch box power indicator, which should be on at all times, and can be found on the backside of the box, as seen in Figure 3.6. The laser must be turned-on using the laser keys, which remains inside the keyhole during the operation. It takes a minute for the current to ramp up to 0.8×100 mA, during which the light inside the laser tube can be seen and the fan starts to run. The red indicator should stay on and within two minutes the system should produce

Table 3.4: Deposition parameters for the sputtered samples.

Steps	**Samples**		
	MS115	**MS213**	**MS217**
Sputtering target materials	Carbon	Carbon	Carbon
Gun-substrate distance (mm)	60	50	50
Power (W)	rf 200	rf 200	dc 200
Gas flow during sputtering (sccm)	12.5	12.5	12.5
Duration of pumping gas out (min)	62	75	86
RF cleaning duration (min)	30	30	30
Pre-sputtering duration (min)	5	5	5
Pre-sputtering temperature (°C)	30	32	17
Sputtering duration (min)	120	120	120
Sputtering temperature (°C)	76	72	70

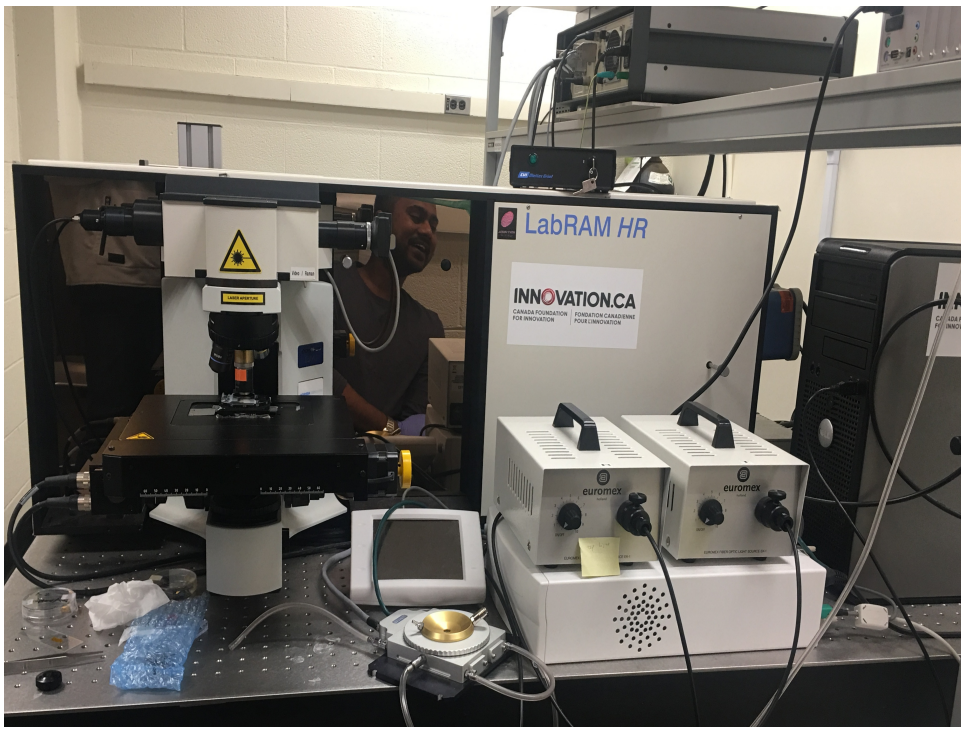

Figure 3.5: The front view of the LabRAM HR Raman confocal microscope that was manufactured by Horiba Scientific. This image is captured by Ashraf Ahsan, used by permission. The online version of this figure is depicted in color.

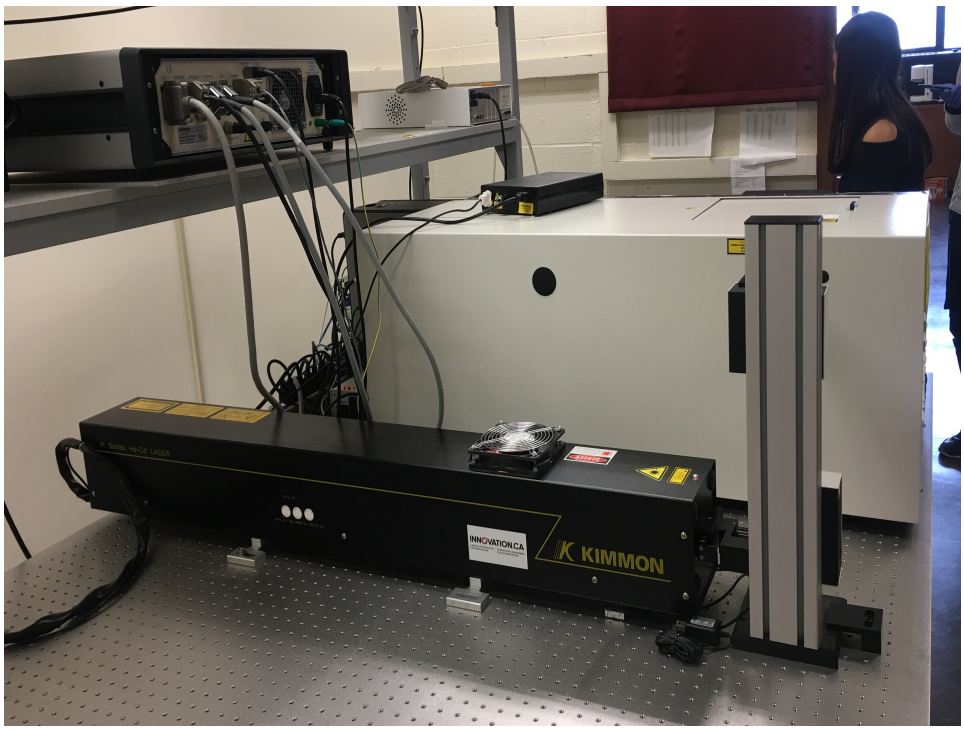

Figure 3.6: The back-view of the LabRAM HR Raman confocal microscope by Horiba Scientific. This image is captured by Ashraf Ahsan, used by permission. The online version of this figure is depicted in color.

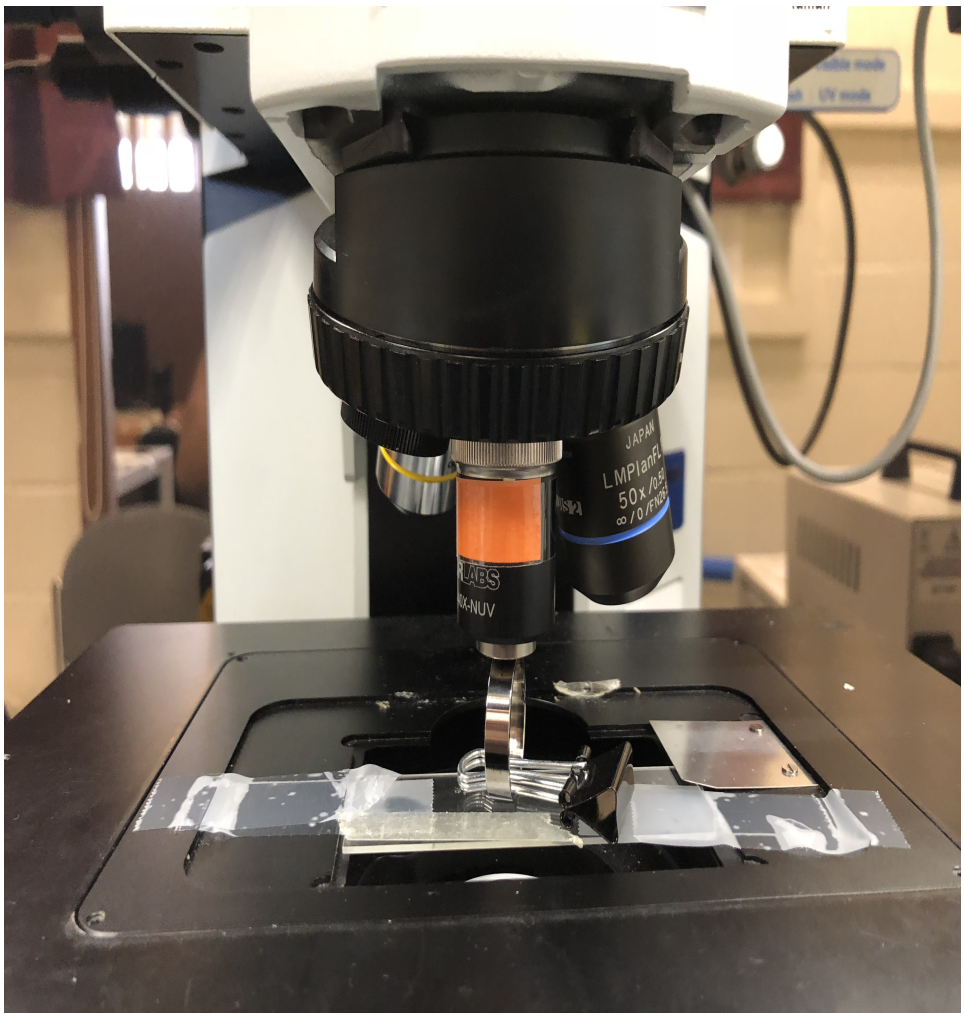

Figure 3.7: The sample placement for Raman spectroscopy. This image is captured by Ashraf Ahsan, used by permission. The online version of this figure is depicted in color.

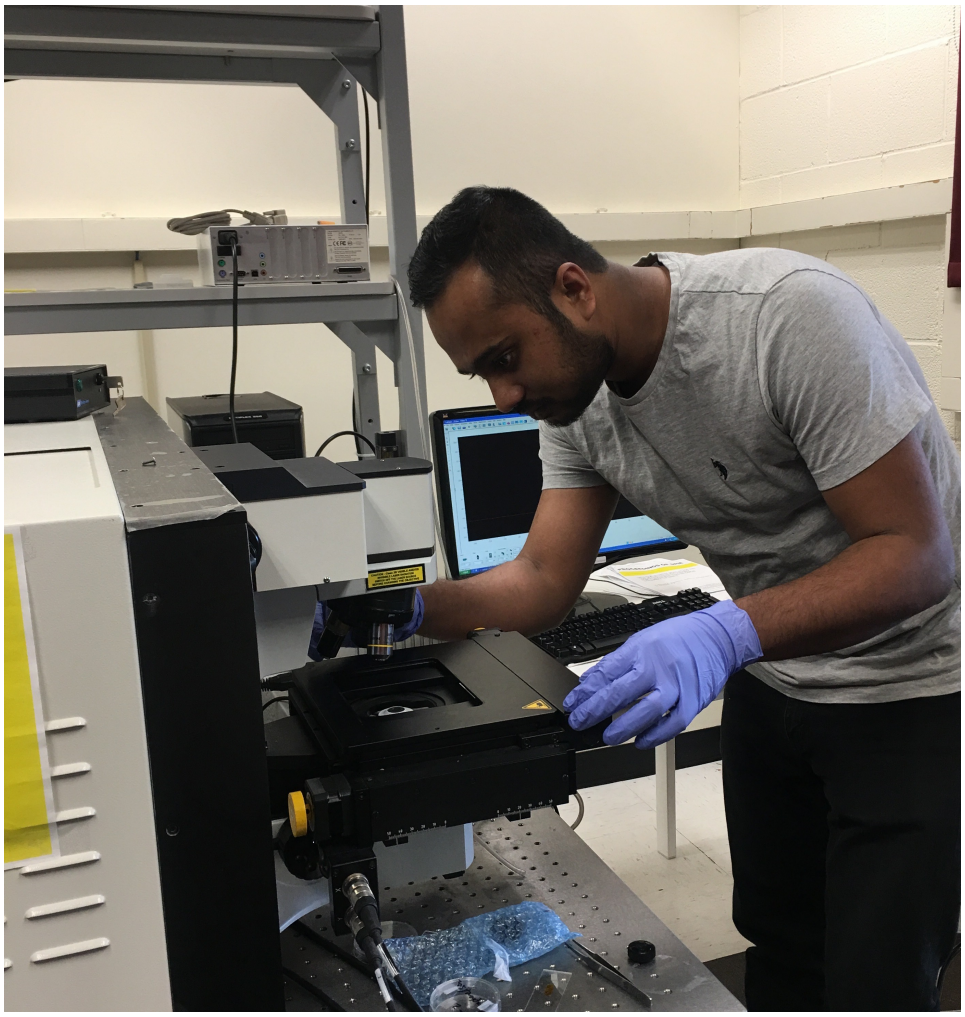

Figure 3.8: This image shows the sample placement and the working position for the LabRAM HR Raman confocal microscope by Horiba Scientific. The author is presented in this image, captured by permission. The online version of this figure is depicted in color.

laser light. An indicator bar can be pushed or pulled to get the desired UV or visible Raman measurement, respectively. Meanwhile, the computer and the monitor attached to it should be turned on to open LabSpec 5. It is advised to check the height of the optical lenses before mounting the sample in order to avoid scratches on both surfaces. The lens can be raised by turning the knob towards the user. The top light, which is also known as the reflection light, needs to be turned-on. It is possible to switch to camera mode and a microscopic image can be seen by clicking on the Video icon on the LabSpec 5 tool-bar.

As the laser might be too strong at times, it is required to use a density filter in order to lower the laser light intensity and to see the surface features under white light illumination. The density filter numbers represent the optical density OD = log (power transmission factor), where 0 refers to the absence of a density filter, D 1 refers to 10 %, D 0.6 refers to 25 %, D 0.3 refers to 50 % transparency, respectively. After completing the experiment, the lens must be raised to unload the sample. The laser must be turned-off and the data must be saved before turning off the computer. The parameters which can play a key role in Raman spectroscopic results are the excitation source wavelength, the magnification of the lens, the observation time, the number of cycles for the experiment, the filter size, the spot size, the grating, the numerical aperture, the applied power, the spectral resolution, and the Raman-shift range. Table 3.5 gives the list of the parameters to be considered when acquiring a given Raman spectrum.

Table 3.5: Parameters for the Raman analysis on the samples.

Deposition type	Sample	Wavelength (nm)	Filter	Cycle	Time (sec)	Magnification	Hole	Grating
PECVD	AW128	325	0	1	150	40	250	2400
		442	D 0.3	3	20	50	250	2400
		633	-	3	20	100	-	1800
	AW129	325	0	1	150	40	250	2400
		442	D 0.6	3	20	50	250	2400
		633	-	3	20	100	-	1800
	AW130	325	0	1	200	40	250	2400
		442	D 0.6	3	20	50	250	2400
		633	-	3	20	100	-	1800
	AW133	325	0	1	100	40	250	2400
		442	D 0.6	3	20	50	250	2400
		633	-	3	20	100	-	1800
	AW135	325	0	1	200	40	250	2400
		442	D 0.6	3	20	50	250	2400
		633	-	3	20	100	-	1800
	AW143	325	0	1	150	40	250	2400
		442	D 1	3	20	50	250	2400
		633	-	3	60	100	-	1800
	AW145	325	0	1	200	40	250	2400
		442	D 1	3	20	50	250	2400
		633	-	3	20	100	-	1800
PVD	MS115	325	D 0.3	3	200	40	250	2400
		442	D 0.6	3	20	50	250	2400
		633	-	2	20	20	-	1800
	MS213	325	0	1	150	40	250	2400
		442	D 1	3	20	50	250	2400
		633	-	3	20	20	-	1800
	MS217	325	0	1	200	40	250	2400
		442	D 1	3	20	50	250	2400
		633	-	3	20	20	-	1800

3.5 Data processing

3.5.1 Baseline correction

Experimental measurements are susceptible to noise and Raman measurements are also affected by the presence of a baseline[1]. Researchers in the field have adapted a common practice in order to compensate for the presence of this baseline, known as baseline correction. Baseline correction is performed before any further spectral analysis. The process of baseline correction is described below.

The baseline observed in the spectral response of any experimental measurement is corrected by subtracting the so-called baseline from the unprocessed data. The Raman spectra of all of the samples considered in this analysis have been measured from 800 to 2000 cm^{-1}. It is observed that selecting the baseline, spanning from 1000 to 1800 cm^{-1}, yielded satisfactory baseline correction. This range was suggested by Zhao *et al.* [82]. For the purposes of this research, a simplified process of baseline correction, which includes the drawing of a straight line from around 1000 cm^{-1} to about 1800 cm^{-1}, as suggested by Zhao *et al.* [82], was employed in order to subtract the baseline from the unprocessed Raman spectra. Different researchers have used their own approach to this problem, but the essence remains the same, and the data is baseline corrected by removing the baseline caused by the noise present from the unprocessed data.

[1]The baseline arises from dust in the air, electronic noise, imperfections in the optics, the presence of the underlying substrate, and a variety of other factors.

3.5.2 Peak fitting

The general consensus in the field of Raman spectroscopy related to carbon thin-films is that the sp^2 and sp^3 bond contents are roughly proportional to the integrated area or the amplitude of their corresponding peaks. The integrated intensity ratio of the D- ($\sim$ 1350 cm^{-1}) and G-peaks ($\sim$ 1580 cm^{-1}) provide insights into the sp^2 to sp^3 bonding ratio within carbon thin-films. If it is accepted that sp^2 bonds lead to the appearance of the G-peak and that sp^3 bonds lead to the presence of D-peak, then the overall baseline corrected data must be the sum of both these peaks. Consequently, peak fitting provides a means of identifying the fraction of sp^2 and sp^3 bonding.

A variety of peak fitting profiles are available and the nature of the observed peaks governs one's choice of peak profile selection. Based on the amount of noise in the Raman spectra of thin-films of carbon, the peaks are often assumed to be Gaussian functions, i.e., the form of each peak is of the form

$$Ae^{-(x-m)^2/2\sigma^2}, \tag{3.1}$$

where A denotes the amplitude of the peak, m refers to the peak location, and σ provides a measure of the peak breadth. Therefore, I fit the acquired Raman spectral data to the sum over two Gaussian peak, i.e.,

$$A_D e^{-(x-m_D)^2/2\sigma^2} + A_G e^{-(x-m_G)^2/2\sigma^2}, \tag{3.2}$$

to the baseline corrected Raman spectra, where the peak amplitudes of the D- and G-peaks are denoted as A_D and A_G, respectively, the peak locations are represented by m_D and m_G, and their breadths are represented by σ_D

and σ_G.

Assuming that the baseline corrected data corresponds to the sum over two selected Gaussian fitted peaks, as seen in Eq. (3.2), the analysis is performed within the framework of the least-squares-error analysis, i.e., it aims to minimize the difference between the baseline corrected data and the sum over the two peaks through the selection of the fitting parameters, i.e., A_D, A_G, m_D, m_G, σ_D, and σ_G, so as to minimize this error.

Several researchers assert that peak magnitudes should be considered to study thin-film bonds, whereas others believe that the peak integration, or the area underlying the peaks, instead should be focused upon. For the purposes of this thesis, both approaches are considered. In particular, the integrated intensities, I_D/I_G, as well as the peak amplitudes, A_D/A_G, are considered; where

$$I_D = \int_{\sim 1000\, cm^{-1}}^{\sim 1800\, cm^{-1}} [Ae^{-(x-m_D)^2/2\sigma_D^2}]\, dx, \tag{3.3}$$

for the D-peak, and

$$I_G = \int_{\sim 1000\, cm^{-1}}^{\sim 1800\, cm^{-1}} [Ae^{-(x-m_G)^2/2\sigma_G^2}]\, dx, \tag{3.4}$$

for the G-peak.

In this thesis, I aim to determine if there is a relationship between A_D/A_G and I_D/I_G and, if such a relationship exists, if it is related to the source wavelength.

Chapter 4

Analysis

4.1 Overview

Thin-films of carbon are presently being used for military, decorative, and industrial applications [25, 46, 57]. The deposition conditions used for the preparation of these thin-films of carbon have been shown to play a critical role in determining the properties of the resultant materials. Depending on the particular application at hand, the right deposition technique should be employed. If hardness is a priority, for example, it is essential to deposit hydrogen-free forms of thin-film carbon [57]. In the case of wear-and-tear resistant applications of thin-film carbon, however, CVD processes, which mostly lead to hydrogenated forms of thin-film carbon, offer better performance [83].

Raman spectroscopy is often used in studies of thin-film carbon. In Raman spectroscopy, an incident beam of light interacts with the vibrating molecules of the sample under investigation. A certain fraction of these interactions will engage in inelastic interactions, the energy of the photons within the emitted light being less than or greater than those in the incident light. This increase or decrease in the energy of the photons within the re-emitted light (as compared with the incident light) leads to a shift in the corresponding wavelength. It is this shift in the wavelength of the light that

is measured in a determination of a given Raman spectrum.

The form of the Raman spectrum is determined by a variety of factors. The dependence of the Raman spectra on the source wavelength, while widely recognized, has yet to receive much attention in the thin-film carbon scientific literature. This is regrettable, as materials, such as thin-film carbon, are known to exhibit very different responses based on the source wavelength. In this analysis, I aim to quantitatively examine this dependence. Hopefully, through such a study, a greater understanding of the Raman response of thin-film carbon will be developed.

In this chapter, I aim to quantitatively examine how the spectral form of the Raman response of samples of thin-film carbon vary in response to changes in the source wavelength. In order to do this, the Raman spectra, associated with a wide variety of thin-film carbon samples, are considered. The particular focus of this analysis will be on the relationship between the D- and G-peak amplitude ratio and the corresponding integrated intensity ratio, with a critical examination as to whether or not such a relationship exists. The dependence of this relationship on the source wavelength will also be examined.

This chapter is organized in the following manner. The expected variations in the Raman responses are discussed in Section 4.2. Then, in Section 4.3, a brief description of the examined samples is given. In Section 4.4, the procedure employed in order to perform a Raman analysis is then presented. Then, the unprocessed Raman spectra, baseline identification, and the peak fitting process followed by their interpretation, is discussed in Sections 4.5, 4.6, and 4.7, respectively, for the representative samples, AW128 and MS115. Finally, a summary of the acquired Raman results is presented in Section 4.8.

4.2 Variations in the Raman response

The source wavelength plays a critical role in determining the form of the Raman spectral response. First, the interactions that occur with the various peaks that are present within thin-film carbon are critically dependent upon the source wavelength, the cross-section associated with each peak being a function of the source wavelength and the peak location, i.e., certain peaks may be more enhanced than others. Second, the transmission of the optical signals through a given material attenuate, and this rate of attenuation depends upon the source wavelength. In Figure 4.1, the spectral dependence of the optical absorption coefficient, associated with a representative sample of thin-film carbon, is depicted. The result suggests that the Raman response associated with the larger source wavelength will be able to probe deeper regions of thin-film carbon while the Raman response associated with a smaller source wavelength will only be able to probe the surface regions of thin-film carbon[2]. Thus, different source wavelengths probe different regions of thin-film carbon.

In order to set the stage for the type of study that will be conducted, the case of thin-film silicon is introduced. In Figures 4.2 and 4.3, I depict Raman spectra corresponding to a layer of hydrogenated nano-crystalline silicon (nc-Si:H), prepared using a modified very-high-frequency glow-discharge technique. In Figure 4.2, the Raman spectral response of the nc-Si:H sample corresponding to a 532 nm source light is depicted, this light only probing

[2]Based on the spectral dependence of the optical absorption coefficient depicted in Figure 4.1, it is estimated that the penetration depths corresponding to a light source at 325, 442, and 633 nm are about 100, 1000, and 5000 nm, respectively. Given that our thin-films of carbon are about 5 μm in thickness, this suggests that the different Raman sources are probing different regions of the thin-film. Thus, variations in the corresponding Raman spectra are to be expected.

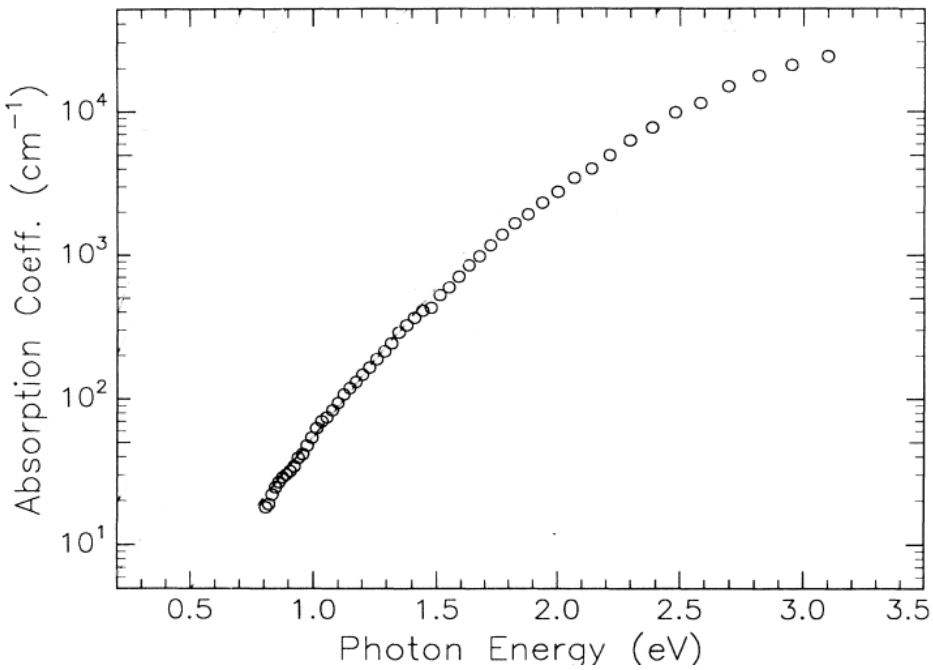

Figure 4.1: A representative optical absorption spectrum associated with thin-film carbon [84]. Digitized by Ashraf Ahsan, used by permission. The online version of this figure is depicted in color.

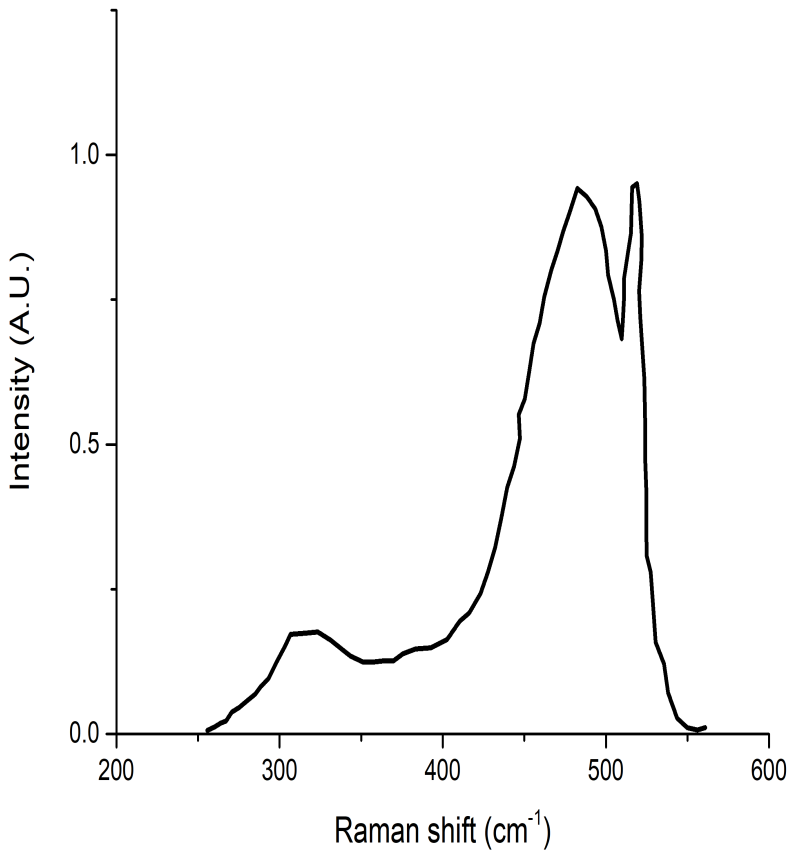

Figure 4.2: The Raman spectrum of a nc-Si:H sample excited using a 532 nm source wavelength [85]. Digitized by Ashraf Ahsan, used by permission.

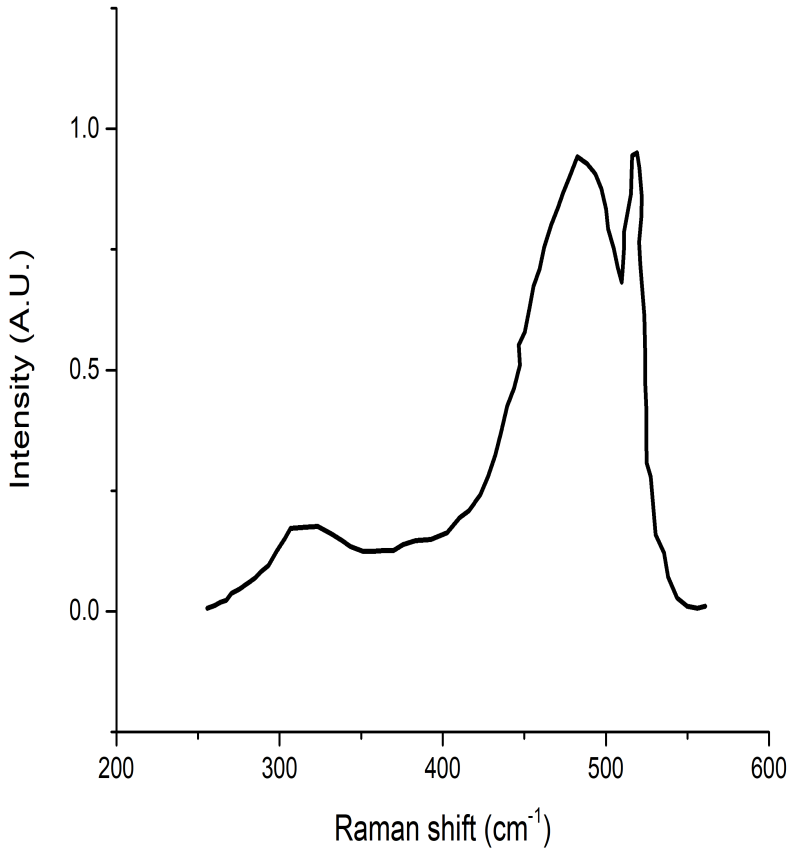

Figure 4.3: The Raman spectrum of a nc-Si:H sample excited using a 632.8 nm source wavelength [85]. This spectrum corresponds to the same sample of thin-film silicon as that depicted in Figure 4.2. Digitized by Ashraf Ahsan, used by permission.

the top layer of the nc-Si:H. A probing of the sample using a 633 nm source light yields a very different Raman spectral response, as is seen in Figure 4.3. This source light instead probes the bulk of the thin-film silicon layer. So, large differences in the Raman spectral response are found for the case of nc-Si:H using different source wavelength, these being observed by contrasting Figure 4.2 with Figure 4.3. It is expected that a similar variation will occur for the case of thin-film carbon.

Clearly, variations in the Raman spectral response of a given sample of thin-film carbon, subjected to different source wavelengths, are to be expected. Variations in the spectral dependence of the Raman spectrum of a given sample in response to changes in the source wavelength arise from variations in the cross-sections that occur and variations in the optical absorption coefficient. The thin-films of carbon exhibit a large spectral variation in the dependence of the optical assumption coefficient, and this dependence is expected to have implications in terms of the form of its Raman spectra. In particular, large source wavelengths, corresponding to lower photon energies, are able to penetrate deeper into a given sample, and thus, probe different regions of a given thin-film. The goal of this analysis is to examine Raman spectra corresponding to thin-film carbon samples using a variety of source wavelengths and to determine how this impacts upon the relationship between A_D/A_G and I_D/I_G, if such a relationship exists at all.

4.3 Description of the examined samples

A large number of thin-film carbon samples were available for this study, these samples being prepared by Mr. Jonathan Laumer. Some of the thin-film carbon samples were prepared through the use of PECVD, others being

fabricated through magnetron sputtering. The Raman spectra, corresponding to each thin-film carbon sample that was examined for the purposes of this analysis, was determined by me. For each sample considered, these Raman spectral measurements were performed, one for each available source wavelength. Variations in the form of the Raman spectra are observed amongst the form of the corresponding thin-film carbon Raman spectra acquired for the purposes of this analysis.

In order to make the analysis manageable, I selected samples of thin-film carbon that corresponded to the most easily interpretable Raman responses. In particular, seven PECVD prepared samples and three magnetron sputtering prepared samples of thin-film carbon are chosen for the purposes of this analysis, pictures of these samples being shown in Figures 4.4 and 4.5.

All samples of thin-film carbon had been deposited onto titanium rings. The Raman spectrum associated with each sample is determined using the three different available source wavelengths, i.e, 325, 442, and 633 nm, the two later wavelengths being commonly found in the scientific literature. All of the measurements are taken by projecting the Raman source beam onto the middle of the sample. This was done in order to avoid the influence of boundary effects that might be expected at the periphery of the thin-film carbon coatings.

Thin-film carbon samples selected for the purposes of this analysis were chosen for the clarity of their Raman response. It should be noted, however, that some of the samples considered possessed Raman spectra that were challenging to baseline correct. Most of these samples had a baseline with a large slope. A picture of such a sample, and the corresponding Raman spectral response, are depicted in Figures 4.6 and 4.7, respectively. This large baseline slope is believed to be related to its high hydrogen content,

(a) AW128.

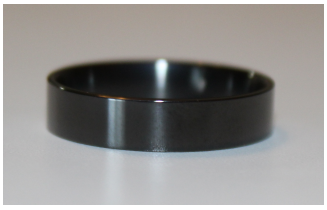

(b) AW129.

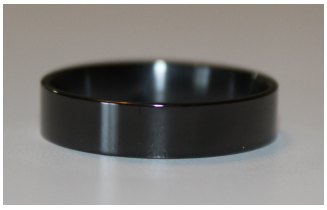

(c) AW130.

(d) AW133.

(e) AW135.

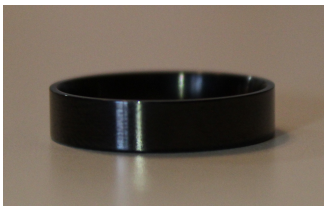

(f) AW143.

(g) AW145.

Figure 4.4: The seven PECVD prepared samples analyzed for the purposes of this work. Sample AW128 is the reference sample. These figures being captured by Ashraf Ahsan, used by permission. The online version of these figures is depicted in color.

(a) MS115.

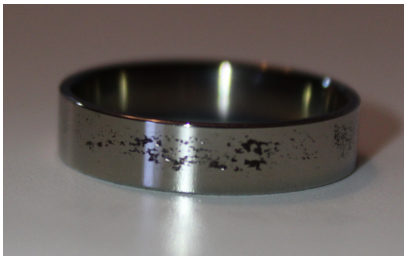

(b) MS213.

(c) MS217.

Figure 4.5: The three magnetron sputtering prepared samples analyzed for the purposes of this work. Sample MS115 is the reference sample. These figures being captured by Ashraf Ahsan, used by permission. The online version of these figures is depicted in color.

as was suggested by Baby *et al.* [86].

For the purposes of this analysis, representative Raman spectra, corresponding to the reference samples that had been produced through PECVD and rf magnetron sputtering depositions, i.e., samples AW128 and MS115, respectively, are presented in this analysis. One of the reasons is to keep the analysis concise. The other reason is that these two samples show consistent behaviour for all of the source wavelengths considered in this analysis and represent trends noted for the other samples deposited using the same techniques.

4.4 Step-by-step guide to Raman data processing

The Raman spectra, obtained through the use of different excitation source wavelengths, corresponding to the thin-films of carbon considered in this analysis, have all been acquired using a LabRAM HR system. This machine is equipped with an internal helium-neon laser, along with two individual helium-cadmium lasers which have been mounted on an extended chassis at the back of the system, this machine being manufactured by Horiba Scientific. The excitation source wavelengths considered are 325, 442, and 633 nm. The spectral data have all been acquired from 800 to 2000 cm^{-1}. I selected baselines that nominally span from about 1000 to around 1800 cm^{-1} and I found that I was able to obtain reasonably satisfactory baseline correction as a result. Typically, for the determination of the baseline, a line is drawn over the spectral range considered and then this baseline is removed from the uncorrected spectral data in order to perform baseline correction.

Once the Raman spectra have been acquired and baseline correction has been performed, peak decompositions are pursued. In particular, I fit all of

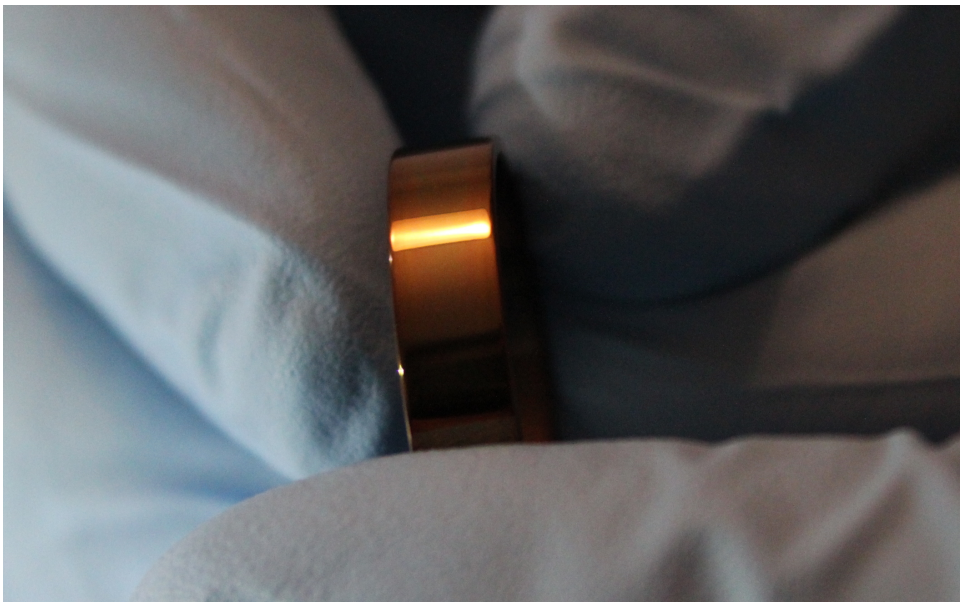

Figure 4.6: A picture of sample AW147. This is a picture of a representative thin-film carbon sample with a high baseline slope. This figure being captured by Ashraf Ahsan, used by permission. The online version of this figure is depicted in color.

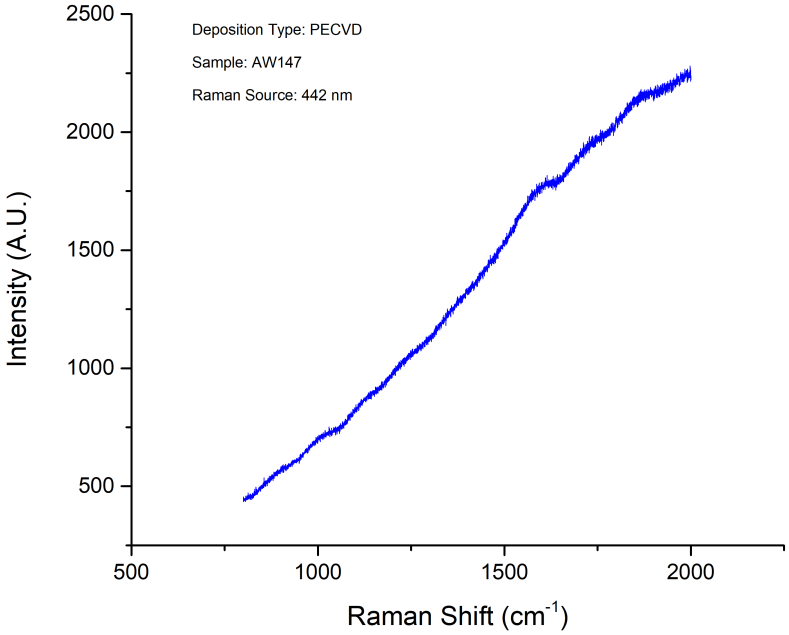

Figure 4.7: The unprocessed Raman spectral data associated with sample AW147 for the source wavelength set to 442 nm. Created by Ashraf Ahsan, used by permission. The online version of this figure is depicted in color.

the acquired Raman spectral data with a sum over two peaks, one representing the D-peak, the other representing the G-peak. For the purposes of this particular analysis, it will be assumed that the two observed peaks are Gaussian functions, although it should be noted that other peak functional forms could also be selected. From this peak fitted data, a number of parameters are acquired corresponding to the individual peaks, such as the peak amplitude, the peak integrated intensity, the mean positions of both the D- and G-peaks, the ratio of the peak amplitudes, i.e., A_D/A_G, and the ratio of peak integrated intensities, i.e., I_D/I_G, respectively, being determined for each thin-film carbon sample considered in this analysis.

4.5 Unprocessed Raman spectral data

The unprocessed Raman spectra, corresponding to the PECVD prepared reference sample, AW128, are depicted in Figures 4.8, 4.9, and 4.10, these spectra being determined using the 325, 442, and 633 nm Raman sources, respectively.

The spectral data between 1000 and 2000 cm^{-1} are plotted, as this is the region over which the important peaks required for this analysis are evident. The D- and G-peaks, at around 1350 and 1580 cm^{-1}, respectively, are distinctly noted in Figures 4.8, 4.9, and 4.10. As suggested by Zhao *et al.* [82], these peaks represent the presence of sp^2 and sp^3 carbon bonding, respectively. Two distinct peaks can be clearly observed when the sample under consideration, AW128, is probed using the 325 nm source wavelength. It is observed that when probed using the 442 nm source wavelength, however, that the Raman spectrum exhibits a larger D-peak. This trend continues with the 633 nm source wavelength, a much larger D-peak being observed

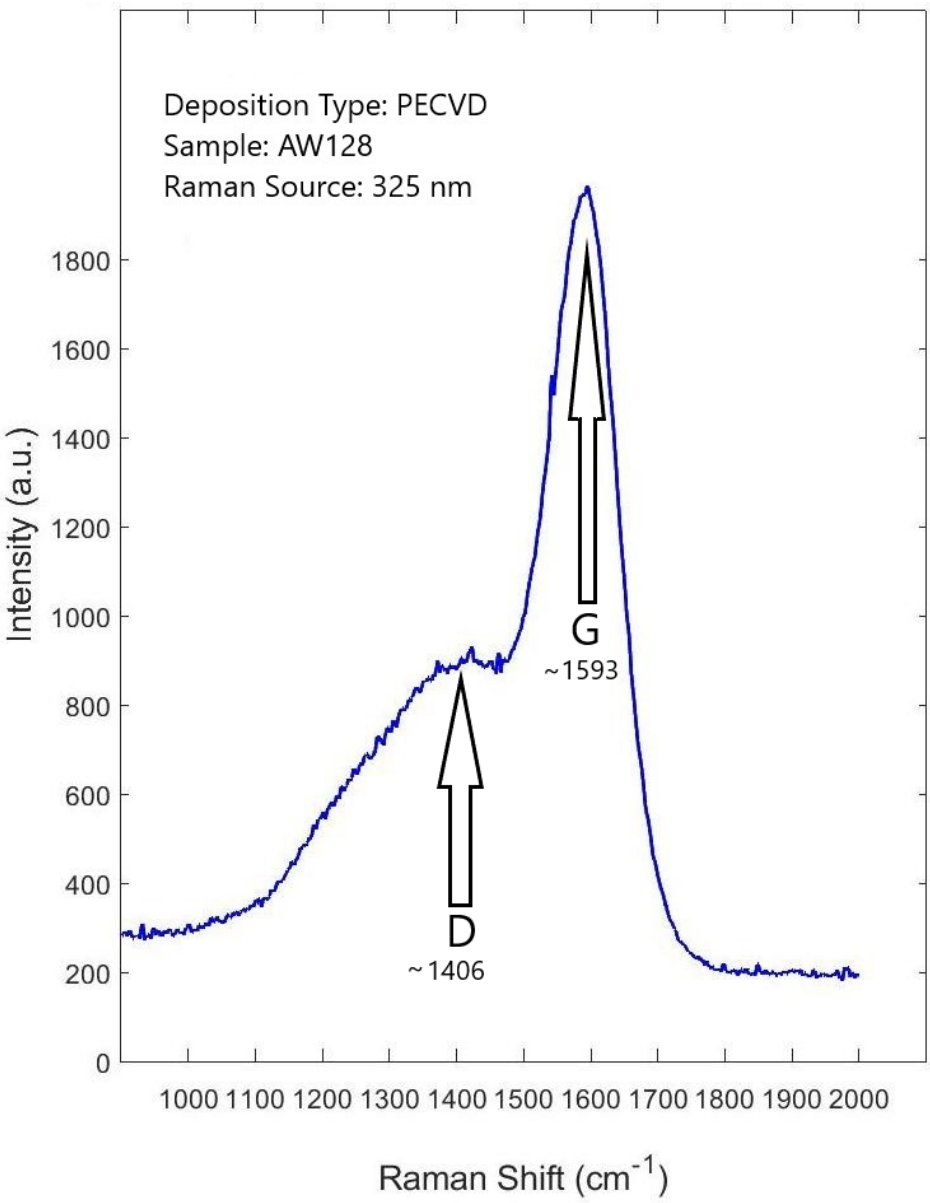

Figure 4.8: The unprocessed Raman spectral data associated with sample AW128 for the source wavelength set to 325 nm. The locations of D-peak and G-peak are indicated with the arrows. Created by Ashraf Ahsan, used by permission. The online version of this figure is depicted in color.

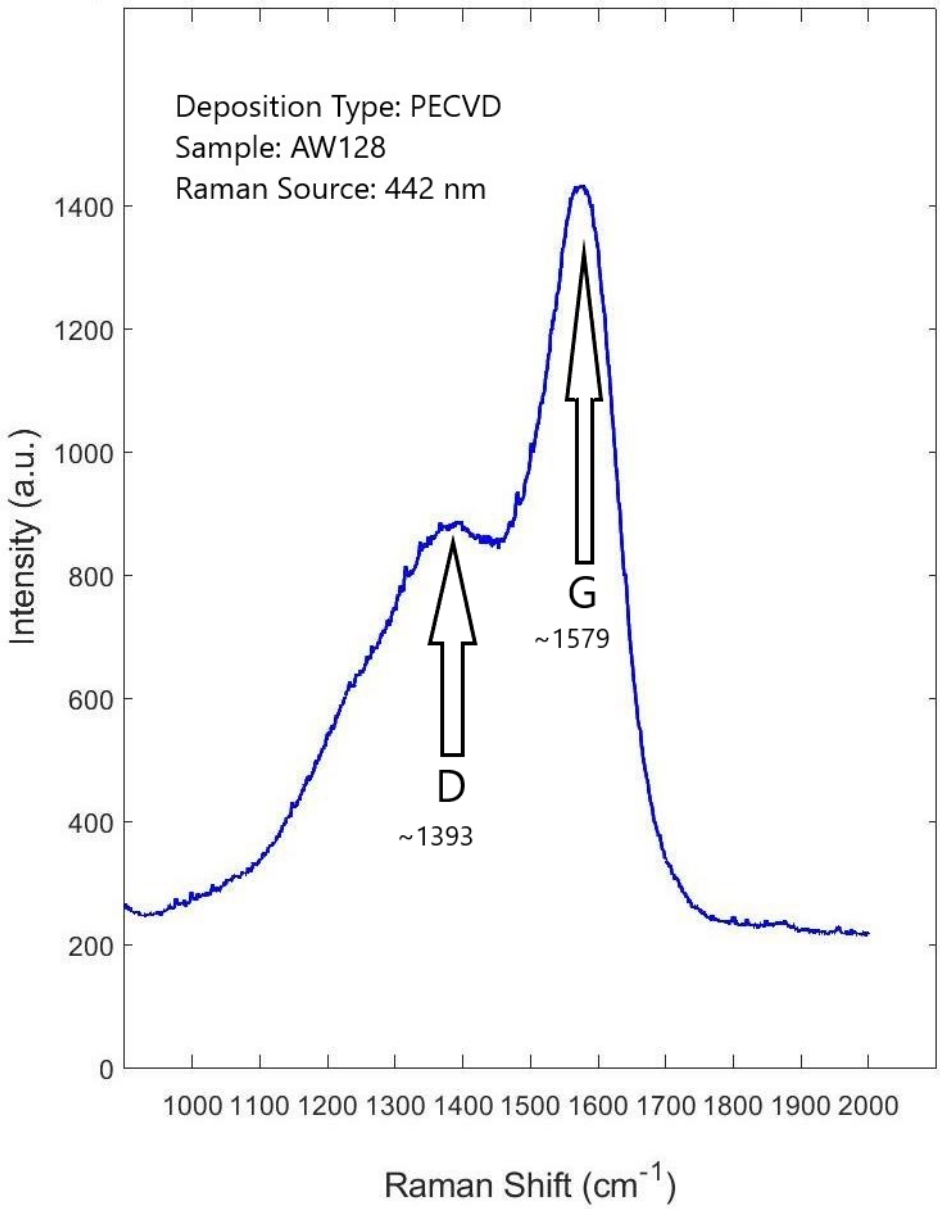

Figure 4.9: The unprocessed Raman spectral data associated with sample AW128 for the source wavelength set to 442 nm. The locations of D-peak and G-peak are indicated with the arrows. Created by Ashraf Ahsan, used by permission. The online version of this figure is depicted in color.

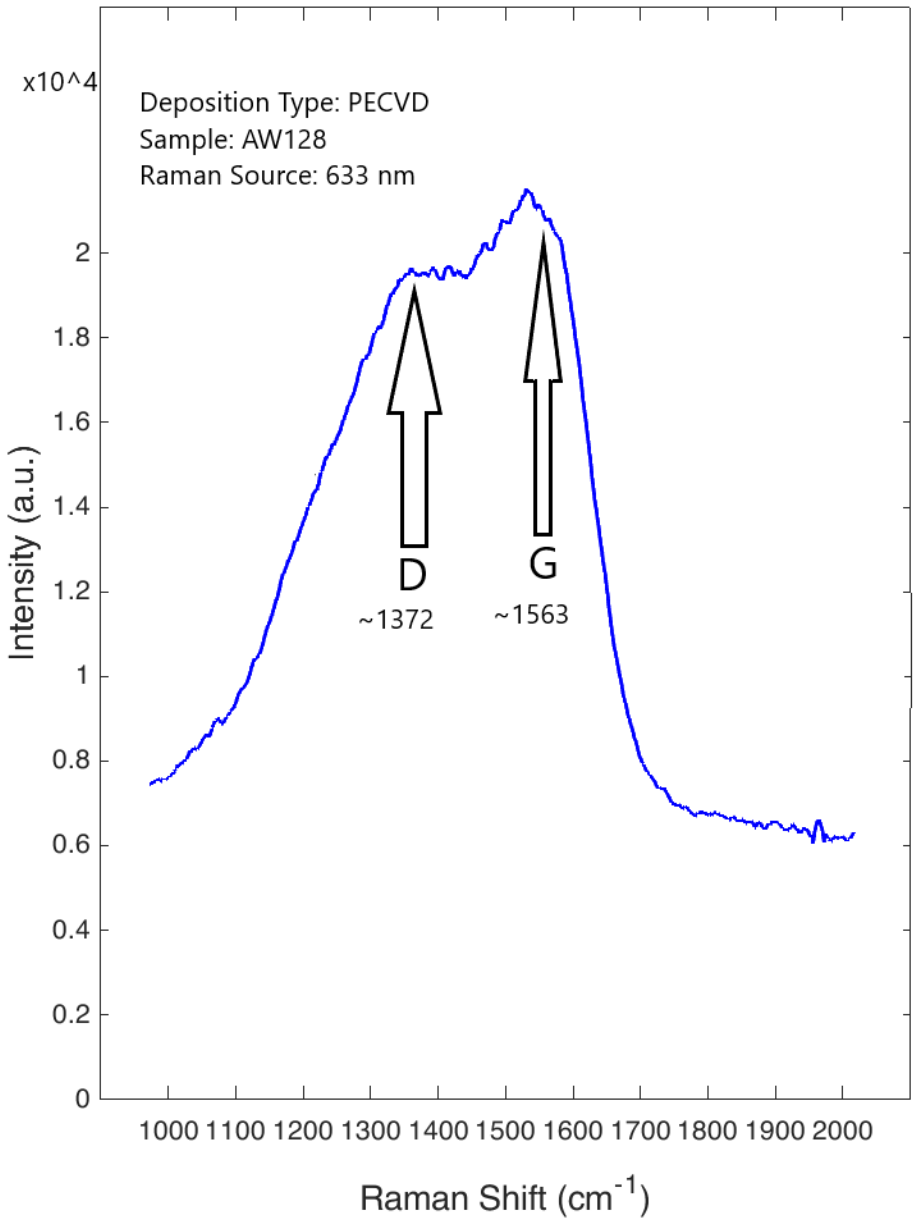

Figure 4.10: The unprocessed Raman spectral data associated with sample AW128 for the source wavelength set to 633 nm. The locations of D-peak and G-peak are indicated with the arrows. Created by Ashraf Ahsan, used by permission. The online version of this figure is depicted in color.

for this case, i.e., it almost merges with the G-peak for this particular case, making it challenging to distinguish between the two separate peaks. It should be noted that both the D- and G-peak positions of the benchmark sample, AW128, tend to decrease in wave-number, i.e., exhibit a horizontal shift towards the left, in response to an increase in the Raman source wavelength; the locations of the D- and G-peaks are indicated with the arrows in Figures 4.8, 4.9, and 4.10.

Unprocessed Raman spectra, corresponding to the rf magnetron sputtering reference sample, MS115, are depicted in Figures 4.11, 4.12, and 4.13, these spectra being determined using the 325, 442, and 633 nm Raman sources, respectively. The spectral data between 1000 and 2000 cm^{-1} are plotted, as this is the region over which the important peaks required for this analysis are apparent. The D- and G-peaks, around 1350 and 1580 cm^{-1}, respectively, are noted in Figures 4.11, 4.12, and 4.13. As was mentioned before, according to the suggestion of Zhao *et al.* [82], these peaks represent the presence of sp^2 and sp^3 carbon bonding, respectively. While the spectral data acquired with the 325 nm source wavelength exhibits greater levels of noise than that associated with the other Raman spectra, two distinct peaks are clearly observed for this source wavelength corresponding to this particular sample, MS115. It is observed that when probed using the 442 nm source wavelength, the Raman data is less noisy and shows a larger D-peak. This trend continues with the 633 nm source wavelength, a much larger D-peak being observed for this case, this particular spectral data being smooth compared with the other Raman spectra; I take this to suggest that this spectrum corresponding to this particular sample is the one with the least noise amongst the three spectra considered. It should be noted that both the D- and G-peak positions of the benchmark sample, MS115, tend

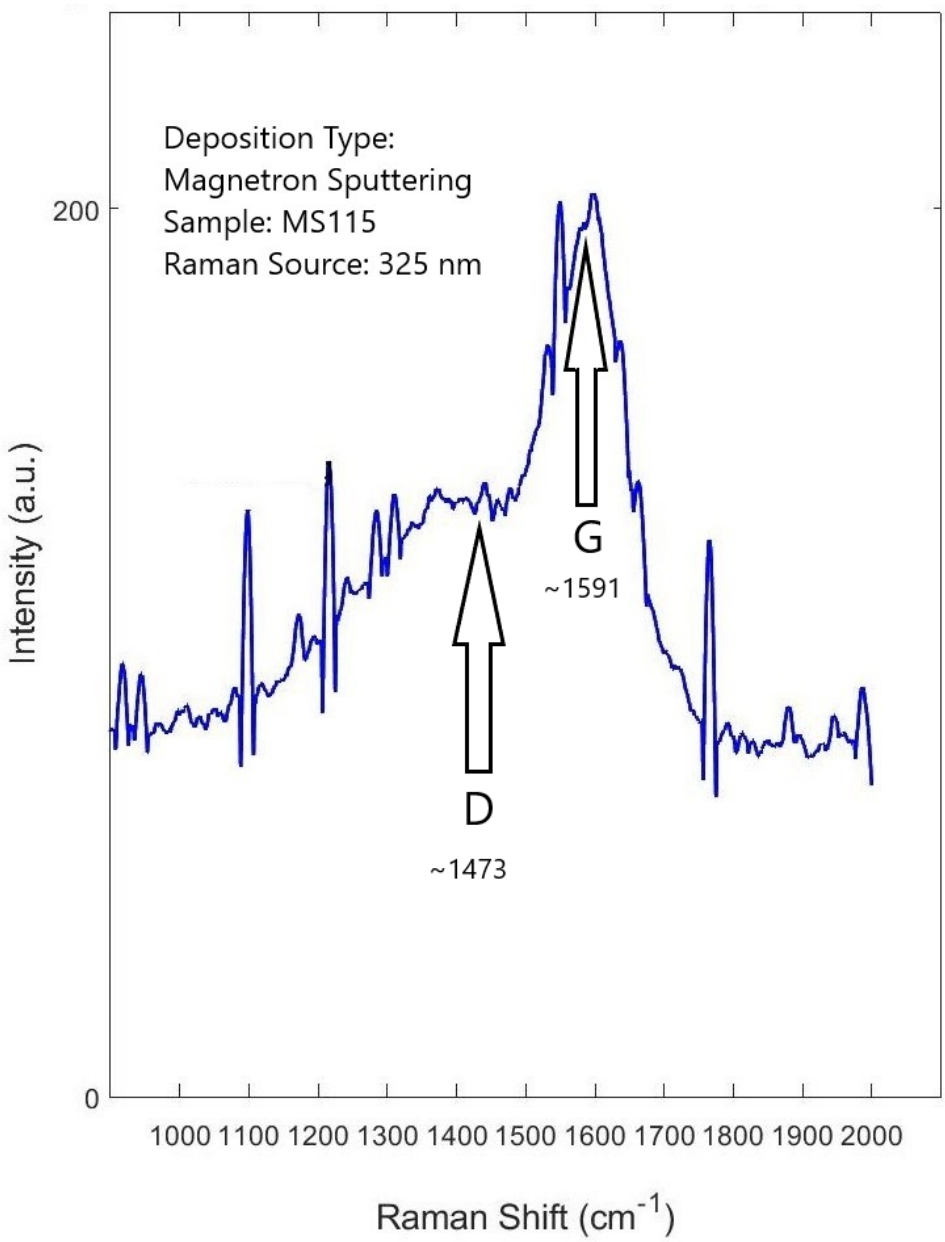

Figure 4.11: The unprocessed Raman spectral data associated with sample MS115 for the source wavelength set to 325 nm. The locations of D-peak and G-peak are indicated with the arrows. Created by Ashraf Ahsan, used by permission. The online version of this figure is depicted in color.

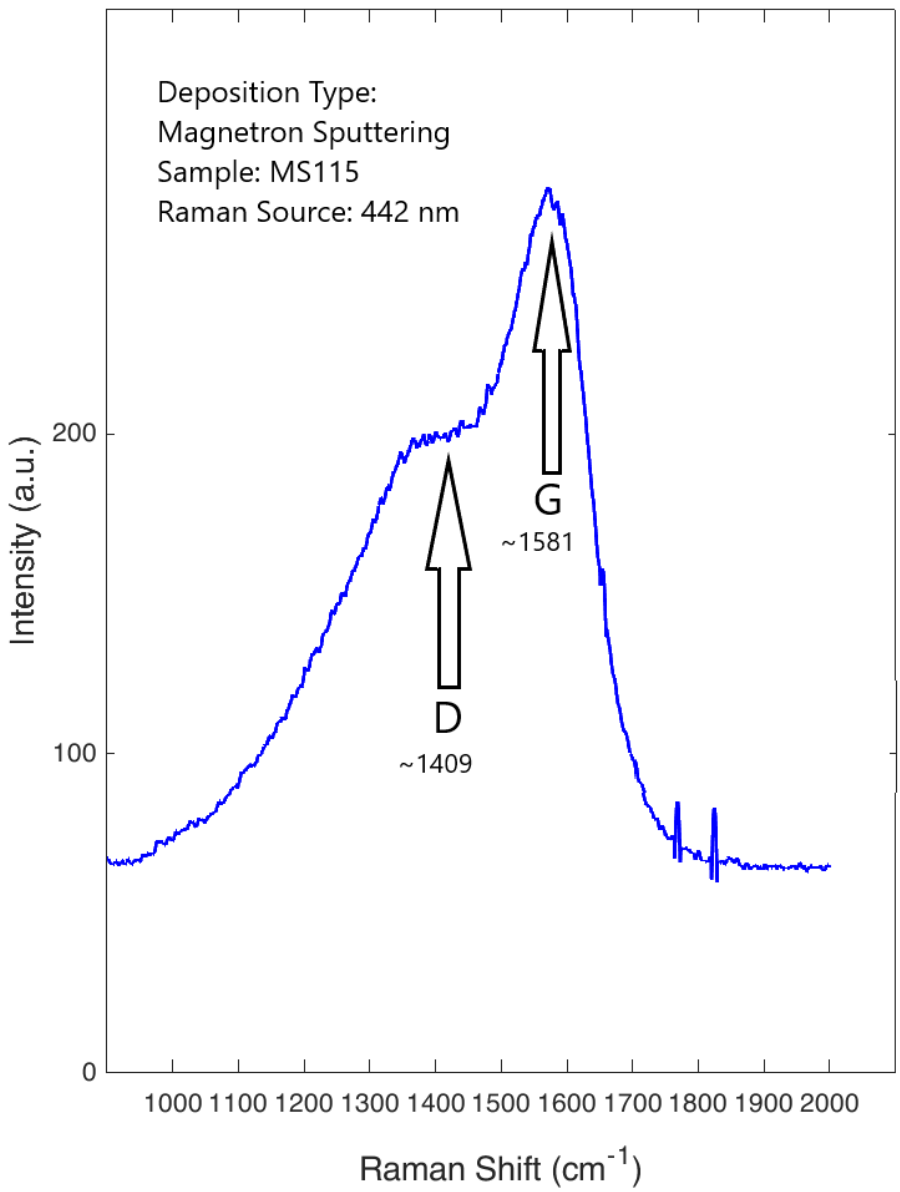

Figure 4.12: The unprocessed Raman spectral data associated with sample MS115 for the source wavelength set to 442 nm. The locations of D-peak and G-peak are indicated with the arrows. Created by Ashraf Ahsan, used by permission. The online version of this figure is depicted in color.

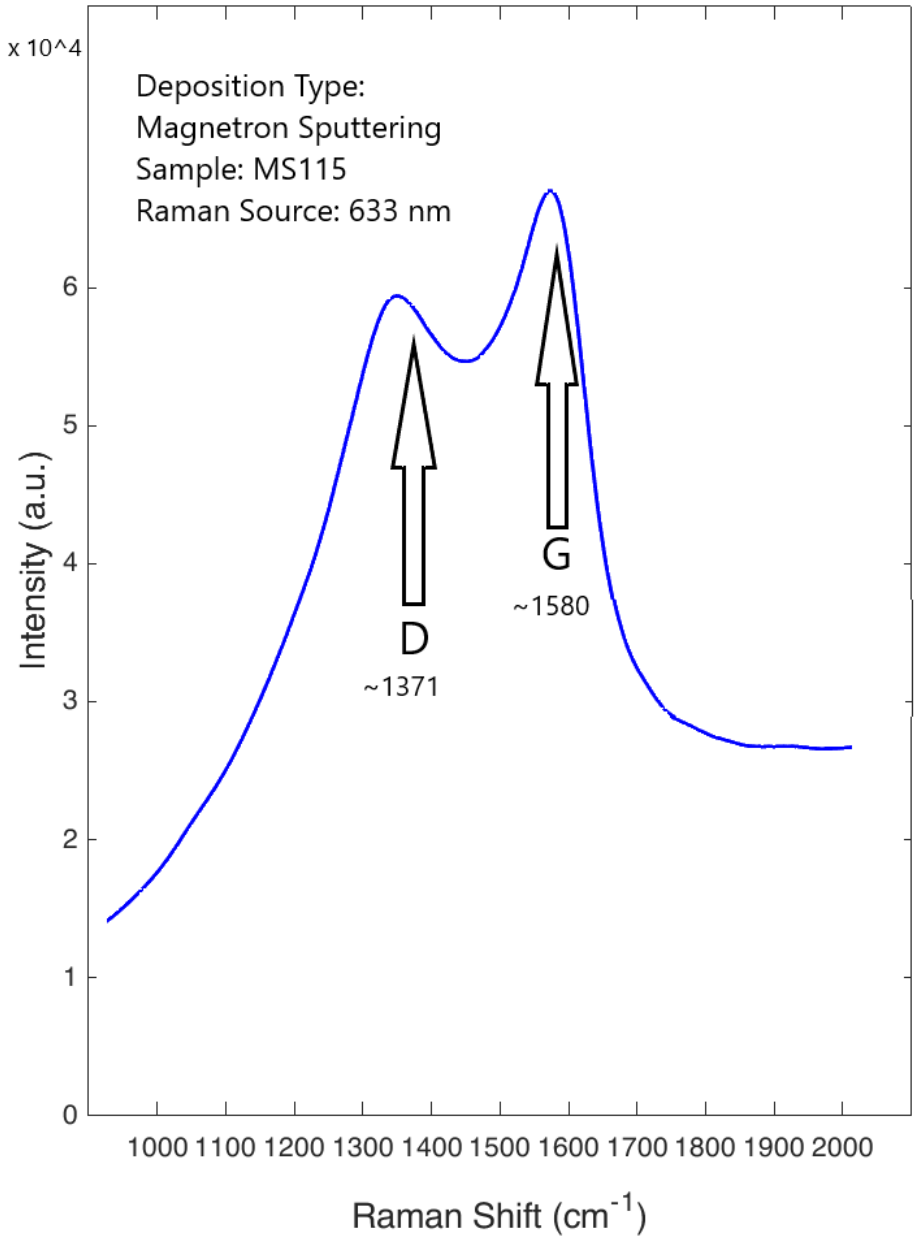

Figure 4.13: The unprocessed Raman spectral data associated with sample MS115 for the source wavelength set to 633 nm. The locations of D-peak and G-peak are indicated with the arrows. Created by Ashraf Ahsan, used by permission. The online version of this figure is depicted in color.

to decrease in wave-number, i.e., exhibit a horizontal shift towards the left, in response to an increase in the Raman source wavelengths; the locations of the D- and G-peaks are indicated with the arrows in Figures 4.11, 4.12, and 4.13.

4.6 Identification of the baseline

Prior to peak decomposition, a given Raman spectrum must be baseline corrected. This involves identifying the baseline itself and then removing it from the corresponding spectrum. There are a number of ways through which baseline correction can be performed, the essence being the same for all. A simplified one, which involves the drawing of a straight line from about 1000 cm^{-1} to around 1800 cm^{-1}, as suggested by Zhao *et al.* [82], is employed here. Subsequently, a process of normalization is performed on the baseline corrected data. It involves the linear mapping of every amplitude value to a normalized amplitude, where the highest value is mapped to 1 and the lowest value to 0 [87]. Baseline identification, corresponding to the normalized Raman spectra, for the case of the PECVD deposited reference sample, AW128, are depicted in Figures 4.14, 4.15, and 4.16, for the spectra acquired using source wavelengths 325, 442, and 633 nm, respectively. Baseline identification, corresponding to normalized Raman spectra, for the case of the magnetron sputtering reference sample, MS115, are depicted in Figures 4.17, 4.18, and 4.19, for the spectra excited using the source wavelengths 325, 442, and 633 nm, respectively.

The normalized and baseline identified Raman spectral data corresponding to the PECVD reference sample, AW128, are depicted in Figures 4.14, 4.15, and 4.16 for the spectra acquired using the Raman source wavelengths

325, 442, and, 633 nm, respectively. The normalized and baseline identified Raman spectral data corresponding to the magnetron sputtered reference sample, MS115, are depicted in Figures 4.17, 4.18, and 4.19, for the spectra acquired using the source wavelengths 325, 442, and 633 nm, respectively. All of the other normalized and baseline identified Raman spectra, corresponding to the other thin-films of carbon considered in this analysis, exhibit a similar behavior.

4.7 Peak fitting and interpretation

With the Raman spectral data baseline corrected and normalized, one can now decompose these spectra into a sum over two peaks, one representing the D-peak and the other representing the G-peak. Typically, this is done by fitting a sum over two peaks to the baseline corrected and normalized experimental spectral data. A least-squares fit criterion is usually employed in resolving the two-peak fittings, the peak fitting parameters, corresponding to the magnitude, the position, and the breadth of the peaks, being selected in such a manner so as to minimize the difference between the sum over the two peaks and the experimentally acquired baseline corrected and normalized spectra. Thus far, researchers have fit thin-film carbon Raman spectral data using Gaussian, Gaussian-Lorentzian, Lorentztian, and many other types of peak fitting profiles. The nature of the Raman peaks governs the type of fitting profile that should be employed [88].

Based on the amount of noise observed in the Raman spectra, the Gaussian fit was determined to be adequate for the purposes of this particular analysis. Within the context of this selection, the form of each peak is of

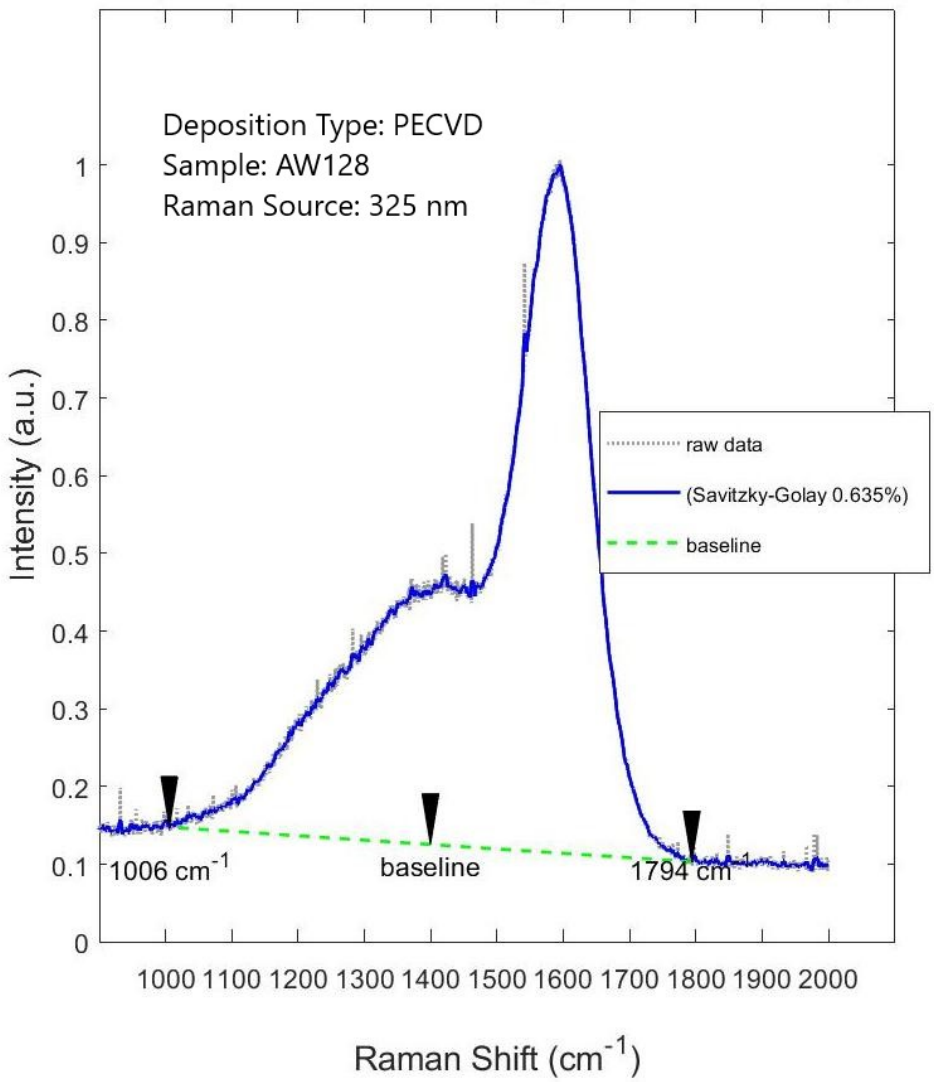

Figure 4.14: Baseline identification for the case of the normalized Raman spectral data associated with sample AW128 for the source wavelength set to 325 nm. Created by Ashraf Ahsan, used by permission. The online version of this figure is depicted in color.

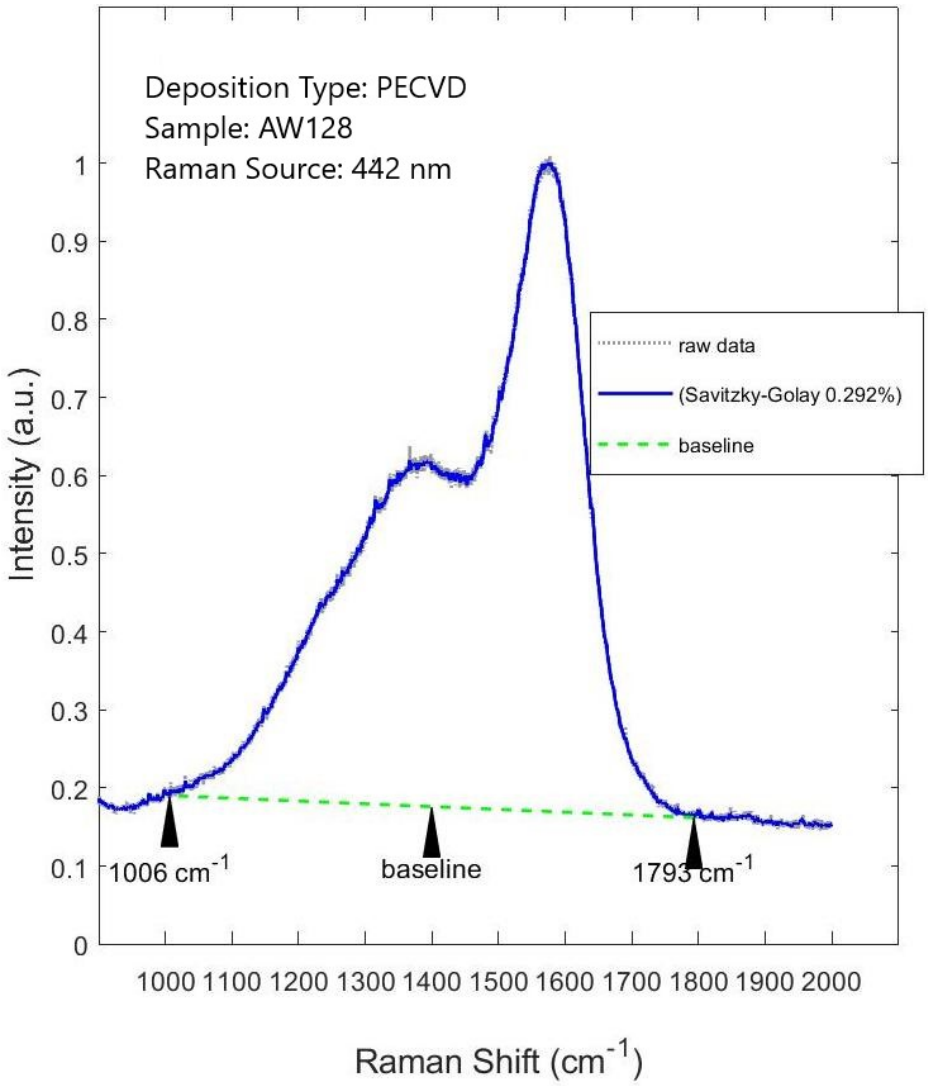

Figure 4.15: Baseline identification for the case of the normalized Raman spectral data associated with sample AW128 for the source wavelength set to 442 nm. Created by Ashraf Ahsan, used by permission. The online version of this figure is depicted in color.

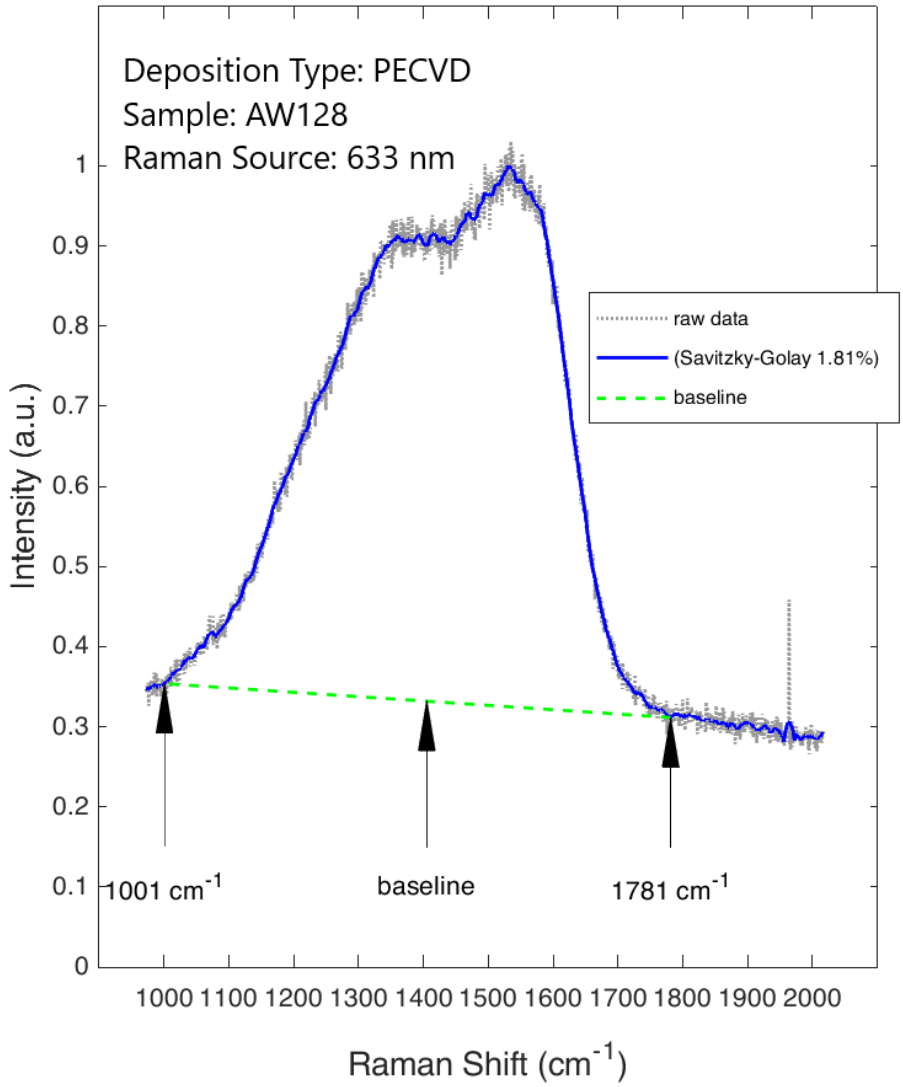

Figure 4.16: Baseline identification for the case of the normalized Raman spectral data associated with sample AW128 for the source wavelength set to 633 nm. Created by Ashraf Ahsan, used by permission. The online version of this figure is depicted in color.

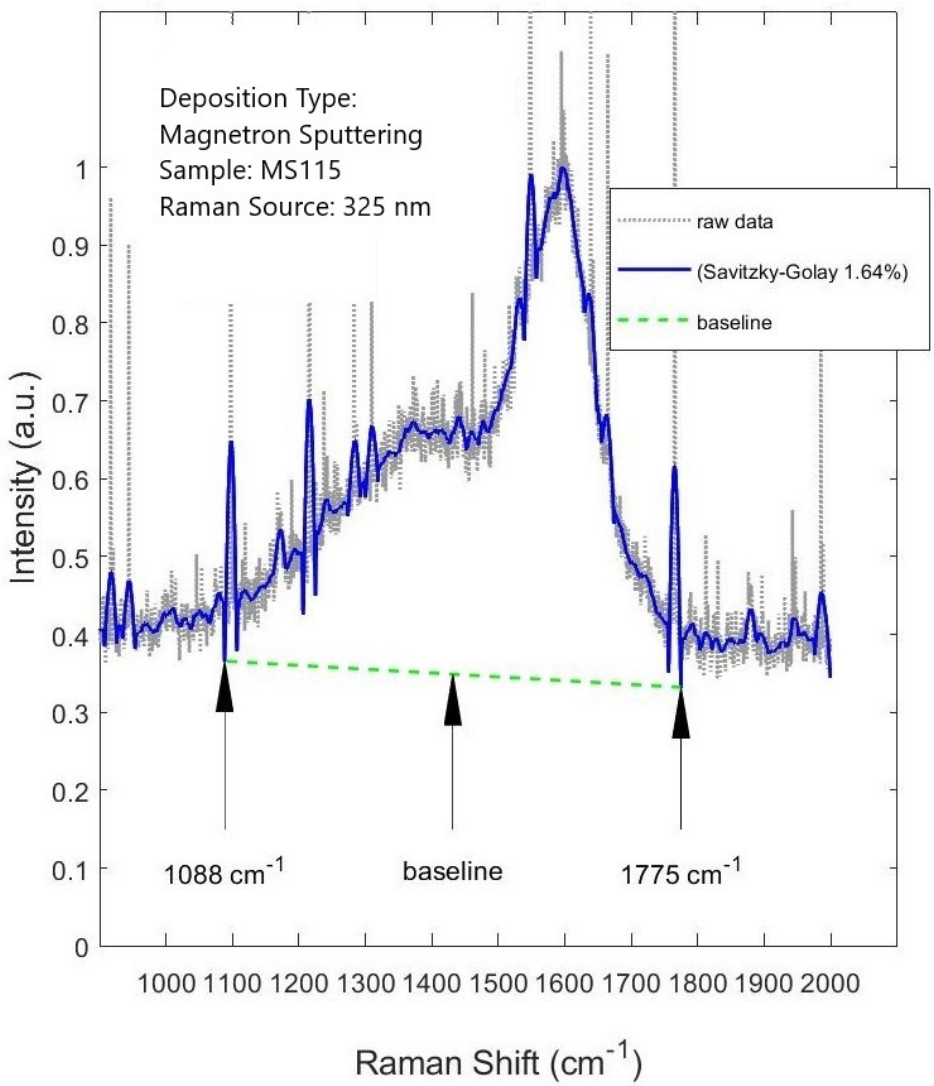

Figure 4.17: Baseline identification for the case of the normalized Raman spectral data associated with sample MS115 for the source wavelength set to 325 nm. Created by Ashraf Ahsan, used by permission. The online version of this figure is depicted in color.

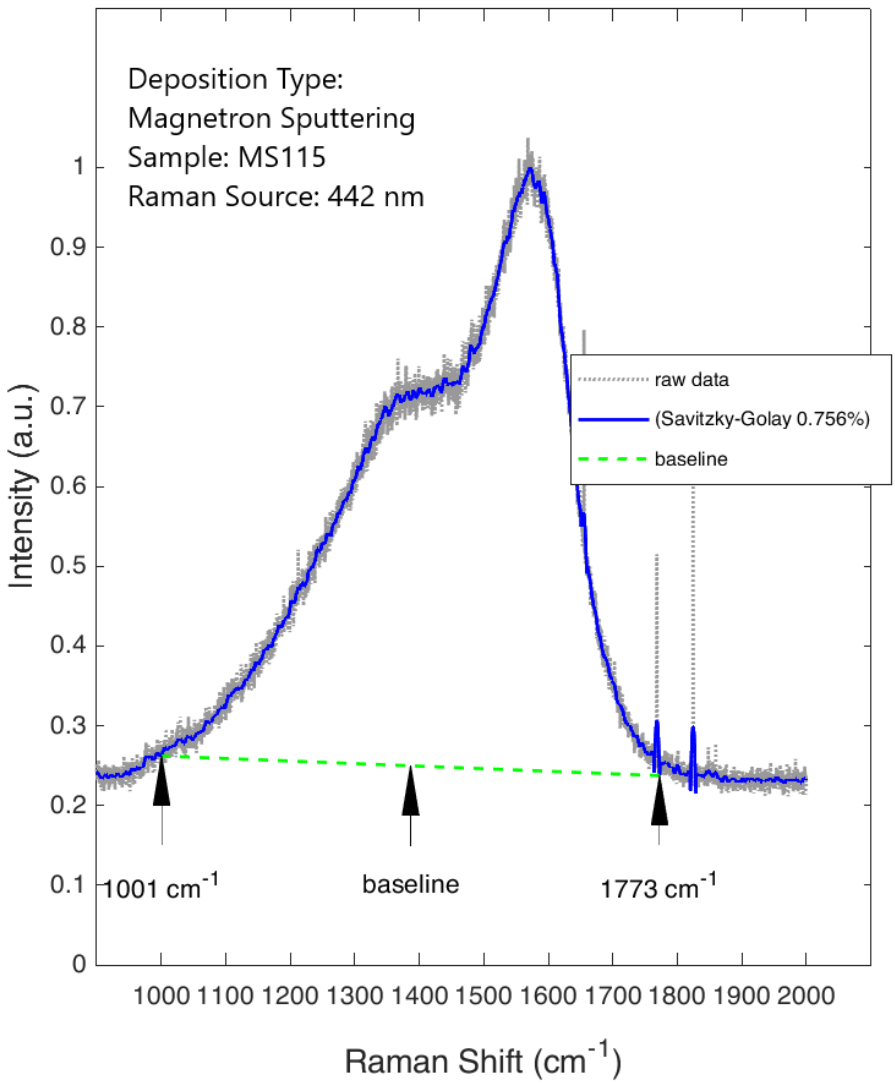

Figure 4.18: Baseline identification for the case of the normalized Raman spectral data associated with sample MS115 for the source wavelength set to 442 nm. Created by Ashraf Ahsan, used by permission. The online version of this figure is depicted in color.

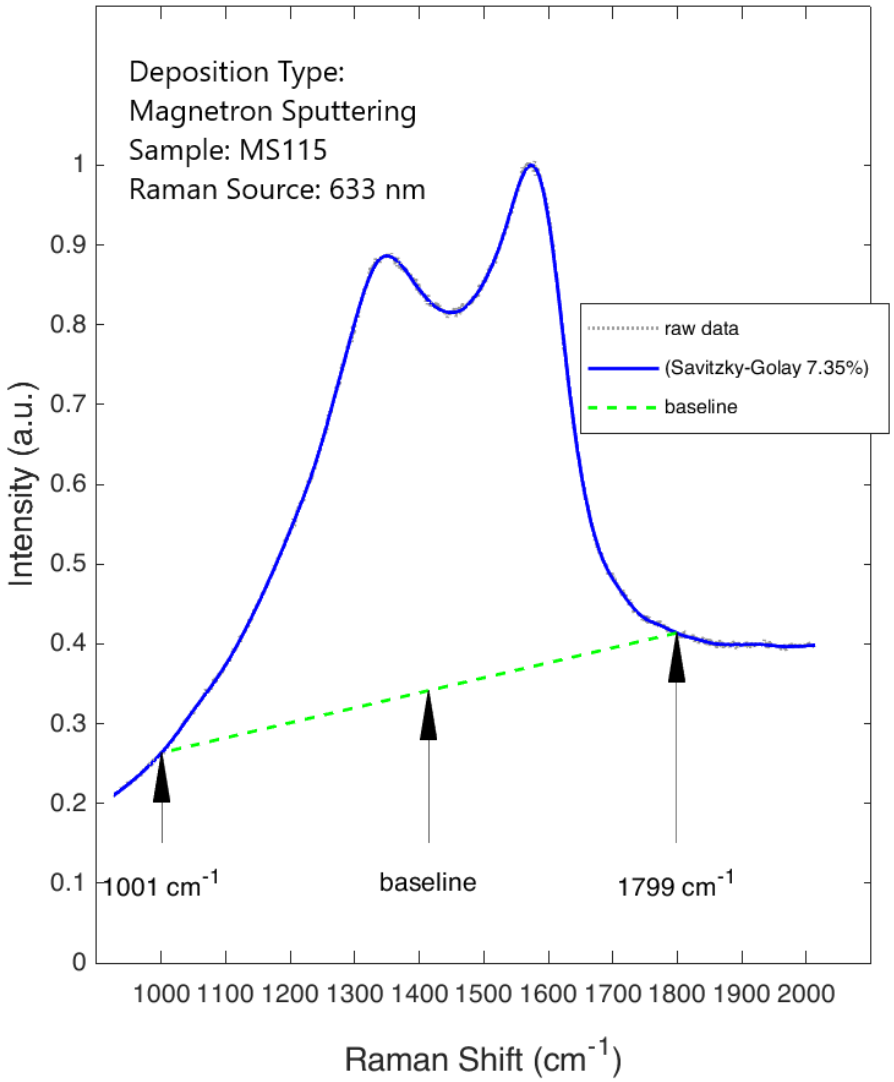

Figure 4.19: Baseline identification for the case of the normalized Raman spectral data associated with sample MS115 for the source wavelength set to 633 nm. Created by Ashraf Ahsan, used by permission. The online version of this figure is depicted in color.

the form

$$Ae^{-(x-m)^2/2\sigma^2}, \tag{4.1}$$

where A denotes the amplitude of peak, m refers to the peak location, and σ provides measure of the peak breadth. Therefore, for the purposes of this analysis, the sum over two Gaussian peaks, i.e.,

$$A_D e^{-(x-m_D)^2/2\sigma^2} + A_G e^{-(x-m_G)^2/2\sigma^2}, \tag{4.2}$$

is fit to the baseline corrected normalized Raman spectra, where the peak amplitudes of D- and G-peaks are denoted as A_D and A_G, respectively, the peak locations are represented by m_D and m_G, and the peak breadths are σ_D and σ_G, respectively.

Peak fittings, for the baseline corrected and normalized Raman spectra, corresponding to the PECVD reference sample, AW128, are depicted in Figures 4.20, 4.21, and 4.22, these spectra being acquired using the 325, 442, and 633 nm Raman sources, respectively; Figures 4.8, 4.9, and 4.10 depict the corresponding unprocessed Raman spectra. The results acquired are representative of that expected for the case of thin-film carbon, i.e., a broad D-peak followed by a sharp and narrow G-peak.

Peak fittings, for the baseline corrected and normalized Raman spectra, corresponding to the magnetron sputtering reference sample, MS115, are depicted in Figures 4.23, 4.24, and 4.25, these spectra being determined using the 325, 442, and 633 nm Raman sources, respectively; Figures 4.11, 4.12, and 4.13 depict the corresponding unprocessed Raman spectra. The results acquired are representative of that expected for the case of thin-film carbon, i.e., a broad D-peak followed by a sharp and narrow G-peak.

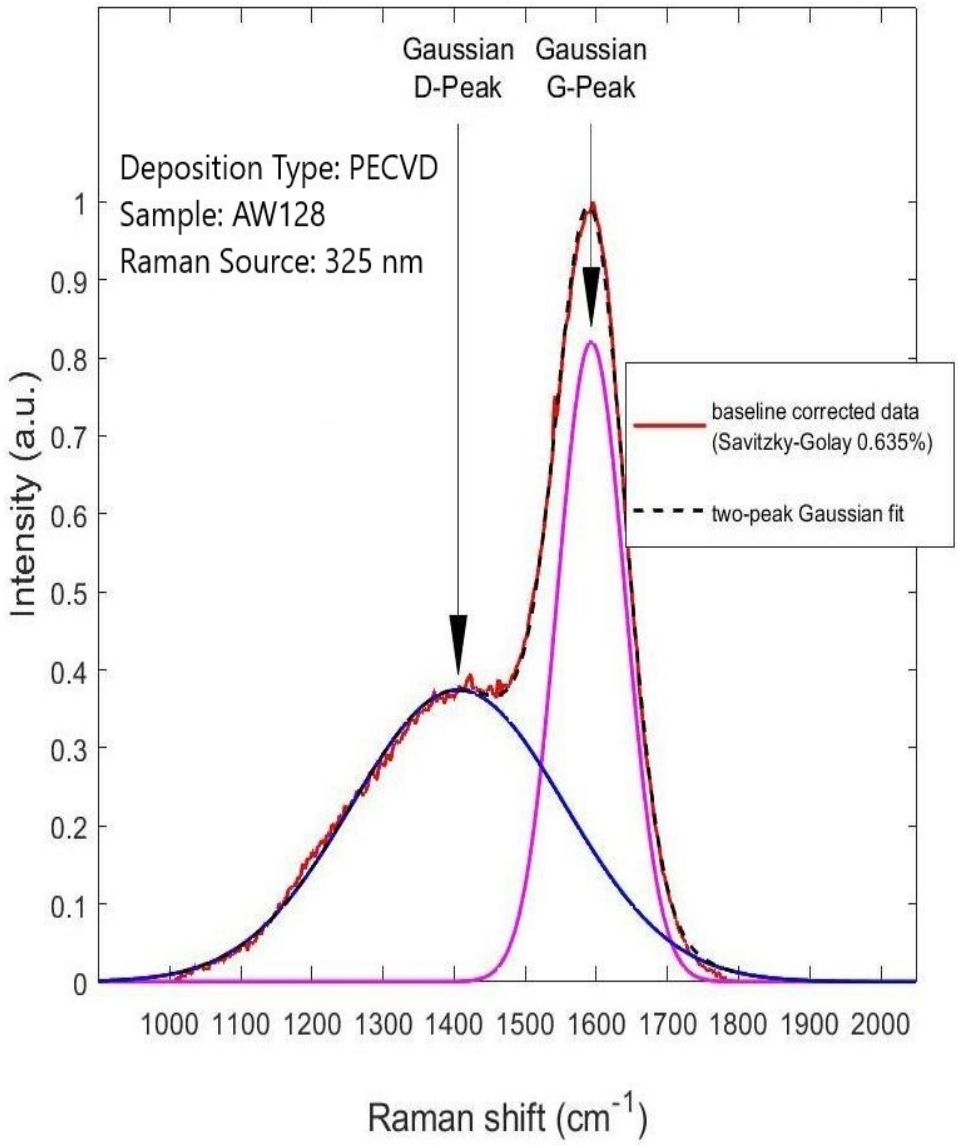

Figure 4.20: Raman interpretation of AW128 obtained using a 325 nm laser wavelength with baseline removal. The baseline corrected and normalized Raman spectral data associated with sample AW128 is depicted. A peak fitted result, corresponding to this baseline corrected and normalized data, is depicted, the peaks being Gaussian in nature. Created by Ashraf Ahsan, used by permission. The online version of this figure is depicted in color.

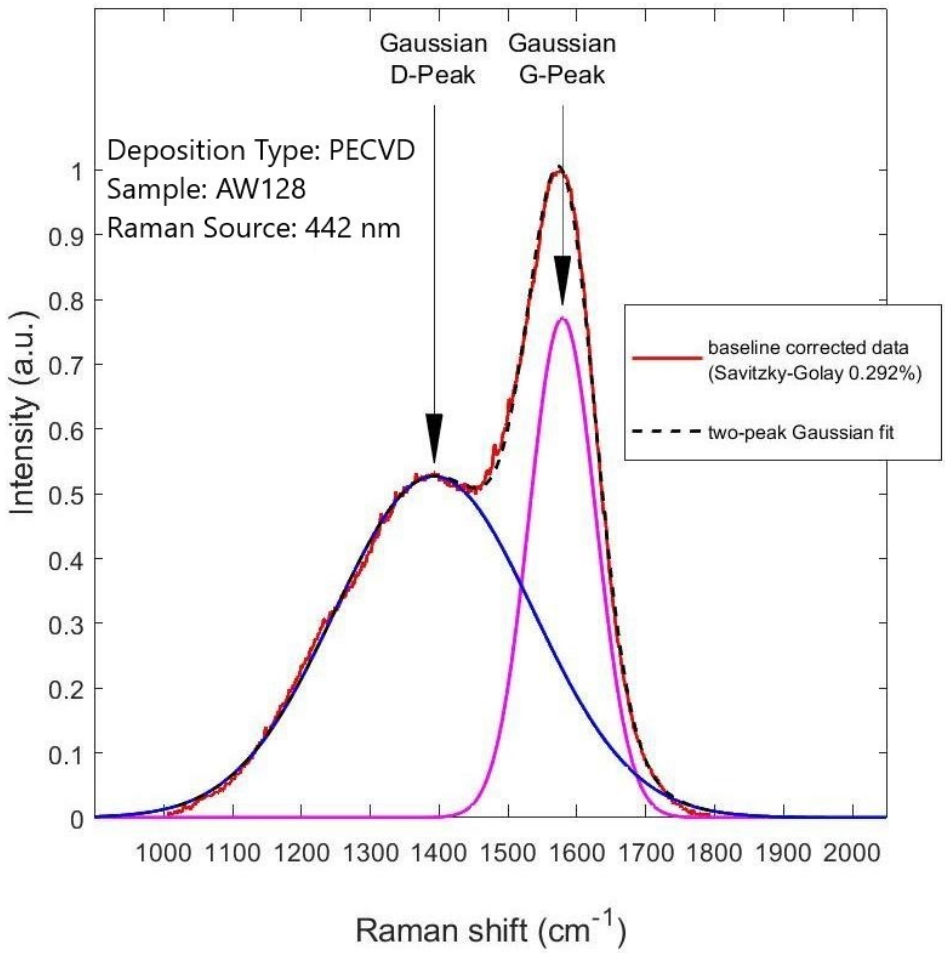

Figure 4.21: Raman interpretation of AW128 obtained using a 442 nm laser wavelength with baseline removal. The baseline corrected and normalized Raman spectral data associated with sample AW128 is depicted. A peak fitted result, corresponding to this baseline corrected and normalized data, is depicted, the peaks being Gaussian in nature. Created by Ashraf Ahsan, used by permission. The online version of this figure is depicted in color.

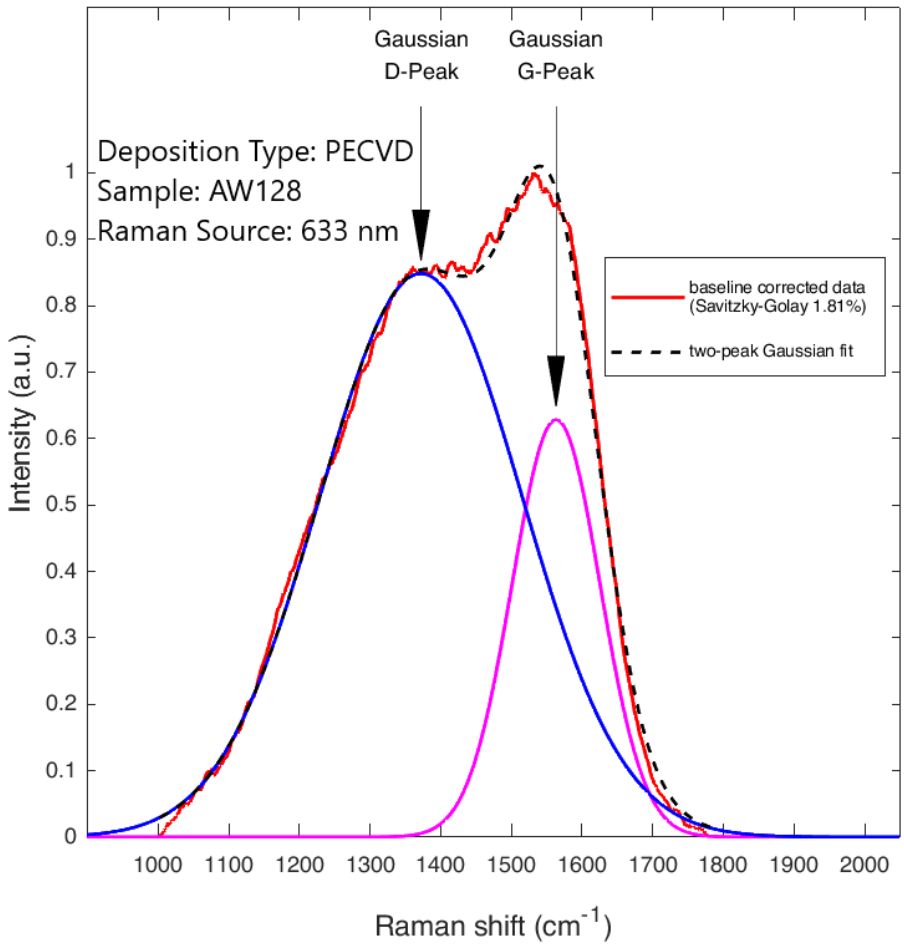

Figure 4.22: Raman interpretation of AW128 obtained using a 633 nm laser wavelength with baseline removal. The baseline corrected and normalized Raman spectral data associated with sample AW128 is depicted. A peak fitted result, corresponding to this baseline corrected and normalized data, is depicted, the peaks being Gaussian in nature. Created by Ashraf Ahsan, used by permission. The online version of this figure is depicted in color.

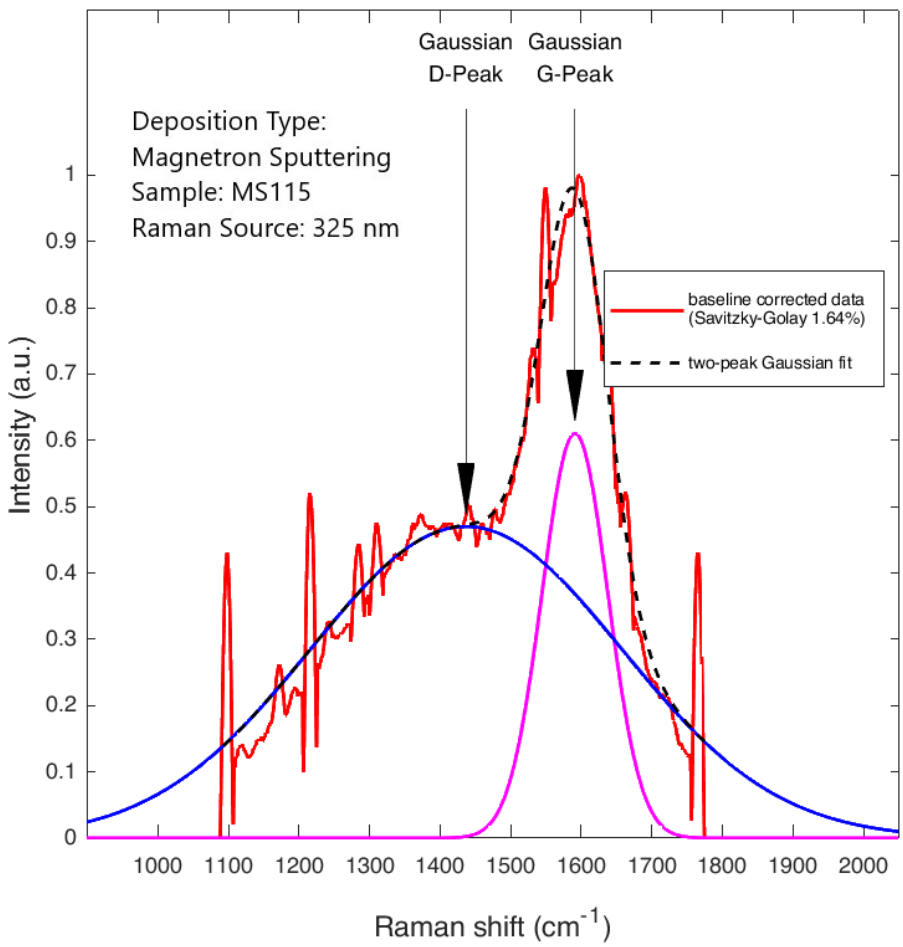

Figure 4.23: Raman interpretation of MS115 obtained using a 325 nm laser wavelength with baseline removal. The baseline corrected and normalized Raman spectral data associated with sample MS115 is depicted. A peak fitted result, corresponding to this baseline corrected and normalized data, is depicted, the peaks being Gaussian in nature. Created by Ashraf Ahsan, used by permission. The online version of this figure is depicted in color.

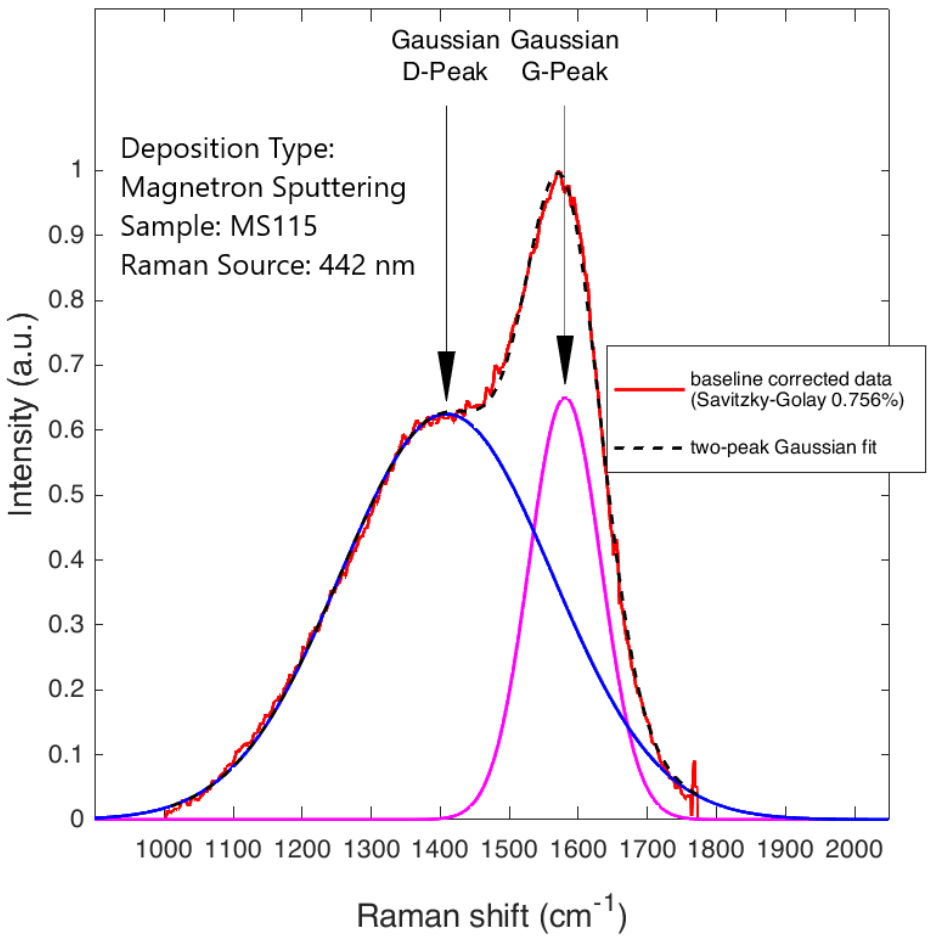

Figure 4.24: Raman interpretation of MS115 obtained using a 442 nm laser wavelength with baseline removal. The baseline corrected and normalized Raman spectral data associated with sample MS115 is depicted. A peak fitted result, corresponding to this baseline corrected and normalized data, is depicted, the peaks being Gaussian in nature. Created by Ashraf Ahsan, used by permission. The online version of this figure is depicted in color.

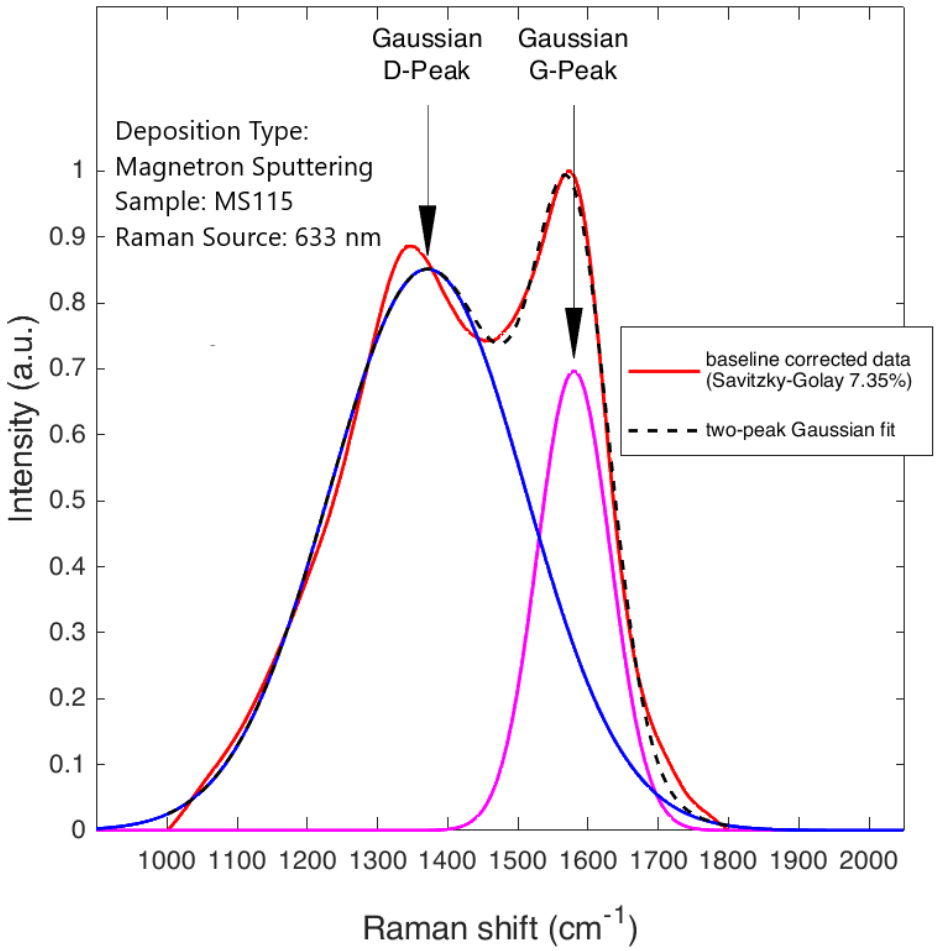

Figure 4.25: Raman interpretation of MS115 obtained using a 633 nm laser wavelength with baseline removal. The baseline corrected and normalized Raman spectral data associated with sample MS115 is depicted. A peak fitted result, corresponding to this baseline corrected and normalized data, is depicted, the peaks being Gaussian in nature. Created by Ashraf Ahsan, used by permission. The online version of this figure is depicted in color.

As was mentioned in Section 4.6, selecting the baseline, spanning from around 1000 cm^{-1} to about 1800 cm^{-1}, provides a satisfactory baseline correction for both of the benchmark samples, i.e., AW128 and MS115.

4.8 Discussion

The dependence of the integrated intensity ratio, I_D/I_G on the amplitude intensity ratio, A_D/A_G, is now examined. In Figures 4.26, 4.27, and 4.28, the dependence of I_D/I_G on A_D/A_G, for the samples considered in this analysis, is considered.

Results corresponding to each sample considered, for the three different source wavelengths employed, i.e., 325, 442, and 633 nm, are plotted in this figure. It is noted that there is indeed a relationship corresponding to each source wavelength. It is noted that increased A_D/A_G corresponds to increased I_D/I_G, for all source wavelengths considered. In particular, a linear least-squares error fit demonstrates a linear relationship between A_D/A_G and I_D/I_G. In particular, least-squares fits demonstrate that

$$\frac{I_D}{I_G} = 5.2\frac{A_D}{A_G} + (-0.87), \quad (325\,\text{nm}) \tag{4.3}$$

$$\frac{I_D}{I_G} = 3.54\frac{A_D}{A_G} + (-0.49), \quad (442\,\text{nm}) \tag{4.4}$$

$$\frac{I_D}{I_G} = 2.59\frac{A_D}{A_G}) + (-0.43), \quad (633\,\text{nm}) \tag{4.5}$$

where Eqs. (4.3), (4.4), and (4.5), correspond to the source wavelengths 325, 442, and 633 nm, respectively. The slope of this relationship decreases as the source wavelength is increased, as can be seen in Figure 4.27. It is also noted that the data points for the 325 nm measurements are the most tightly

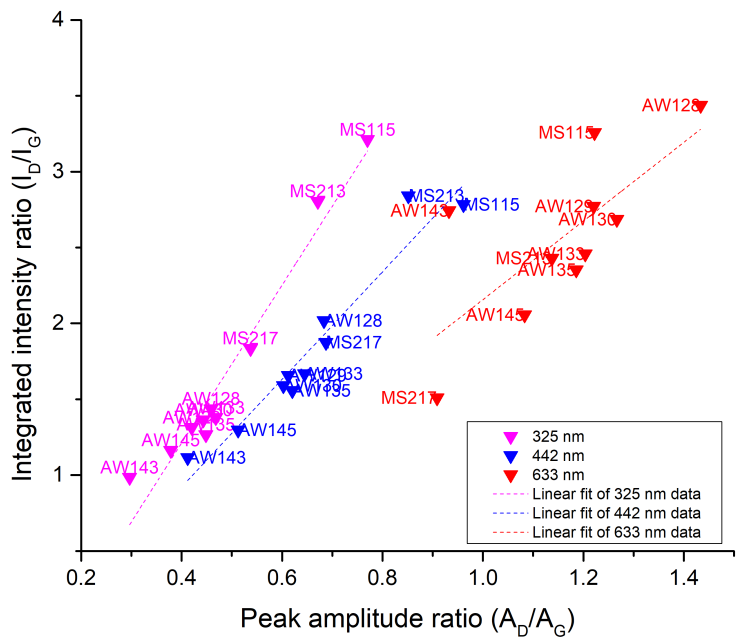

Figure 4.26: The relationship between the A_D/A_G and I_D/I_G, for both PECVD and rf and dc magnetron sputtering prepared samples of thin-film carbon. Created by Ashraf Ahsan, used by permission. The online version of this figure is depicted in color.

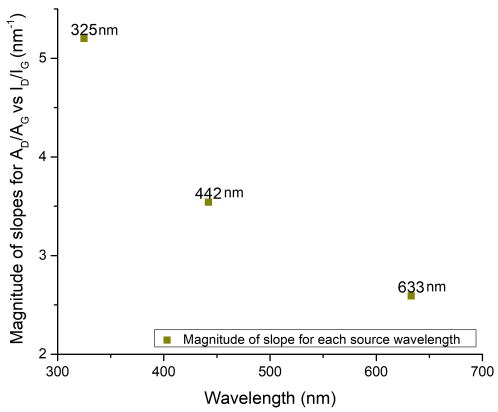

Figure 4.27: Relationship for the slope of the amplitude ratio of D- and G-peaks with the integrated intensity ratio of D- and G-peaks for both PECVD and rf and dc magnetron sputtering samples, for each source wavelength. The online version of this figure is depicted in color.

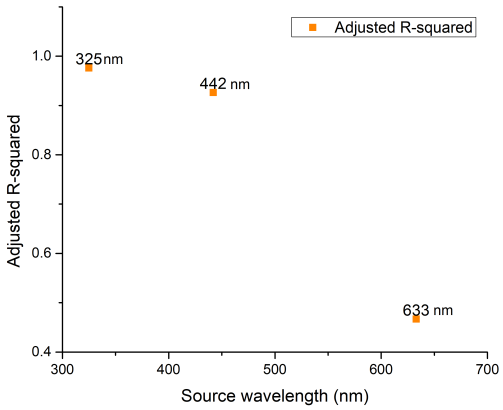

Figure 4.28: Relationship for the adjusted R-squared value of the slopes of the amplitude ratio of D- and G-peaks with the integrated intensity ratio of D- and G-peaks for both PECVD and rf and dc magnetron sputtering samples, for each source wavelength. The online version of this figure is depicted in color.

distributed about the corresponding linear least-square fit. The variations about this linear relationship get more scattered as the source wavelength is increased. Hence, the 633 nm data points are less tightly distributed about the corresponding linear least-squares fit result compared to the 325 nm measurements. The relationship for the adjusted R-squared value of the slopes of the amplitude ratio of D- and G-peaks with the integrated intensity ratio of D- and G-peaks for both PECVD and rf and dc magnetron sputtering samples, for each source wavelength, has been statistically evaluated to measure how closely the data are located to the linear least-squares fit, as can be seen in Figure 4.28. It should be noted that an adjusted R-squared of 1 means that all the data points are exactly on the line of best fit[3]. From Figure 4.28, it is seen that the proportion of variance in the $\mathrm{I}_D/\mathrm{I}_G$ can be correlated and predicted from the A_D/A_G, where the 325 nm source wavelength produces a stronger correlation compared with the 442 nm source wavelength, which in turn tends to produces a stronger correlation compared with the 633 nm source wavelength.

The thin-film carbon literature suggests that both $\mathrm{I}_D/\mathrm{I}_G$ and $\mathrm{A}_D/\mathrm{A}_G$ are directly related to the material properties of the thin-films of carbon. Table 4.1 contains the important parameters corresponding to the PECVD samples. The table consists of the sample numbers, the powers supplied to the chamber during the TMS layer deposition step, and the DLC layer step for deposition. The Raman spectral data, corresponding all three source wavelengths that are considered, including the mean positions of the D- and G-peaks, followed by the integrated intensity ratio, $\mathrm{I}_D/\mathrm{I}_G$, and the amplitude

[3]The adjusted R-squared evaluation corresponds to a modification of that corresponding to the R-squared evaluation that is applicable to cases with a large number of predictors in the model. This is the case here. Further details are adequately discussed in the literature [89].

ratio, A_D/A_G, respectively, of the peaks presented in this table. Similarly, Table 4.2 provides information on the sample names, the duration of the pumping out of the existing or previous gases from the deposition chamber, the pre-sputtering and sputtering temperatures inside the chamber, followed by the integrated intensity ratio, I_D/I_G, and the amplitude ratio, A_D/A_G, respectively, of the peaks for all three Raman source wavelengths.

Table 4.1: Parameters for evaluating the PECVD samples.

Sample	TMS layer power (W)	DLC layer power (W)	Wave-length (nm)	D-peak position (cm^{-1})	G-peak position (cm^{-1})	Integrated intensity ratio (I_D/I_G)	Amplitude ratio (A_D/A_G)
AW128	120	200	325	1406	1593	1.45	0.46
			442	1393	1579	2.02	0.68
			633	1376	1564	3.44	1.35
AW129	120	200	325	1403	1591	1.31	0.42
			442	1391	1575	1.66	0.61
			633	1374	1558	2.77	1.22
AW130	120	200	325	1406	1591	1.36	0.44
			442	1397	1576	1.59	0.60
			633	1366	1554	2.69	1.27
AW133	120	200	325	1406	1592	1.38	0.47
			442	1395	1575	1.67	0.65
			633	1369	1555	2.46	1.20
AW135	120	200	325	1407	1593	1.27	0.45
			442	1397	1575	1.56	0.62
			633	1370	1553	2.35	1.19
AW143	100	100	325	1393	1590	0.99	0.30
			442	1384	1562	1.12	0.41
			633	1319	1501	2.74	0.93
AW145	120	150	325	1402	1589	1.16	0.38
			442	1387	1568	1.30	0.51
			633	1354	1542	2.06	1.08

Table 4.2: Parameters for evaluating rf and dc magnetron sputtering samples.

Sample	Pump down duration (min)	Pre-sputtering temperature (°C)	Sputtering temperature (°C)	Wave-length (nm)	D-peak position (cm^{-1})	G-peak position (cm^{-1})	Integrated intensity ratio (I_D/I_G)	Amplitude ratio (A_D/A_G)
MS115	62	30	76	325	1437	1591	3.21	0.77
				442	1409	1581	2.78	0.96
				633	1371	1580	3.26	1.22
MS213	75	32	72	325	1423	1597	2.80	0.67
				442	1400	1590	2.84	0.85
				633	1385	1560	2.43	1.14
MS217	86	17	70	325	1416	1594	1.84	0.54
				442	1408	1575	1.88	0.69
				633	1348	1541	1.51	0.91

Chapter 5

Conclusions

Through an examination of the Raman spectra associated with a number of representative carbon thin-films, these thin-films having been prepared by another researcher [44], it has been established that the amplitude ratio, A_D/A_G, is related to the corresponding integrated intensity ratio, I_D/I_G. The samples of thin-film carbon had been prepared through the use of PECVD and rf and dc magnetron sputtering. The slope of this relationship was shown to be determined by the source wavelength, larger source wavelengths corresponding to a lower slope. The scatter about the linear fit was found to increase as the source wavelength is increased[4].

Recommendations for further work include the gathering of more samples from each deposition technique along with an increase in the number of source wavelengths to conduct Raman spectroscopy. It might be of interest to employ other techniques, such as X-ray photoelectron spectroscopy, to measure the elemental configuration, and a scanning electron microscope to observe the surface topography and thickness of the carbon thin-films. Gradually, the effects of different interlayers and the adhesion strength will need to be measured depending on the substrate type and geometry. The hardness test of all of the samples need to be conducted using a nanoindenter. Finally, further deposition techniques needs to be explored. This will have

[4]One limitation to the results is the fact that I am not exactly sure as to how broad a sampling over the thin-film carbon genome was actually performed.

to be done in the future.

Bibliography

[1] R. Dillon, J. A. Woollam, and V. Katkanant, "Use of raman scattering to investigate disorder and crystallite formation in as-deposited and annealed carbon films," *Physical Review B*, vol. 29, no. 6, p. 3482, 1984. → pages ix, 1, 8, 32

[2] A. Varade, K. N. Reddy, D. Sasen, A. Krishna, M. Chellamalai, and P. Shashikumar, "Detailed raman study of dlc coating on si (100) made by rf-pecvd," *Procedia Engineering*, vol. 97, pp. 1452–1456, 2014. → pages ix, 8, 35

[3] I. R. Lewis and H. Edwards, *Handbook of Raman Spectroscopy: From the Research Laboratory to the Process Line*, ser. Practical Spectroscopy. CRC Press, 2001. → pages 27, 31, 32, 36, 37, 38, 39

[4] S. Gould, Robert D.and Kasap and A. K. Ray, *Thin Films*, S. Kasap and P. Capper, Eds. Cham: Springer International Publishing, 2017. [Online]. Available: https://doi.org/10.1007/978-3-319-48933-9_28 → pages 1

[5] M. Eslamian, "Inorganic and organic solution-processed thin film devices," *Nano-micro letters*, vol. 9, no. 1, p. 3, 2017. → pages 1

[6] K. L. Chopra and S. R. Das, "Thin film deposition techniques," in *Thin Film Solar Cells*. Springer, 1983, pp. 195–273. → pages 1, 25

[7] X. Xie, J. Kang, W. Cao, J. H. Chu, Y. Gong, P. M. Ajayan, and K. Banerjee, "Designing artificial 2d crystals with site and size controlled quantum dots," *Scientific reports*, vol. 7, no. 1, p. 9965, 2017. → pages 1

[8] K. Wasa, M. Kitabatake, and H. Adachi, *Thin Film Materials Technology-Sputtering of Compound Materials*. Norwich, NY: William Andrew Publishing and Springer-Verlag, 2004. → pages 1

[9] K. Reichelt, "Nucleation and growth of thin films," *Vacuum*, vol. 38, no. 12, pp. 1083–1099, 1988. → pages 1

[10] T. Hosokai, A. Hinderhofer, F. Bussolotti, K. Yonezawa, C. Lorch, A. Vorobiev, Y. Hasegawa, Y. Yamada, Y. Kubozoro, A. Gerlach *et al.*, "Thickness and substrate dependent thin film growth of picene and impact on the electronic structure," *The Journal of Physical Chemistry C*, vol. 119, no. 52, pp. 29 027–29 037, 2015. → pages 1

[11] R. M. Miranda, J. P. Gandra, P. Vilaca, L. Quintino, and T. G. Santos, *Surface modification by solid state processing*. Woodhead Publishing, 2013. → pages 2

[12] S. Mammeri, M. Msimanga, A. Dib, H. Ammi, and C. Pineda-Vargas, "Sputtering of bismuth thin films under mev cu heavy ion irradiation: Experimental data and inelastic thermal spike model interpretation." *Surface and Interface Analysis*, vol. 50, no. 3, pp. 328–334, 2018. → pages 2

[13] J. Gracio, Q. Fan, and J. Madaleno, "Diamond growth by chemical

vapour deposition," *Journal of Physics D: Applied Physics*, vol. 43, no. 37, p. 374017, 2010. → pages 2

[14] D. Bera, L. Qian, T.-K. Tseng, and P. H. Holloway, "Quantum dots and their multimodal applications: a review," *Materials*, vol. 3, no. 4, pp. 2260–2345, 2010. → pages 2

[15] J. L. Delgado, M. Á. Herranz, and N. Martin, "The nano-forms of carbon," *Journal of Materials Chemistry*, vol. 18, no. 13, pp. 1417–1426, 2008. → pages 2, 15

[16] B. Schultrich, *Tetrahedrally Bonded Amorphous Carbon Films I: Basics, Structure and Preparation*. Springer, 2018, vol. 263. → pages 2

[17] S. Nasir, M. Hussein, Z. Zainal, and N. Yusof, "Carbon-based nanomaterials/allotropes: A glimpse of their synthesis, properties and some applications," *Materials*, vol. 11, no. 2, p. 295, 2018. → pages 5

[18] I. Kratochvilova, "Polycrystalline diamond thin films for advanced applications," in *Advances in Carbon Nanostructures*. InTech, 2016. → pages 5

[19] Z. H. Stachurski, "On structure and properties of amorphous materials," *Materials*, vol. 4, no. 9, pp. 1564–1598, 2011. → pages 5

[20] G. Kopidakis, I. N. Remediakis, M. G. Fyta, and P. C. Kelires, "Atomic and electronic structure of crystalline–amorphous carbon interfaces," *Diamond & Related Materials*, vol. 16, no. 10, pp. 1875–1881, 2007. → pages 5

[21] A. H. Lettington, "Applications of diamond-like carbon thin films," *Carbon*, vol. 36, no. 5, pp. 555–560, 1998. → pages 5

[22] E. Asmatulu, R. Asmatulu, and P. Nguyen, *Chapter 5 - Nanotechnology Safety in the Automotive Industry.* Elsevier B.V, 2013. → pages 5

[23] C. C. Blatchley, *Chapter 6 - Nanotechnology Safety in the Biomedical Industry.* Elsevier B.V, 2013. → pages 5

[24] V. Y. Vasilyev, N. B. Morozova, T. V. Basova, I. K. Igumenov, and A. Hassan, "Chemical vapour deposition of ir-based coatings: chemistry, processes and applications," vol. 5, no. 41, pp. 3234–3263, 2015. → pages 5

[25] S. Neuville and A. Matthews, "A perspective on the optimisation of hard carbon and related coatings for engineering applications," *Thin solid films*, vol. 515, no. 17, pp. 6619–6653, 2007. → pages 7, 8, 22, 30, 64

[26] A. Ababou, B. Carriere, G. Goetz, J. Guille, B. Marcus, M. Mermoux, A. Mosser, M. Romeo, and F. Le Normand, "Surface characterization of microwave-assisted chemically vapour deposited carbon deposits on silicon and transition metal substrates," *Diamond and Related Materials*, vol. 1, no. 8, pp. 875–881, 1992. → pages 7

[27] A. C. Ferrari and J. Robertson, "Raman spectroscopy of amorphous, nanostructured, diamond–like carbon, and nanodiamond," *Philosophical Transactions of the Royal Society of London. Series A: Mathematical, Physical and Engineering Sciences*, vol. 362, no. 1824, pp. 2477–2512, 2004. → pages 7, 31

[28] J. R. Ferraro, K. Nakamoto, and C. W. Brown, *Introductory Raman spectroscopy*, 2nd ed. Amsterdam;Boston;: Academic Press, 2003. → pages 7, 25, 28

[29] V. Paillard, "On the origin of the 1100 raman band in amorphous and nanocrystalline sp3 carbon," *EPL (Europhysics Letters)*, vol. 54, p. 194, 2001. → pages 7

[30] A. C. Ferrari and J. Robertson, "Interpretation of raman spectra of disordered and amorphous carbon," *Physical review B*, vol. 61, no. 20, p. 14095, 2000. → pages 8, 31, 36

[31] A. Jorio, E. H. M. Ferreira, M. V. Moutinho, F. Stavale, C. A. Achete, and R. B. Capaz, "Measuring disorder in graphene with the g and d bands," *physica status solidi (b)*, vol. 247, no. 11-12, pp. 2980–2982, 2010. → pages 8

[32] F. Tuinstra and J. L. Koenig, "Raman spectrum of graphite," *The Journal of Chemical Physics*, vol. 53, no. 3, pp. 1126–1130, 1970. → pages

[33] L. Cançado, K. Takai, T. Enoki, M. Endo, Y. Kim, H. Mizusaki, A. Jorio, L. Coelho, R. Magalhaes-Paniago, and M. Pimenta, "General equation for the determination of the crystallite size l a of nanographite by raman spectroscopy," *Applied Physics Letters*, vol. 88, no. 16, p. 163106, 2006. → pages

[34] M. S. Dresselhaus and R. Kalish, *Ion implantation in diamond, graphite and related materials.* Springer Science & Business Media, 2013, vol. 22. → pages 8

[35] A. Shen, Y.-C. Weng, and T.-C. Chou, "Effect of the analytic regions on the quality trend of diamond-like/graphitic carbon ratios in raman spectra," *Zeitschrift für Naturforschung B*, vol. 65, no. 1, pp. 67–71, 2010. → pages 8

[36] S. Hashmi, *Comprehensive Materials Processing.* Elsevier Science, 2014. [Online]. Available: https://books.google.ca/books?id=OV9-AgAAQBAJ → pages 12

[37] F. Lampert, P. Møller, and J. B. Rasmussen, "Thin glass coatings for the corrosion protection of metals," Ph.D. dissertation, Technical University of Denmark (DTU), 2017. → pages 12

[38] M. Seal, "Diamonds in science," *Interdisciplinary Science Reviews*, vol. 14, no. 1, pp. 64–76, 1989. [Online]. Available: https://doi.org/10.1179/isr.1989.14.1.64 → pages ix, 13, 14

[39] P. W. May, "Diamond thin films: a 21st-century material," *Philosophical Transactions of the Royal Society of London. Series A: Mathematical, Physical and Engineering Sciences*, vol. 358, no. 1766, pp. 473–495, 2000. → pages 13

[40] S. Seo, "The characterization of diamond-like carbon films deposited using unbalanced magnetron sputtering." 1998. → pages 13

[41] D. Saada, "Ion implantation into diamond and the subsequent graphitization," Ph.D. dissertation, Thèse de Doctorat, Israel Institute of Technology, 2000. → pages 13

[42] K. Kanda, S. Takehana, S. Yoshida, R. Watanabe, S. Takano, H. Ando, and F. Shimakura, "Application of diamond-coated cutting tools," *Sur-*

face and Coatings Technology, vol. 73, no. 1-2, pp. 115–120, 1995. → pages 13

[43] J. Hannay, "Vi. on the artificial formation of the diamond," *Proceedings of the Royal Society of London*, vol. 30, no. 200-205, pp. 450–461, 1880. → pages 14, 15

[44] J. Laumer, "A Raman and scanning electron microscope analysis of magnetron sputtered thin-film carbon," Master's thesis, University of British Columbia, 2014. → pages 14, 15, 30, 51, 106

[45] S. Aisenberg and R. Chabot, "Ion-beam deposition of thin films of diamondlike carbon," *Journal of applied physics*, vol. 42, no. 7, pp. 2953–2958, 1971. → pages 15, 19, 20

[46] A. Grill, "Diamond-like carbon: state of the art," *Diamond and related materials*, vol. 8, no. 2-5, pp. 428–434, 1999. → pages 15, 64

[47] S. Semiatin, S. Knisley, P. Fagin, D. Barker, and F. Zhang, "Microstructure evolution during alpha-beta heat treatment of ti-6al-4v," *Metallurgical and Materials Transactions A*, vol. 34, no. 10, pp. 2377–2386, 2003. → pages 16

[48] K. Bobzin, N. Bagcivan, N. Goebbels, and K. Yilmaz, "Effect of the substrate geometry on plasma synthesis of dlc coatings," *Plasma Processes and Polymers*, vol. 6, no. S1, pp. S425–S428, 2009. → pages 16

[49] K. Wojciechowski, R. Zybala, R. Mania, and J. Morgiel, "Dlc layers prepared by the pvd magnetron sputtering technique," *Journal of Achieve-*

ments in Materials and Manufacturing Engineering, vol. 37, no. 2, pp. 726–729, 2009. → pages

[50] M. Maharizi, O. Segal, E. Ben-Jacob, Y. Rosenwaks, T. Meoded, N. Croitoru, and A. Seidman, "Physical properties of a: Dlc films and their dependence on parameters of deposition and type of substrate," *Diamond and related materials*, vol. 8, no. 6, pp. 1050–1056, 1999. → pages 16

[51] L. Bonetti, G. Capote, L. Santos, E. Corat, and V. Trava-Airoldi, "Adhesion studies of diamond-like carbon films deposited on ti6al4v substrate with a silicon interlayer," *Thin Solid Films*, vol. 515, no. 1, pp. 375–379, 2006. → pages 16, 21

[52] J. G. Buijnsters, P. Shankar, W. Fleischer, W. Van Enckevort, J. Schermer, and J. Ter Meulen, "Cvd diamond deposition on steel using arc-plated chromium nitride interlayers," *Diamond and related materials*, vol. 11, no. 3-6, pp. 536–544, 2002. → pages 17, 20, 21

[53] E. Gariboldi, "Drilling a magnesium alloy using pvd coated twist drills," *Journal of Materials Processing Technology*, vol. 134, no. 3, pp. 287–295, 2003. → pages 17

[54] M. Smietana, M. Korwin-Pawlowski, W. Bock, G. Pickrell, and J. Szmidt, "Refractive index sensing of fiber optic long-period grating structures coated with a plasma deposited diamond-like carbon thin film," *Measurement Science and Technology*, vol. 19, no. 8, p. 085301, 2008. → pages 17

[55] M. Gilo and A. Azran, "Low reflectance dlc coatings on various ir sub-

strates," in *Infrared Technology and Applications XXXVIII*, vol. 8353. International Society for Optics and Photonics, 2012, p. 835320. → pages 20, 21

[56] M. Allen, B. Myer, and N. Rushton, "In vitro and in vivo investigations into the biocompatibility of diamond-like carbon (dlc) coatings for orthopedic applications," *Journal of Biomedical Materials Research: An Official Journal of The Society for Biomaterials, The Japanese Society for Biomaterials, and The Australian Society for Biomaterials and the Korean Society for Biomaterials*, vol. 58, no. 3, pp. 319–328, 2001. → pages 17, 21

[57] J. Robertson, "Diamond-like amorphous carbon," *Materials science and engineering: R: Reports*, vol. 37, no. 4-6, pp. 129–281, 2002. → pages 18, 20, 64

[58] R. Street, "Hydrogenated amorphous silicon cambridge solid state science series, ed. cahn, rw, davis, ea, and ward, im," 1991. → pages 19

[59] R. J. Yeo, *Overview of Amorphous Carbon Films*. Singapore: Springer Singapore, 2017, pp. 29–37. [Online]. Available: https://doi.org/10.1007/978-981-10-4882-1_2 → pages 20

[60] S. J. Barton, B. M. Hennelly, T. Ward, K. Domijan, and J. Lowry, "A review of raman for multicomponent analysis," in *Biophotonics: Photonic Solutions for Better Health Care IV*, vol. 9129. International Society for Optics and Photonics, 2014, p. 91290C. → pages 21, 28

[61] J. J. Sakurai and E. D. Commins, "Modern quantum mechanics, revised edition," 1995. → pages 24

[62] J. A. Lohne, "Experimentum crucis," *Notes and records of the Royal Society of London*, vol. 23, no. 2, pp. 169–199, 1968. → pages 24

[63] F. A. James, "The practical problems of 'new'experimental science: spectro-chemistry and the search for hitherto unknown chemical elements in britain 1860–1869," *The British Journal for the History of Science*, vol. 21, no. 2, pp. 181–194, 1988. → pages 24

[64] M. Qasim, *Simplified Concepts in Spectroscopy and Photochemistry*. US Army Engineer Waterways Experiment Station, 1997. → pages 24

[65] E. P. Fischer, "We are all aspects of one single being: An introduction to erwin schrödinger," *Social research*, vol. 51, no. 3, p. 809, 1984. → pages 24

[66] R. J. Gale, *Spectroelectrochemistry: theory and practice*. Springer Science & Business Media, 2012. → pages 25

[67] R. L. McCreery, "Raman spectroscopy for chemical analysis," *Measurement science and technology*, vol. 12, no. 5, p. 653, 2001. → pages 25

[68] J. Schwan, S. Ulrich, V. Batori, H. Ehrhardt, and S. Silva, "Raman spectroscopy on amorphous carbon films," *Journal of Applied Physics*, vol. 80, no. 1, pp. 440–447, 1996. → pages 28

[69] H. Kerr, Byrne, "optimal choice of sample substrate and laser wavelength for raman spectroscopic analysis of biological specimen," pp. 5041–5052, 2015. → pages 30

[70] D. Tuschel, "Selecting an excitation wavelength for raman spectroscopy," 2016. → pages 30, 31

[71] A. C. Ferrari, "Determination of bonding in diamond-like carbon by raman spectroscopy," *Diamond and Related Materials*, vol. 11, no. 3-6, pp. 1053–1061, 2002. → pages 30

[72] I. Pócsik, M. Hundhausen, M. Koós, and L. Ley, "Origin of the d peak in the raman spectrum of microcrystalline graphite," *Journal of Non-Crystalline Solids*, vol. 227, pp. 1083–1086, 1998. → pages 31

[73] I. Alexandrou, H.-J. Scheibe, C. Kiely, A. Papworth, G. Amaratunga, and B. Schultrich, "Carbon films with an sp 2 network structure," *Physical Review B*, vol. 60, no. 15, p. 10903, 1999. → pages 31

[74] A. Modabberasl, P. Kameli, M. Ranjbar, H. Salamati, and R. Ashiri, "Fabrication of dlc thin films with improved diamond-like carbon character by the application of external magnetic field," *Carbon*, vol. 94, pp. 485–493, 2015. → pages 32, 33

[75] R. Paul, S. Hussain, S. Majumder, S. Varma, and A. Pal, "Surface plasmon characteristics of nanocrystalline gold/dlc composite films prepared by plasma cvd technique," *Materials Science and Engineering: B*, vol. 164, no. 3, pp. 156–164, 2009. → pages 32, 33

[76] M. Panda, G. Mangamma, R. Krishnan, K. K. Madapu, D. N. G. Krishna, S. Dash, and A. Tyagi, "Nano scale investigation of particulate contribution to diamond like carbon film by pulsed laser deposition," *RSC Advances*, vol. 6, no. 8, pp. 6016–6028, 2016. → pages 32, 34

[77] P. Colomban and A. Slodczyk, "Raman intensity: An important tool in the study of nanomaterials and nanostructures," *Acta Physica Polonica A*, vol. 116, no. 1, pp. 7–12, 2009. → pages 32

[78] M. R. Joya, K. M. Fonseca, and J. Barba-Ortega, "Difference in the relative intensities raman of the perovskite plt with temperature," *AIP Conference Proceedings*, vol. 1627, no. 1, pp. 42–45, 2014. [Online]. Available: https://aip.scitation.org/doi/abs/10.1063/1.4901655 → pages 35

[79] B. Marchon, N. Heiman, and M. R. Khan, "Evidence for tribochemical wear on amorphous carbon thin films," *IEEE Transactions on Magnetics*, vol. 26, no. 1, pp. 168–170, 1990. → pages 35

[80] M. Okada, K. Yoshikawa, Y. Yamamoto, and H. Toku, "Process for coating diamond-like carbon film and coated thin strip," Oct. 3 1995, uS Patent 5,455,081. → pages 35

[81] S. A. Asher, "Ultraviolet r aman spectrometry," *Handbook of vibrational spectroscopy*, 2006. → pages 37

[82] D. C. Zhao, N. Ren, Z. J. Ma, G. J. Xiao, and S. H. Wu, "Study on the mechanic properties of dlc films on different metal substrates," in *Key Engineering Materials*, vol. 373. Trans Tech Publ, 2008, pp. 117–121. → pages 61, 77, 81, 85

[83] A. Wu, J. Sun, X. Shen, N. Xu, Z. Ying, Z. Dong, and J. Wu, "Diamond-like carbon thin films prepared by ecr argon plasma assisted pulsed laser deposition," *Diamond and related materials*, vol. 15, no. 9, pp. 1235–1241, 2006. → pages 64

[84] G. Compagnini, U. Zammit, K. N. Madhusoodanan, and G. Foti, "Disorder and absorption edges in ion-irradiated hydrogenated amorphous carbon films," *Phys. Rev. B*, vol. 51, pp. 11 168–11 171, Apr 1995. [Online]. Available: https://link.aps.org/doi/10.1103/PhysRevB.51.11168 → pages 67

[85] G. Yue, B. Yan, G. Ganguly, J. Yang, S. Guha, and C. W. Teplin, "Material structure and metastability of hydrogenated nanocrystalline silicon solar cells," *Applied Physics Letters*, vol. 88, no. 26, p. 263507, 2006. → pages 68, 69

[86] A. Baby, C. Mahony, and P. Maguire, "Acetylene–argon plasmas measured at a biased substrate electrode for diamond-like carbon deposition: I. mass spectrometry," *Plasma Sources Science and Technology*, vol. 20, no. 1, p. 015003, 2011. → pages 74

[87] M. Wojciechowicz, "Advanced MATLAB Techniques for Raman Spectral Processing," 2016. → pages 85

[88] X. Yuan and R. A. Mayanovic, "An empirical study on raman peak fitting and its application to raman quantitative research," *Applied Spectroscopy*, vol. 71, no. 10, pp. 2325–2338, 2017, pMID: 28665140. [Online]. Available: https://doi.org/10.1177/0003702817721527 → pages 86

[89] J. Miles, "R-squared, adjusted r-squared," *Encyclopedia of Statistics in Behavioral Science*, 2005. → pages 103